Aalto-yliopisto
Aalto-universitetet
Aalto University

Master's Programme in European Mining, Minerals and Environmental Programme

Numerical modelling of microwave pre-treatment of some sulfidic ores

Sami Naumer

Master's Thesis
2021

Aalto-yliopisto
Aalto-universitetet
Aalto University

Author Sami Naumer

Title of thesis Numerical modelling of microwave pre-treatment of some sulfidic ores

Programme European Mining, Minerals and Environmental Programme (EMMEP)

Major European Mining Course (EMC)

Thesis supervisor Prof. Mikael Rinne

Thesis advisor(s) M.Sc. Risto Kiuru

Collaborative partner Oy Rock Physics Finland Ltd

Date 22.09.2021 **Number of pages** 83 **Language** English

Abstract

Microwave pre-treatment of rock is a promising way to decrease rock strength during rock comminution processes. The microwave radiation transfers heat to the rock which then heats up and expands. This induces stresses within the rock. In this study, numerical modelling is used to assess how different material and irradiation parameters affect the induced stresses.

The study is divided into two numerical models: one for a simulated rock sample and one for a digitized rock sample. In both models, a rock sample was irradiated with microwave radiation within a simulated microwave oven. In the first model, the rock sample was modelled so that its material parameters could be easily varied. The rock sample consisted of two materials with different capabilities to absorb heat from microwave radiation. The varied material parameters included the mineral composition, the ratio between the two minerals, grain size and mineral shapes of the rock sample. Additionally, microwave input power was varied and the effect of the wave pattern inside the microwave oven studied

In the second model a rock sample from Pyhäsalmi mine was digitized into a 3D model which then replaced the simulated rock sample within the modelled microwave oven. The sample consisted of four minerals: pyrite, chalcopyrite, sphalerite and pyrrhotite. The model was used to study where the induced stresses were situated in the rock sample and the magnitude of the induced stresses.

The results showed that increasing the fraction of the mineral with a high capability to absorb microwave radiation increased the temperatures in the sample significantly. However, heterogenous mineral composition was required to concentrate the stresses on mineral boundaries. More heterogenous mineral composition was achieved with larger grains and minerals with different mechanical properties. Highest stresses were observed on mineral boundaries between two minerals with different, but high elastic moduli and coefficient of thermal expansion. Narrower angles within the minerals also resulted in higher stresses.

Keywords microwave pre-treatment, heat transfer in rock, rock comminution, induced stress in rock

Aalto-yliopisto
Aalto-universitetet
Aalto University

Tekijä Sami Naumer

Työn nimi Joidenkin sulfidimineraalien mikroaaltokäsittelyn numeerinen mallinnus.

Koulutusohjelma European Mining, Minerals and Environmental Programme (EMMEP)

Pääaine European Mining Course (EMC)

Vastuuopettaja/valvoja Prof. Mikael Rinne

Työn ohjaaja(t) FM. Risto Kiuru

Yhteistyötaho Oy Rock Physics Finland Ltd

Päivämäärä 22.09.2021 **Sivumäärä** 83 **Kieli** englanti

Tiivistelmä

Kiven mikroaaltokäsittely on lupaava keino vähentää kiven lujuutta jauhatusprosessin aikana. Mikroaallot siirtävät lämpöä kiveen, joka lämpenee ja laajenee. Tämän johdosta kiveen indusoituu jännitteitä. Tässä tutkimuksessa tutkitaan eri materiaali- ja säteilyparametrien vaikutusta indusoituihin jännitteisiin numeerisella mallinnuksella.

Tämä tutkimus on jaettu kahteen numeeriseen malliin: ensimmäisessä mallinnetaan simuloitua kivinäytettä ja toisessa digitoitua näytettä. Molemmissa malleissa kivinäytettä säteilytettiin simuloidussa mikroaaltouunissa. Ensimmäisen mallin näyte mallinnettiin siten, että sen materiaaliparametrejä voitiin muuttaa helposti. Näyte koostui kahdesta eri mineraalista, joilla oli eri kyvyt absorboida lämpöä mikroaaltosäteilystä. Muunnettaviin materiaaliparametreihin kuuluivat kiven mineraalirakenne, kahden mineraalin määrän välinen suhde, raekoko ja rakeiden muoto. Lisäksi mikroaaltosäteilyn tehoa muutettiin ja sähkömagneettisen kentän muodon vaikutusta tutkittiin.

Toisessa mallissa Pyhäsalmen kaivoksesta oleva kivinäyte digitoitiin 3D-malliksi, joka sijoitettiin mallinnettuun mikroaaltouuniin simuloidun kivinäytteen tilalle. Kivi koostui neljästä mineraalista: pyriitistä, kuparikiisusta, sinkkivälkkeestä sekä magneettikiisusta. Mallilla tutkittiin, mihin jännitteet indusoituvat kivinäytteessä sekä indusoitujen jännitteiden suuruutta.

Tuloksista kävi ilmi, että lisättäessä mineraalia, jolla on hyvä kyky absorboida lämpöä mikroaaltosäteilystä, kivinäytteen lämpötilat nousivat huomattavasti. Jotta mineraalien rajoille syntyi jännitteitä, mineraalien tuli olla heterogeenisiä rajan molemmin puolin. Heterogeeninen materiaalirakenne muodostui esimerkiksi suuremmalla raekoolla ja mineraalien eri mekaanisilla ominaisuuksilla. Korkeimmat jännitteet olivat rajoilla, joiden eri puolilla olevien mineraalien elastiset kertoimet sekä lämpölaajenemiskertoimet olivat korkeat, mutta erosivat toisistansa.

Avainsanat mikroaaltokäsittely, lämmönsiirtyminen kivessä, kiven jauhatus, kiveen indusoituneet jännitteet

Table of contents

Preface

I would like to thank both my advisor Risto Kiuru and my supervisor Mikael Rinne on guiding the thesis through its many iterations. Discussions with both of you were very fruitful and I learned a lot throughout the process.

Furthermore, I wish to thank the professionals who gave me insightful information on both microwave physics and their application in COMSOL. As this was prior to the thesis outside of my knowledge, your help was well received.

Finally, I want to thank all friends and family who encouraged me and helped me to stay motivated during the process. Especially a big thank you to Iisa.

Espoo 22.09.2021
Sami Naumer

Symbols and abbreviations

Symbols

Symbol	Description
$\boldsymbol{D}$	Electric displacement field
$\boldsymbol{B}$	Magnetic field
$\boldsymbol{H}$	Magnetic field intensity
$\boldsymbol{J}$	Current density
$\dot{\boldsymbol{j}}$	Total current density
$\boldsymbol{E}$	Electric field
$\dot{\boldsymbol{E}}$	Complex quantity of $\boldsymbol{E}$
$\boldsymbol{\sigma}$	Electric conductivity of a material
$\boldsymbol{w}$	Electric power converted to heat in a conductive material
$\boldsymbol{w_a}$	Heat generated by dielectric losses
$\boldsymbol{\varepsilon_0}$	Dielectric constant of a vacuum ($8.86 \cdot 10^{-12}\ F/m$)
$\boldsymbol{\varepsilon_r}$	Absolute dielectric constant
$\boldsymbol{\varepsilon_r'}$	Real part of the absolute dielectric constant
$\boldsymbol{\varepsilon_r''}$	Imaginary part of the absolute dielectric constant
$\boldsymbol{\delta}$	Loss angle
$\boldsymbol{j}$	Imaginary unit
$\boldsymbol{f}$	Frequency of an electromagnetic wave
$\boldsymbol{\lambda}$	Wavelength of an electromagnetic wave
$\boldsymbol{\alpha}$	Thermal diffusivity
$\boldsymbol{c_p}$	Specific heat capacity
$\boldsymbol{k}$	Thermal conductivity
$\boldsymbol{T}$	Temperature
$\boldsymbol{q}$	Heat flux
$\boldsymbol{h}$	Heat transfer coefficient
$\boldsymbol{A}$	Area of a surface
$\boldsymbol{q_v}$	volume charge density
$\boldsymbol{Q_{in}}$	Heat entering a system
$\boldsymbol{E^*}$	Internal energy of a system
$\boldsymbol{E_s^*}$	Internal energy per unit mass of a system
$\boldsymbol{K}$	Kinetic energy of a system
$\boldsymbol{P_{ext}}$	Power of forces applied to a system
$\boldsymbol{P_{str}}$	Stress power
$\boldsymbol{Q_{exh}}$	Heat a system exchanges with its environment
$\boldsymbol{t}$	Time
$\boldsymbol{\rho}$	Density of a material
$\boldsymbol{\sigma}$	Cauchy stress tensor
$\boldsymbol{D^*}$	Strain rate tensor
$\boldsymbol{Q_{add}}$	Additional heat sources of a system
$\boldsymbol{u}$	Velocity field
$\boldsymbol{S}$	Second Piola-Kirchhoff stress tensor
$\boldsymbol{Y}$	Young's modulus
$\boldsymbol{\epsilon_{th}}$	Thermal strain
$\boldsymbol{\alpha_V}$	Coefficient of thermal expansion
$\boldsymbol{\sigma_1}$	First principal stress
$\boldsymbol{\sigma_3}$	Third principal stress
$\boldsymbol{\sigma_n}$	Normal stress

$\boldsymbol{\phi}$	Angle of internal fiction
$\boldsymbol{c}$	Cohesion
$\boldsymbol{m_i}$	Empirical parameter of intact rock

Operators

∇f	Gradient of a scalar function
$\nabla \cdot \mathbf{A}$	divergence of a vector field **A**
$\nabla \times \mathbf{A}$	curl of vector **A**
$\frac{\mathrm{d}}{\mathrm{d}t}$	derivative with respect to variable t
$\frac{\delta}{\delta t}$	partial derivative with respect to variable t
$\mathbf{A} \cdot \mathbf{B}$	dot product of vectors **A** and **B**
$\boldsymbol{tr}(\boldsymbol{A})$	Trace function of a square matrix
$\boldsymbol{\delta_{ij}}$	Kronecker delta $\delta_{ij} = \begin{cases} 0 \; if \; i \neq j \\ 1 \; if \; i = j \end{cases}$.

Abbreviations

EM	Electromagnetic
ISM	Industrial, scientific, and medical
FEM	Finite element model

1 Introduction

Rock comminution is the process of decreasing the particle size of rock in ore processing. After extraction of ore, the first size-reducing process in ore processing plants is often done by crushing with different types of rock crushers. This process is often very energy intensive, taking up to half of the processing plants energy consumption (Dunne, Kawatara and Young, 2019). Thus, ways to decrease the energy consumption in ore processing should be sought for.

Energy consumption of rock comminution is significantly influenced by rock strength, more specifically, the uniaxial compressive strength of the rock (Haffez, 2012; Korman *et al.*, 2015). Thus, the energy consumption of rock comminution can be decreased by pre-treating the rock so that the rock strength is decreased. Multiple pre-treating methods exist with one commonly studied one being heat treatment of the rock. In this thesis, heat treatment via microwave radiation is studied.

Heat transfer using microwaves is a well-established method in multiple fields, both in industrial and household applications. Energy is transferred via microwaves which lose some of the energy in certain materials as heat losses. The heat losses result in increasing temperatures in objects under the microwave radiation. Usually, this increasing temperature is used to simply heat up the object, for example in household cooking or industrial melting processes. However, increases in temperature also cause the object to thermally expand. This expansion causes internal stresses in the object. If these stresses grow large enough, they can induce damage in the object, or in other words, decrease the strength of the material. It has been well established that treating rock with microwave radiation can cause significant temperatures and stresses within it. These studies are briefly discussed in **Section 2.**

1.1 Objectives and research questions

This thesis consists of two separate numerical models in which different aspects of heat treatment of rock using microwave radiation are assessed. In the first model, the aim is to study how different mineral and microwave parameters affect the induced temperatures and stresses in rock. This is achieved by individually changing rock and mineral properties. These properties include for example shapes and sizes of the minerals and mineral composition of the rock. Microwave radiation parameters such as frequency and power are also varied.

Conducting physical experiments to assess the effects of the changes in parameters in depth is far beyond the scope of this master thesis. Thus, a numerical model is created, where conducting many different conditions can be done by changing input values of the model. The aim is to create a simulated rock sample with properties based on two real minerals. The ratios between the minerals, mineral sizes and shapes are all set up so that they can easily be changed. Such a rock does not correspond to any real rock but can help to understand how individual aspects of the rock affect the viability of microwave treatment.

In the second model, a real rock sample is digitized to numerically assess how stresses are induced on a realistic mineral geometry. First, different ore rocks common in Finnish mines are compared. The aim is to assess which typical ore minerals are suitable for microwave treatment. Such minerals should generate high heat losses when exposed to microwave radiation. This is followed by choosing a mineral to be digitized. The digitized model is then imported to the numerical modelling software, where a microwave treatment is simulated similarly to the first model.

With the two models and the literature reviews, the following research questions are sought to be answered:

1) What ores and minerals are suitable for microwave treatment?

2) How do different microwave and rock properties affect the induced temperatures and stresses of a simulated rock sample?

3) How does microwave heating affect the stress-state of a realistic mineral geometry?

The answers to the research questions are further used to discuss how they affect a real ore comminution process.

Prior to the numerical modelling, it is hypothesized that heat treatment of rock via microwave radiation cause minerals to heat up. This increase in temperature leads to thermally induced stresses in the rock. The induced stresses can be increased by treating rocks consisting of minerals, where high microwave heat losses occur. The rock sample should consist of various minerals in order to concentrate large stresses on mineral boundaries.

Large stresses at mineral boundaries could exceed the rock strength and thus reduce the strength of the rock. Thus, minerals with properties that lead to increased stresses should be well suited for microwave treatment. Such properties could be for example the readiness to absorb energy from microwave radiation or the mechanical properties of the minerals.

1.2 Scope of the study and research material

As the studied topic is complex, certain limitations of this thesis should be addressed. As mentioned previously, microwave heating of rock in this study is limited to numerically modelling. Hence, no physical experiments are conducted. The configurations of material parameters are limited so that only one parameter is changed at a time. If combined effects of multiple parameters would be studied, the amount of different model setups would grow exponentially.

In the second model, only one suitable rock is digitized and modelled. This way, the sample can be digitized in more detail and the effect of the microwave radiation studied more thoroughly. Additionally, the considered rock sample should be typical in ores, as the mining industry would benefit the most from applying microwave pre-treatment to their processes. Aalto University has multiple samples of ore rocks from Finland. Thus, the availability of

rocks was greater for rocks from Finnish mines. Additionally, rocks from operational mines are usually confidential. Therefore, the selection of rock samples is limited to mines close to the end of mine life. Additionally, in neither model damage to the rock is modelled as the emphasis is on the stress evolution of the rock. Calculating plastic deformation of rock requires a wide range of material parameters which are not readily available. Thus, the study does not assess how the rock strength is affected. However, the stress assessment is conducted from a point of view where the sample is heated up with using as little energy as possible.

COMSOL-Multiphysics (from now on "COMSOL") is chosen as the used numerical modelling software, as it allows for coupling of different physical fields so that they can be solved simultaneously. In this study, microwave radiation, heat transfer, and solid mechanics are combined in order to simulate the microwave treatment and the resulting temperature and stress states.

In prior to the two numerical models, a literature review is conducted. The aim of the literature review is to present a compact version of the required theory to understand how microwaves are generated and how energy is transferred via the radiation. The theory is used as the basis of the numerical modelling, where it is applied as the governing equations of the model. The literature review also briefly summarizes prior research on the field. The theory is compiled from textbooks and from similar studies presented in scientific journals.

2 Literature review of previous studies conducted on microwave treatment of ore rock

In this section, selected important studies of microwave treatment of ore and rock are briefly introduced. The aim is to present general trends that have been in the studies. This section is used as a basis for the initial setup of the numerical model later in this thesis.

Whittles, Kingman and Reddish (2003) conducted a study on how electric field strength of microwave treatment of ore affects the uniaxial compressive strength of the ore. In the study, a numerical model using finite difference modelling was created for a sample where chalcopyrite is embedded in a calcite host rock. The sample was heated with heating times of 1, 5, 15 and 30 seconds. The study showed that with higher power densities of microwave radiation, the unconfined compressive strength of the rock reduced significantly more when compared to lower power densities. With a power density of 100 GW/m^3, the compressive strength of the rock decreased from 126 MPa to 57 MPa in just 0.05 s. Thus, increasing the power density increases thermal stresses faster than when the rock is exposed lower densities.

Pressacco and Saksala (2018) created a numerical model for thermally induced rock fracturing in granitic rock. In the model, heat was applied on the boundaries of a rock specimen. The heat applied on the boundaries induced multiple small cracks on the rock surfaces. They also determined how thermally induced damage influenced the compressive strength of the rock. The results showed that the strength of the rock was reduced between 35 % – 50 % when compared to untreated rock.

Pressacco and Saksala (2019) investigated how thermal shock can be applied as a pre-treatment of rock for rock comminution. The emphasis was on how the thermally induced cracking of rock affects the compressive strength of it. The study was conducted for a granitic specimen. The study shows that 1) existing microcracks within a rock sample have an insignificant effect on the temperature evolution of the rock, 2) increasing heating time causes increased tension within the samples, and 3) tests with different internal structure of the rock caused differing crack patterns which however followed a general trend. The uniaxial compressive tests on the heat-treated rock samples resulted in 40 % – 50 % reduced compressive strengths of the samples when compared to intact rock. The study also showed that a higher intensity, but shorter duration heat treatment reduced the compressive strength more, than a longer treatment with a lesser heat flux intensity.

Similar results, where short duration, high intensity radiation reduced the strength of the ore, have been shown in a wide range of other studies as well. Ali and Bradshaw (2010) performed numerical tests for ore consisting of microwave absorbent galena and non-absorbent calcite. The test showed not only that high power density resulted in more damage in grain boundaries, but also that high power density is required in order to treat finely grained ores at an efficient energy usage. Li *et al.* (2019) conducted a similar numerical study on pegmatitic samples. The results showed that both compressive and tensile stresses increased fastest on grain boundaries between quartz and plagioclase. Additionally, materials with larger dielectric constants and coefficients of thermal expansion of minerals caused larger strains.

Kingman, Corfield and Rowson (1998) performed laboratory experiments on ilmenite ore with a 2.6 kW, 2.45 GHz microwave oven. The samples were exposed for microwave radiation with both 1.3 kW and 2.6 kW powers for 30 s and 60 s. After heating the samples, they were rapidly cooled with water. The study showed increased number of fractures at grain boundaries between ilmenite and surrounding calcic plagioclase. Zheng *et al.* (2020) also state that rocks containing various minerals with different dielectric properties have a greater weakening effect than a more homogenous material.

Toifl *et al.* (2016) created a 3D numerical model in order to study how heat transferred via microwave radiation induces stresses in inhomogeneous rocks. The study was conducted with 15 s and 25 s irradiation times with a 25 kW power and a microwave frequency of 2.45 GHz. The study also considered the phase transformation of quartz in high temperatures. The study showed that tensile strength of the rock was exceeded in areas up to 10 cm deep in the rock in the direction of the microwave radiation. The study showed higher stresses in inhomogeneous samples when compared to homogenous samples, as grains more absorbent of microwave radiation deeper in the rock heated up more in the inhomogeneous case. In addition to damage caused by tensile stresses, compressive stresses in some areas within the rock exceeded compressive rock strength of the rock. Higher stresses in inhomogeneous samples are partly explained by the higher temperature gradients caused by grains with different dielectric parameters heating up nonuniformly. With 25 s radiation durations, the quartz within the samples heated up sufficiently to undergo a phase transformation. This induced even greater stresses within the sample.

Finally, Hartlieb *et al.* (2012) performed laboratory tests on basaltic rock samples and compared them to numerical results. The experiments were conducted with a 3.2 kW, 2.45 GHz microwave oven. The study showed that in laboratory experiments, where a sample is absorbing radiation rather homogeneously, the sample is heated up equally. However outwards heat radiation from the surfaces causes them to be cooler than the internal parts of the sample.

From the studies, it would seem that microwave heat treatment of ore can induce large enough stresses, to form discontinuities in the rock structure. The highest stresses seem to occur on boundaries between different minerals within the rock.

Discontinuities significantly weaken the rock compressive strength. As the energy consumption of rock comminution is dependent on rock strength, this could lead into less energy required in the rock comminution process. However, the microwave treatment itself consumes energy. Thus, the decrease in energy consumption in comminution should be larger than the required energy in the microwave treatment process. This way, a decrease in total energy consumption of the process can be achieved.

In order to minimize the energy consumption of the microwave treatment process, it would seem that short irradiation times with high microwave energy densities should be preferred. The studies also show that the mineral composition of the rock plays a large role on the induced stresses. Heterogenous rocks consisting of minerals with different material properties seem to induce larger stresses than homogenous minerals. However, homogenous

minerals seem to absorb heat more equally which can lead to higher total temperatures in the rock.

3 Theory of microwave induced stress in rock

In this section theory and background information required to understand microwave heat transfer is presented. First, the basics including the nature of electromagnetic- and microwaves and ways to generate them are discussed. This is followed by derivation of equations for dielectric materials in electromagnetic fields. Heat balance and the continuum mechanics equations are additionally described in their form presented in COMSOL. Finally, rock strength is discussed and the equations for modelling rock strength are presented.

3.1 Electromagnetic waves

Maxwell equations are the four well-known foundational equations which combine electricity and magnetism in a single theory, electromagnetism. They describe how electric and magnetic field are related and how a change in one affects the other. Together the electric and magnetic fields create a single, electromagnetic (EM) field (Bécherrawy, 2012). The first equation is Gauss's law which in differential form can be expressed as

$$\nabla \cdot \boldsymbol{D} = q_{\mathrm{v}} \tag{1}$$

where $\boldsymbol{D}$ is the electrical displacement field and q_{v} the volume charge density. It describes how a closed surface with an electric charge creates an electric field. The second equation, Gauss's law for magnetism, describes how magnetic monopoles do not exist and is expressed as

$$\nabla \cdot \boldsymbol{B} = 0 \tag{2}$$

where $\boldsymbol{B}$ is the magnetic field. The third equation is Ampere–Maxwell Equation which in differential form can be expressed as

$$\nabla \times \boldsymbol{H} = \boldsymbol{J} + \frac{\partial \boldsymbol{D}}{\partial t} \tag{3}$$

where $\boldsymbol{H}$ is the magnetic field intensity and $\boldsymbol{J}$ the current density. The law states that a magnetic field is generated around a flowing electric current and a changing electric displacement field. The final equation, Faraday's law, can be expressed as:

$$\nabla \times \boldsymbol{E} = -\frac{\partial \boldsymbol{B}}{\partial t}, \tag{4}$$

where $\boldsymbol{E}$ is the electric field. It describes how a changing magnetic field induces an electric field in a closed loop, for example in a wire.

3.2 Theory of microwave generation and heat transfer

Microwaves are electromagnetic waves with frequency (f) ranging from 0.3 GHz to 300 GHz and wavelength (λ) ranging from 1 mm to 1 m. They are used for example in microwave ovens, as they heat up dipole water molecules within the heated material very efficiently (Bécherrawy, 2012). They can also be used on materials not containing water, discussed later

in **Section 3.2.2**. Other uses for microwaves are for example various telecommunication devices and technologies such as mobile telecommunications.

3.2.1 Magnetrons as a way to generate microwave radiation

Various ways to generate microwaves exist, but the most commonly used for heat generation is generating microwaves with a multi-cavity magnetron. A magnetron is a device consisting of a cylindrical vacuum tube, where a cathode, surrounded by a vacuum, is enclosed within an anode (Shinohara, 2014). The anode material is shaped so that it forms multiple cavities surrounding the cathode.

Paths of the electrons are affected by the magnetic field and with a certain value of magnetic induction, the paths become cycloidal and return to the cathode. With the right value of magnetic induction, the electrons touch the anode on the top of the trajectory. This induces a charge on the edges of the cavities. The charges oscillate as the electrons move which creates microwaves within the cathodes. The frequency of the electromagnetic waves created by the magnetron is dependent on the geometry of the resonant cavities (Shinohara, 2014). A schematic of a magnetron is presented in **Figure 1**.

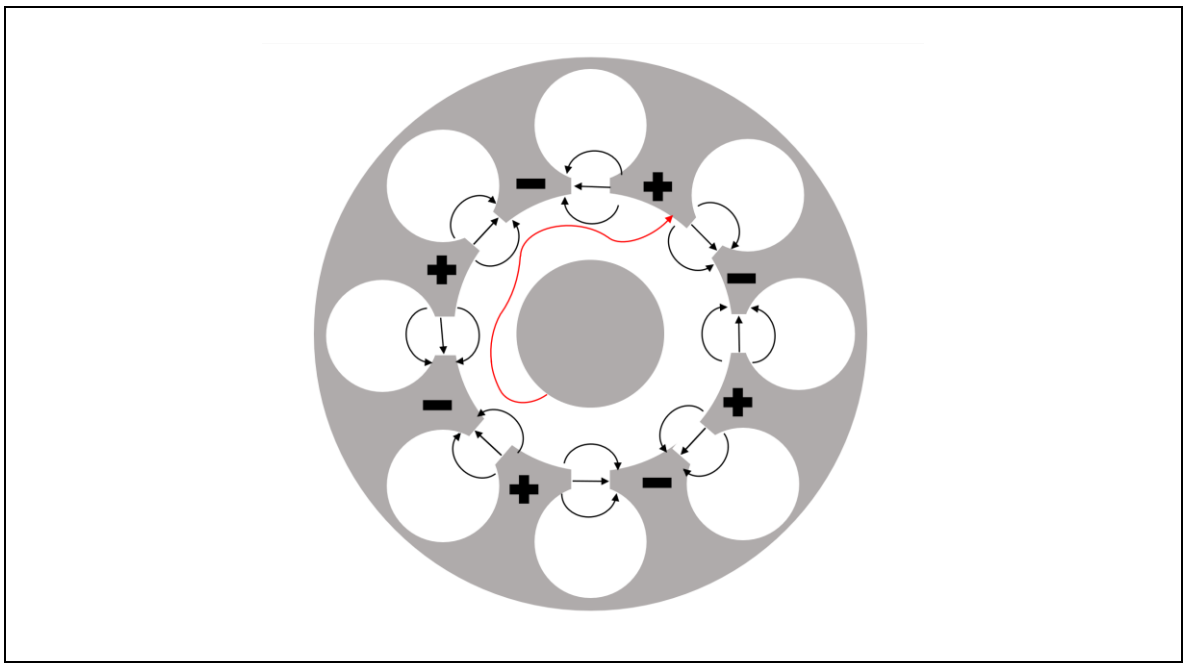

Figure 1: A crosscut of a multi cavity magnetron. The path of a electron is presented with a red colour. An electric field is induced on the edges of the cavities which affects the path of the electron.

Magnetrons are one of the most efficient sources of microwaves (Grigoriev, 2018), but their efficiency to transfer electrical energy to microwaves depends on the frequency of the generated microwaves. Lower frequencies in 1 – 5 GHz range have higher efficiencies, even over 80 %, compared to higher frequencies in 8 – 35 GHz range, where the efficiency drops to approximately 20 % (Shinohara, 2014). Thus, typical microwave ovens in domestic use operate with a lower frequency of 2.45 GHz. Even though a wide range of frequencies can be generated with different shaped magnetrons, their usage is limited. According to ITU (1998)

EM frequencies for industrial, scientific and medical (ISM) applications are restricted to certain frequency bands. Allowed bands within the microwave frequency range (0.3 – 300 GHz) that apply in the European region are 433.92 MHz, 2450 MHz, 5800 MHz, and 24.125 GHz. As 2.45 GHz is the most commonly used and operates on a high efficiency, it is also used in the numerical modelling later in this thesis.

3.2.2 Dielectric material in a changing electric field

Dielectric materials are materials that themselves contain no free electric charges, and thus act as insulators. When dielectric materials are placed within an electrical field, charged atomic particles within the material align themselves with the electric field. This phenomenon is called polarization and is fundamental for microwave heating. Polarization occurs both due to atomic particle charges and their displacement in the electric field and due to permanent asymmetrical charges of polar molecules. Polar molecules are molecules which have distinct charged ends due to different electron densities in their atoms and due to the shape of the molecules. In an electric field, the positive ends of the molecules align with the "negative side" of the electric field and vice versa. When the electric field either disappears or alternates its direction, the atomic particles either lose their polarization or polarize according to the new direction of the electric field. (Bécherrawy, 2012)

Polarization of atoms and molecules is not instantaneous, and the electric field applies work on the molecules in order to polarize them. During the polarization, the molecules undergo friction in the form of heat (Lupi, 2017). This loss is called the dielectric loss and it can be used to calculate how much an object in an alternating electric field heats up per unit volume. Next a way to calculate dielectric losses in a dielectric material is presented.

The Ampere–Maxwell, **Equation (3),** can be represented as:

$$\nabla \times \boldsymbol{H} = \sigma \boldsymbol{E} + \frac{\partial \boldsymbol{D}}{\partial t}, \tag{5}$$

where $\sigma \boldsymbol{E}$ is the conduction current density with σ being the electric conductivity of the material. The second part, $\frac{\partial \boldsymbol{D}}{\partial t}$, is the displacement current density. In a case of dielectric materials, the electric displacement field can be substituted with

$$\frac{\partial \boldsymbol{D}}{\partial t} = \varepsilon_0 \varepsilon_\mathrm{r} \frac{\partial \boldsymbol{E}}{\partial t}, \tag{6}$$

where ε_0 is the dielectric constant of a vacuum ($8.86 \cdot 10^{-12}\ F/m$) and ε_r the absolute dielectric constant. As the change in electric field in a microwave is sinusoidal periodic **(6)** can be represented in phasor form as:

$$\nabla \times \boldsymbol{H} = \sigma \dot{\boldsymbol{E}} + j\omega \varepsilon_0 \varepsilon_\mathrm{r} \dot{\boldsymbol{E}}, \tag{7}$$

where

$$\omega = 2\pi f, \tag{8}$$

and

$$j^2 = -1 \tag{9}$$

and $\dot{\boldsymbol{E}}$ represents the complex quantity of $\boldsymbol{E}$. The right-hand-side of **(7)** represents the total current density $\dot{\boldsymbol{J}}$ which is a sum of the conduction current density and the displacement current density. $\dot{\boldsymbol{J}}$ can be represented as a displacement current giving **Equation (17)** (Lupi, 2017). Dielectric constant ε_r can be substituted with a complex number:

$$\varepsilon_r = \varepsilon_r' - j\varepsilon_r'', \tag{10}$$

where ε_r' represents the real part and $\varepsilon_r''$the imaginary part of the absolute dielectric constant. Furthermore, ε_r'' can be substituted with

$$\varepsilon_r'' = \varepsilon_r' \tan(\delta), \tag{11}$$

where δ is the loss angle, an angle between the component of total current density in same phase as the electric field and the displacement current density (Lupi, 2017).
The displacement current can be represented as:

$$\dot{\boldsymbol{J}} = \omega\varepsilon_0 \frac{\sigma\dot{\boldsymbol{E}}}{\omega\varepsilon_0} + j\omega\varepsilon_0\varepsilon_r\dot{\boldsymbol{E}}, \tag{12}$$

$$\dot{\boldsymbol{J}} = -j^2\omega\varepsilon_0 \frac{\sigma\dot{\boldsymbol{E}}}{\omega\varepsilon_0} + j\omega\varepsilon_0\varepsilon_r\dot{\boldsymbol{E}}, \tag{13}$$

$$\dot{\boldsymbol{J}} = j\omega\varepsilon_0 \left(\varepsilon_r - j\frac{\sigma}{\omega\varepsilon_0}\right)\dot{\boldsymbol{E}} = \dot{\sigma}_t\dot{\boldsymbol{E}}. \tag{14}$$

When **Equations (10)** and **(11)** are substituted to **(14)**, the following equation is obtained

$$\dot{\boldsymbol{J}} = j\omega\varepsilon_0 \left(\varepsilon_r' - j\varepsilon_r'' - j\frac{\sigma}{\omega\varepsilon_0}\right)\dot{\boldsymbol{E}} = j\omega\varepsilon_0 \left(\varepsilon_r' - j\varepsilon_r'\tan(\delta) - j\frac{\sigma}{\omega\varepsilon_0}\right)\dot{\boldsymbol{E}}, \tag{15}$$

$$\dot{\boldsymbol{J}} = (j\omega\varepsilon_0\,\varepsilon_r' - j\omega\varepsilon_0 j\varepsilon_r'\tan(\delta) + \sigma)\boldsymbol{E} = (j\omega\varepsilon_0\,\varepsilon' - \dot{} j\omega\varepsilon_0 j\varepsilon_r'\tan(\delta))\dot{\boldsymbol{E}}, \tag{16}$$

$$\dot{\boldsymbol{J}} = j\omega\varepsilon_0\,\varepsilon_r'(1 - j\tan(\delta))\dot{\boldsymbol{E}}. \tag{17}$$

Complex power per unit volume of a dielectric material in a changing electric field can be calculated with

$$w_a + jw_r = \dot{\boldsymbol{E}} \cdot \dot{\boldsymbol{J}}, \tag{18}$$

$$w_a + jw_r = j\omega\varepsilon_0\,\varepsilon_r'(1 - j\tan(\delta))\dot{\boldsymbol{E}}^2, \tag{19}$$

$$w_a + jw_r = (j\omega\varepsilon_0\,\varepsilon_r' - j^2\omega\varepsilon_0\varepsilon_r'\tan(\delta))\dot{\boldsymbol{E}}^{\boldsymbol{2}}, \tag{20}$$

$$w_a + jw_r = \omega\varepsilon_0\varepsilon_r''\dot{\boldsymbol{E}}^2 + j\omega\varepsilon_0\,\varepsilon_r'\dot{\boldsymbol{E}}^2. \quad (21)$$

The energy that is transformed into heat in a dielectric material can be calculated from the real part of **(21)**:

$$w_a = \omega\varepsilon_0\,\varepsilon_r''\dot{\boldsymbol{E}}^2. \quad (22)$$

If **Equation (11)** is substituted to **(22)** it can be represented as

$$w_a = \omega\varepsilon_0\,\varepsilon_r'\tan(\delta)\dot{\boldsymbol{E}}^2. \quad (23)$$

Heat generated in form of dielectric losses in a medium is thus proportional to the frequency of the microwaves, the imaginary part of the electric permittivity, also called the loss factor and to the electric field intensity (Lupi, 2017). The loss factor is a material property of the heated object which varies later in this study based on the different minerals within the ore rocks. The loss factor is also often represented as in **Equation (23)**. Depending on the conducted experiments, either the loss factor or the tangent of the loss angle is presented for various minerals in articles and studies.

3.3 Heat transfer in rock

The relationship between parameters that are used in most thermomechanical calculations include thermal conductivity (k), specific heat capacity (c_p) and thermal diffusivity (α). The three parameters are related to each other with

$$\alpha = \frac{k}{\rho c_p}, \quad (24)$$

where ρ is the density of the material. Thermal conductivity represents how heat flows through a medium whereas the specific heat capacity represents how heat is stored within the material. Thus, thermal diffusivity can be understood as the ratio of how fast thermal changes occur in a medium. With a high thermal diffusivity, the ratio between thermal conductivity and the specific heat capacity is high and thus heat propagates faster through the material. If the thermal diffusivity is low, heat applied to the material is stored and only slowly propagates through it. The main modes of heat transfer are thermal conductivity, convection and radiation. As thermal conductivity applies for the numerical modelling it is discussed more in the following.

Conduction occurs, when the internal energy of a medium causes its atomic particles to move and collide with each other. It occurs either in solids or motionless fluids. Particles with more energy lose their energy to adjacent particles with lower energies (Sidebotham, 2015). On a macroscopic level, the movement of atomic particles is measured as temperature T which can be represented as a scalar field function of space, $T(x, y, z)$. The changes within the scalar field T can be represented as a temperature gradient

$$\nabla T = \left(\frac{\sigma T}{\sigma x} + \frac{\sigma T}{\sigma y} + \frac{\sigma T}{\sigma z}\right). \tag{25}$$

Heat is transferred from areas of high temperature to areas with low temperature and can be calculated using Fourier's law (Hahn and Özisik, 2012):

$$\boldsymbol{q} = -k\nabla T \tag{26}$$

where $\boldsymbol{q}$ (W/m²) is the heat flux in the material. Heat conductivity is a scalar quantity for continuous, isotropic materials. All minerals used later in this study are considered isotropic and their thermal conductivities are presented in **Section 5.2.1** and **Section 5.3.3** for both numerical models separately. Isotropic materials are materials with constant properties in all spatial directions.

3.4 Heat transfer balance equation in COMSOL

First law of thermodynamics, the law of conservation of energy, can be used to calculate in how heat is transferred in a continuous medium. The law is represented as:

$$\Delta E^* = Q_{in} - W_{out}, \tag{27}$$

where ΔE^* is the change of the internal energy of a system, Q_{in} is heat entering the system and W_{out} work that leaves the system (Karwa, 2017). Next the formulation of **Equation (27)** is presented in the same form as it is used in COMSOL. **Equation (27)** can be represented as a function of changes in internal energy, kinetic energy K, power of forces applied to the system P_{ext}, and the heat exchanged by the system with its environment Q_{exh} (COMSOL, 2018a) as in:

$$\frac{dE^*}{dt} + \frac{dK}{dt} = P_{\text{ext}} + Q_{\text{exh}}. \tag{28}$$

The forces applied to the system can also be represented as:

$$P_{\text{ext}} = \frac{dK}{dt} + P_{\text{str}}, \tag{29}$$

where P_{str} is stress power. When **Equation (29)** is inserted into **Equation (28)**, the following equation is obtained:

$$\frac{dE}{dt} = P_{\text{str}} + Q_{\text{exh}} \tag{30}$$

A localized form of the heat balance equation can be derived when the following three equations are combined with **Equation (30)**:

1)

$$\frac{dE^*}{dt} = \int \rho \frac{dE_s^*}{t} dv, \tag{31}$$

where E_s^* is the internal energy per unit mass.

2)

$$P_{str} = \int (\boldsymbol{\sigma} : \boldsymbol{D}^*)\, dv, \tag{32}$$

where $\boldsymbol{\sigma}$ is the Cauchy stress tensor representing force acting in the deformed configuration and $\boldsymbol{D}^*$ the strain rate tensor which represents how the material is deforming in each of its points in a certain time.

3)

$$Q_{exh} = -\int (\boldsymbol{q} \cdot \boldsymbol{n})\, ds - \int (\boldsymbol{q}_r \cdot \boldsymbol{n}) ds + \int Q_{add}\, dv\,, \tag{33}$$

where Q_{add} represents additional heat sources, such as heat transferred by microwave radiation. Thus, the heat transfer equation, **Equation (30)**, becomes:

$$\int \rho \frac{dE_s^*}{t} dv = \int (\sigma : \boldsymbol{D})\, dv - \int (\boldsymbol{q} \cdot \boldsymbol{n})\, ds - \int (\boldsymbol{q}_r \cdot \boldsymbol{n}) ds + \int Q_{add}\, dv\,, \tag{34}$$

which can be either represented in the material frame, where the coordinate system is fixed to the observed material:

$$\rho \frac{dE_s^*}{t} + \nabla \cdot (\boldsymbol{q} + \boldsymbol{q}_r) = \sigma : \boldsymbol{D} + Q_{add} \tag{35}$$

or in the spatial frame, where the coordinate system in fixed in space:

$$\rho \frac{\partial E_s^*}{t} + \rho \boldsymbol{u} \cdot \nabla E_s^* + \nabla \cdot (\boldsymbol{q} + \boldsymbol{q}_r) = \sigma : \boldsymbol{D} + Q_{add}, \tag{36}$$

where $\boldsymbol{u}$ represents the velocity field. E_s^* can be represented as a function of T and the specific heat capacity of the material C_p:

$$\frac{dE_s^*}{t} = C_p \frac{dT}{t}. \tag{37}$$

Finally, **Equation (36)** can be derived into the following form used in calculations for heat transfer in solids within COMSOL Multiphysics:

$$\rho C_p \left(\frac{\partial T}{t} + \boldsymbol{u} \cdot \nabla \mathrm{T}\right) + \nabla \cdot (\boldsymbol{q} + \boldsymbol{q}_r) = -\alpha T : \frac{d\boldsymbol{S}}{dT} + Q_{add}, \tag{38}$$

where $\boldsymbol{S}$ is the second Piola-Kirchhoff stress tensor. However, as the effect of radiative heat transfer outwards from the solid is omitted, **Equation (38)** simplifies to:

$$\rho C_p \left(\frac{\partial T}{t} + \boldsymbol{u} \cdot \nabla \mathrm{T}\right) + \nabla \cdot \boldsymbol{q} = -\alpha T : \frac{d\boldsymbol{S}}{dT} + Q_{add}, \tag{39}$$

Combining **Equation (39)** with **Equations (22)** and **(26)** gives the final equation which combines heat transfer via microwave radiation and heat transfer in the rock sample as in:

$$\rho C_{\mathrm{p}}\left(\frac{\partial T}{t}+\boldsymbol{u}\cdot\nabla\mathrm{T}\right)-\nabla\cdot k\nabla T,=\ \omega\epsilon_{\mathrm{r}}{}''\varepsilon_0\boldsymbol{E}^2. \tag{40}$$

3.5 Elastic rock stress-strain relationship and its application in COMSOL

As the sample is heated up with microwave heat losses, it undergoes thermal expansion. This expansion induces stresses within the rock sample. In this section, the relationship between the thermal strains and stresses is explained. The rock strength criterion is also addressed. Even though rock failure is not modelled in the numerical model, understanding the principles is necessary in order to analyse the impact of the results.

3.5.1 Hooke's law

If a material is put under sufficient load, it undergoes deformation, or in other words changes in the materials dimensions. If the load, and thus the stress within the material, is below a certain threshold, the deformed material returns to its initial form after the load is lifted (Chung and Myoung-Gyu, 2018). Such stress-strain relationship is called elastic deformation. Hooke's law describes the relationship between stress and strain (ϵ) in a uniaxial stress case as (Chou and Pagano, 1967):

$$\boldsymbol{\sigma}=Y\epsilon \tag{41}$$

where Y is Young's modulus. It is worth noting that Hooke's law only applies in the elastic region of strain. In a more general case, where the stress is not uniaxial and shear stress, and shear strain apply, Hooke's law in tensor notation can be represented as

$$\boldsymbol{\sigma}_{ij}=\frac{Y}{(1+\nu)}\left[\boldsymbol{\epsilon}_{ij}+\frac{\nu}{(1+2\nu)}\delta_{ij}\boldsymbol{\epsilon}_{kk}\right], \tag{42}$$

where i, j and k take the values 1, 2 and 3. Poisson's ratio (ν) describes the relation between strain and the stresses parallel and perpendicular to it. The Kronecker delta (δ_{ij}) gains the following values:

$$\delta_{ij}=\begin{cases}0\ if\ i\ \neq j\\ 1\ if\ i=j\end{cases}. \tag{43}$$

All stress configurations can be rotated so that no shear stress components exist. In such a rotated state, the stress is expressed as three stress components, called principal stresses ($\sigma_1,\sigma_2,\sigma_3$). The principal stress values are calculated as the eigenvalues of the stress tensor and the directions of the principal stresses as the eigenvectors of the stress tensor. The resulting principal stresses thus depend on the stress tensor used. From now on in this thesis, the principal stresses are considered as the eigenvalues of **Equation (42)**.

Equation (42) can be represented in matrix notation as:

$$\boldsymbol{\sigma} = \frac{Y}{(1+\nu)}\left[\boldsymbol{\epsilon} + \frac{\nu}{(1+2\nu)} tr(\boldsymbol{\epsilon})\boldsymbol{I}\right]. \quad (44)$$

As the material is assumed linear elastic, the strain $\boldsymbol{\epsilon}$ is the elastic part of the strain, calculated with:

$$\boldsymbol{\epsilon} = \boldsymbol{\epsilon}_{\mathbf{tot}} - \boldsymbol{\epsilon}_{\mathbf{inel}}, \quad (45)$$

where $\boldsymbol{\epsilon}_{\mathbf{tot}}$ is the total strain and $\boldsymbol{\epsilon}_{\mathbf{inel}}$ the inelastic strain. In the case of this thesis, the inelastic strain component consists of strain caused by thermal expansion of the rock thermal strain $\boldsymbol{\epsilon}_{\mathbf{th}}$ as:

$$\boldsymbol{\epsilon}_{\mathbf{inel}} = \boldsymbol{\epsilon}_{\mathbf{th}} = \alpha_{\mathrm{V}} \Delta T, \quad (46)$$

where the coefficient of thermal expansion, α_{V}, is a material property and ΔT the difference in temperature within the material. COMSOL considers thermal strain to be inelastic, as it is only reversable if the heat is removed from the system. Thus, during heating up for example a rock sample, the thermal strain acts as an inelastic strain.

Thus the equation solved by COMSOL is:

$$\boldsymbol{\sigma} = \frac{E}{(1+\nu)}\left[(\boldsymbol{\epsilon}_{\mathbf{tot}} - \boldsymbol{\epsilon}_{\mathbf{th}}) + \frac{\nu}{(1+2\nu)} tr(\boldsymbol{\epsilon}_{\mathbf{tot}} - \boldsymbol{\epsilon}_{\mathbf{th}})\boldsymbol{I}\right]. \quad (47)$$

The stress-strain relationship can also be represented as a double dot product between the stiffness tensor ($\boldsymbol{C}$) and the elastic strain tensor $\boldsymbol{\epsilon}_{\mathbf{el}}$:

$$\boldsymbol{\sigma} = \boldsymbol{C} : \boldsymbol{\epsilon}_{\mathbf{el}}. \quad (48)$$

3.5.2 Rock failure criterion

Rock can be divided into two classes, when assessing its strength. The first class is intact rock in which the rock is assumed to be fully continuous. The second class, rock mass, considers rock as a larger element, where all cracks and fractures within the rock are considered and thus simplification of the rock to a continuous mass does not apply (Brady and Brown, 2004). Intact rock class can be applied when the rock is observed on a small scale, such as small rock samples studied in this thesis. Thus, the assumption of intact rock material is used throughout this study.

In the previous section it was discussed how low stresses on a material cause reversible deformation. When loads are sufficiently large, the deformation turns from elastic deformation to plastic deformation as the material yields to stress. As opposed to linear deformation, plastic deformation is permanent and is not reversed when the load on the material is lifted. In the simplest case, the deformation turns to plastic, when a certain stress threshold, yield strength, is surpassed (Chung and Myoung-Gyu, 2018).

Parameters such as Young's modulus and Poisson's ratio discussed in the previous section are typically determined with a tensile test. In another material strength test, conducted typically on rock, the uniaxial compressive test, the material is loaded axially from one direction under it yields (Brady and Brown, 2004). In addition to Young's modulus and Poisson's ratio, the peak of uniaxial compressive strength σ_c can be determined.

However, a simple yield criterion cannot represent a load on a material, where multiaxial stress is applied. In multiaxial stress conditions, the affecting stresses confine the rock and increase its strength when compared to a uniaxial stress case. Such stress states are not only present in underground conditions of rock mass (Brady and Brown, 2004) but also both within a rock with a non-uniform internal thermal expansion and in rock comminution processes.

In a multiaxial stress case, the rock strength can be represented with a peak strength criterion. This criterion in its most basic form is a relationship between first and third principal stresses within the material and can be represented as (Brady and Brown, 2004):

$$\sigma_1 = f(\sigma_3). \tag{49}$$

In other words, the relationship defines a combination of principle stresses that exceed the strength of the material in a confining state. Different strength criterions for multiaxial stresses exist for rock and the most common ones are discussed next.

Mohr-Coulomb criteria combines normal stress (σ_n) to shear stress and states that failure on a material occurs on a failure envelope with the slope $\tan(\phi)$ as stated by:

$$\tau = \sigma_n \tan(\phi) + c, \tag{50}$$

where ϕ is called the angle of internal friction and c the cohesion of the material. The normal stress can be calculated with

$$\sigma_n = \frac{1}{2}(\sigma_1 + \sigma_3) + \frac{1}{2}(\sigma_1 - \sigma_3)\cos(2\beta), \tag{51}$$

where β is the angle defined by the Mohr circle, a circle with a diameter of $\sigma_1 - \sigma_3$ and the failure envelope visualized in **Figure 2.** In **Figure 2** T_0 represents the tensile cut-off which is applied, as in general, rock has a very weak tensile strength (Brady and Brown, 2004).

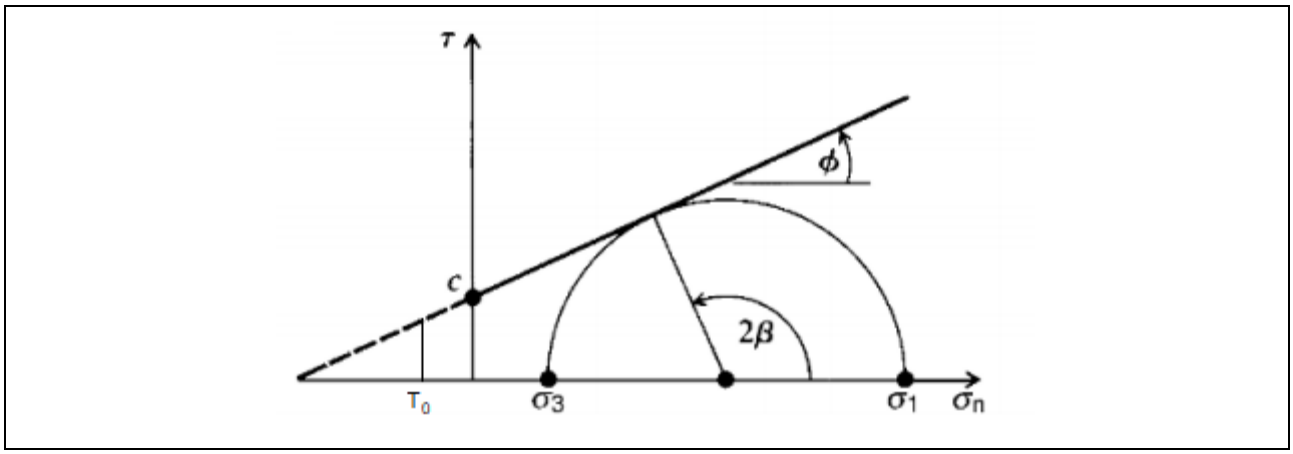

Figure 2: Visualization of the Mohr-Coulomb failure criterion. Modified after (Brady and Brown, 2004)

Brady and Brown (2004) however state that the Mohr-Coulomb yield criterion is not a sufficient strength criterion for rock, as it states that strength envelopes are linear across all stress combinations. This does not apply in a general case and thus a more accurate failure criterion has been developed. The Hoek–Brown yield criterion is based on empirical data. The criterion can be used for both rock mass and intact rock for which it is represented as:

$$\sigma_1 = \sigma_3 + \sqrt{m_i \sigma_c \sigma_3 + \sigma_c^2}, \tag{52}$$

where m_i is an empirical parameter of intact rock, varying with different rock types.

As a summary, high enough stresses can cause damage to a material. However, determining, when elastic deformation transforms to plastic deformation requires specific material parameters. Such parameters are not well defined for all minerals. Thus, later in this study, when the microwave heating induces stresses to the material, all deformations are considered elastic.

3.6 Rock comminution process

Rock comminution is the process of breaking down rock mass, such as rock beds in a mine, step by step to smaller particle sizes. Smaller particle size is used to liberate for example the valuable minerals from the surrounding gangue minerals. This process typically starts by extracting ore from the mine by different means such as explosives. This is followed by crushing and grinding the mineral to smaller particle sizes within a mineral processing plant (Wills, 2006). Crushing is conducted with various ways of compressing the rock. In a jaw crusher the ore is compressed between a pivoting and a fixed jaw, whereas in a gyratory crusher, the compression occurs between a rotating spindle and a conical crushing chamber.

Grinding on the other hand is based on abrasion or impact between the rock and some other media depending on the type of the grinder. Two general types of grinding mills exist. The first type are mills where the ore is put in a rotating mill shell. The grinding occurs, when the ore rotates and collides with either other rocks or steel balls or rods. The second type are

stirred mills, where the ore is put within a fixed mill shell and the rotation is induced with a rotating stirrer. Again, the rock is crushed as it impacts either with itself or other grinding media (Wills, 2006).

Typical size distributions in an ore comminution process are as follows: the extracted ore from the mine can hold particles up to a size of approximately 1.5 m in diameter. In crushing the particle size is reduced to a range of 10 – 20 cm and finally in grinding, depending whether the ore is coarsely or finely grinded, all the way to a range of 40 – 300 μm or 15 – 40 μm (Wills, 2006). At the same time, as the particle size is reduced, the ore rock distribution turns from very heterogenous to a more homogenous size and composition. The ore originating from the mine has a wide range of particle sizes that have discontinuities, such as fractures and cracks in them. The smaller particles produced the comminution process, are in the other hand both more homogenous in size and have less discontinuities within.

If induced stresses reach high enough thresholds, microwave radiation can be used to decrease rock strength. If the energy consumed by the microwave irradiation is less than the energy saved during rock comminution, a net saving of energy can be achieved. However, calculating and modelling the energy saved during the comminution process is outside the scope of this study.

4 Assessment of dielectric properties of various ore minerals

Aim of this section is to present the ore minerals of most operational mines in Finland and present the dielectric properties of the minerals. The rock sample used in the second numerical model is also chosen based on the various minerals presented here.

Dielectric parameters, including ϵ_r, ϵ_r', ϵ_r'' and tan (δ) determine how great heat losses occur in a material under microwave radiation. Higher values result in higher heat losses as can be seen from **Equation (22)** and **Equation (23)**. The stress-strain state of the rock is dependent both on the temperature change within and the coefficient of thermal expansion as stated by **Equation (46)**. Thus, materials with a higher α_V expand more per a unit of temperature change and cause larger stresses in the rock. The temperature change is also dependant on the specific heat capacity and density of the material. Other factors, such as Young's modulus, Poisson's ratio, internal angle of friction and cohesion of the material also play a role when determining the thermal response of the rock to the microwave radiation.

Determining minerals where microwave radiation undergoes large heat losses helps to focus the numerical modelling on minerals that heat up significantly under microwave radiation. Thus, other parameters affecting the stress states resulting from the increased temperature can be studied in more depth in the modelling.

Assessment in this section is conducted on ore rocks of currently operational mines of Finland as the availability of rock samples to digitize is better for Finnish samples. Additionally, the mining industry are the most probable utilizers of technologies that decrease energy consumption of ore comminution. However, as specific rock samples of operating mines are mostly classified, the ore sample for the numerical modelling in the second numerical model is chosen from Aalto's collection and does not necessary represent any single mine currently operating in Finland.

A rock sample in the second numerical model should consist of minerals with high dielectric losses. However, availability of rock samples for digitization also pays a role and thus the sample is selected with from samples available. The research conducted should still give valuable insight and preliminary information on what types of minerals might be suitable for microwave treatment.

Currently, there are 11 operational metal ore mines in Finland (Vasara, 2019). The Pyhäsalmi mine is however reaching the end of its mine life in 2021. The Kylylahti mine is also reaching the end of its mine life. Both mines have nevertheless been considered in this section. Additionally, the upcoming spodumene-pegmatite mine is also considered, as the mine project is in active development, and they have filed an environmental permit application in late 2020. Most of the assessed mines extract sulfidic minerals with the exceptions being Elijärvi mine, where chromite is mined and the Keliber mine. The mines and their respective ore minerals are presented in **Table 1**.

All major ore minerals considered in this assessment are defined from the most common ore minerals of the mines in **Table 1**. As a comprehensive characterization of dielectric

properties of various minerals has not been conducted, the mineral properties in **Table 2** have been compiled from multiple studies. Thus, different values for ϵ, ϵ', ϵ" and tan (δ) are presented for a single mineral based on various studies. It is worth noting that the availability on studies of dielectric properties of minerals is very limited and thus all properties for all ore minerals are not presented.

Table 1: Major ore minerals of operational Finnish mines

Mine	Major Ore mineral	Source
Kittilä	Arsenopyrite, arsenic-rich pyrite	(Doucet *et al.*, 2010)
Kemi	Chromite	(Alapieti and Kärki, 2005)
Jokisivu	Gold hosted in quartz-veined diorite, surrounded in mica	(Dragon Mining Limited, 2020)
Orivesi	strongly deformed, andalusite rich silicified zones	(Dragon Mining Limited, 2014)
Pyhäsalmi	Chalcopyrite, Pyrite, Sphalerite, Pyrrhotite	(Geological Survey of Finland, 2021c)
Sotkamo	chalcopyrite, sphalerite, pentlandite, pyrrhotite	(Reino and Pekkarinen, 1989)
Pampalo	Pyrite, additionally free gold at grain boundaries	(Geological Survey of Finland, 2021b)
Kylylahti	Chalcopyrite, Pyrite, Pyrrhotite	(Geological Survey of Finland, 2021a)
Kevitsa	chalchopyrite-pentlandite assemblage, pentlandite-millerite assemblage, Bi-tellurides and sperrylite	(Gray, Cameron and Briggs, 2016)
Laiva	quartz-sulphide: arsenopyrite, pyrrhotite, chalcopyrite, gold as free grains	(Bektas and Vathavooran, 2019)
Taivalhopea	pyrite, pyrrhotite, sphalerite and galena, dyscrasite, freibergite, electrum	(Sotkamo Silver, 2021)
Keliber	Spodumene-pegmatite	(Sweco Industry Oy, 2016)

According to Schubert (2015), most minerals have low dielectric constants and thus are not readily affected by microwave radiation. Some minerals such as pyrite and galena however have dielectric constants close to water and are heated up significantly under microwave radiation. They also present dielectric constant for some common minerals. The dielectric parameters they determined for galena and pyrite are presented in **Table 2**. Furthermore, Haque (1999) compiled data of various microwave heating experiments on the rock. The results show that arsenopyrite, pyrite, chalcopyrite, galena and pyrrhotite heated rapidly under microwave radiation, whereas minerals such as chromite and sphalerite do not.

Lovás *et al.* (2010) determined both ϵ_r' and ϵ_r" values for chalcopyrite, pyrite and galena in a temperature ranging from 20 ^{o}C to 1000 ^{o}C with 2.2 GHz microwave frequencies. Both the real and imaginary part of the dielectric constant remained relatively constant for a temperature ranging from 20 ^{o}C to 200 ^{o}C for chalcopyrite, 20 ^{o}C to 450 ^{o}C for pyrite and 20 ^{o}C to 300 ^{o}C for galena. The values of dielectric permittivities for the studied minerals are presented in **Table 2**. It is worth noting that the dielectric permittivities raised significantly after heating the samples above the aforementioned temperature ranges as the minerals underwent phase transforms.

Church, Webb and Salsman (1988) determined the dielectric properties of various minerals with microwave frequencies ranging between 300 and 1000 MHz. Their study shows that the dielectric constant is not greatly affected by the varying frequencies or temperatures, whereas the loss tangent for some materials changes drastically. The imaginary parts of dielectric constant and the respective loss tangents for chromite, sphalerite and spodumene at approximately 1 GHz determined in their study are presented in **Table 2**.

Salsman (1992) determined the dielectric properties of chalcopyrite at various frequencies and temperatures. Their research shows that the imaginary part of the dielectric constant gradually decreases when the frequency of the microwave radiation is increased. When the frequency is increased to approximately 2.4 GHz ϵ_r" reaches a value of 10 at 25 ^{o}C and a value of 15 at 200 ^{o}C. They also determined the value for the real part of the dielectric constant, being approximately 12 at the same frequencies and temperatures. They found out that the changes in dielectric properties were at least partly caused by phase changes in the mineral.

Peng *et al.* (2014) determined both the real and imaginary part of the dielectric constant for pyrite via a cavity perturbation technique. The values were determined with both 915 MHz and 2450 MHz microwave frequencies in a temperature range from 20 ^{o}C to 500 ^{o}C. They found out that both parameters increase steadily until a temperature of 450 ^{o}C is reached. After this temperature, the pyrite begins to decompose and both values increase very rapidly. They found out that ϵ_r' increased from about 50 to 75 before from 20 ^{o}C to 450 ^{o}C while ϵ_r" grew from 10 to 45 in the same temperature range and in a frequency of 2450 MHz. It is worth noting that ϵ_r" stayed very close to 0 between 20 ^{o}C to 150 ^{o}C when heated up with the lower frequency microwave radiation.

Marland, Merchant and Rawson (2001) determined dielectric properties of minerals associated with coal in various frequencies. The properties were determined for 0.615 GHz, 1.413 GHz and 2.216 GHz in both 60^{o}C and 180^{o}C. The values for pyrite in 2.216 GHz microwave frequency in both temperatures are presented in **Table 2**.

Harrison, (1997) determined dielectric properties of multiple minerals for 650W, 2.45 GHz microwave radiation. The measurements were undertaken with an open-ended coaxial line sensor, a probe used commonly to measure dielectric properties. They determined that ore minerals such as pyrites, galena and pyrrhotite absorb microwave radiation readily, whereas minerals such as quartz and sphalerite are transparent for the radiation. Values determined in their study for chalcopyrite, galena and pyrite are presented in **Table 2**.

Goldbaum *et al.* (2020) conducted permittivity tests on pyrrhotite samples from three different tailings sources. The tailings were dried to remove all moisture. The experiments were conducted with multiple frequencies and 1200 W microwave power. The experiments indicated a rapid response to microwave radiation and heated readily. The real and imaginary permittivities of the samples increased from room temperature until 850^{o}C. The permittivities grew fairly linearly in 20 – 200^{o}C range and are presented for 2.45 GHz frequency in **Table 2**.

Finally, Zheng *et al.* (2020) conducted a comprehensive study on dielectric properties of various minerals, including common ore minerals. The tests were undertaken with a 2.45 GHz frequency for different densities for each mineral. Dielectric properties of Galena, determined in their study, are presented in **Table 2**.

Table 2: Dielectric properties of ores common in Finnish mines

Mineral	ϵ_r	ϵ_r'	ϵ_r''	$\tan(\delta)\ [\cdot 10^{-4}]$	**source**
Arsenopyrite	>81				(Rosenholtz and Smith, 1936)
Bi-tellurides					NA
Chalcopyrite	>81[(2)]	10 - 15 [(1)] 12 [(3)] 4.75 [(4)]	0.25 [(1)] 10 [(3)] 0.26 [(4)]		[(1)] (Lovás *et al.*, 2010) [(2)] (Rosenholtz and Smith, 1936) (Salsman, 1992) [(3)] (Harrison, 1997) [(4)]
Chromite	11.03[(1)]	10.96[(2)]	0.0016	1.45[(2)]	(Rosenholtz and Smith, 1936) [(1)] (Church, Webb and Salsman, 1988) [(2)]
Galena	17-81[(1)]	8[(2)] 6.75 [(3)] 49.54 [(4)]	0.1[(2)] 0.12 [(3)] 1.462 [(4)]		(Schubert, 2015) [(1)] (Lovás *et al.*, 2010) [(2)] (Harrison, 1997) [(3)] [(4)] (Zheng *et al.*, 2020))
Pyrite	34-81[(1)]	8 [(2)] 8.25 [(3)] 7.07 – 7.58[(4)]	0.1 [(2)] 1.0 [(3)] 1.0625 – 1.2353[(4)]		(Schubert, 2015) [(1)] (Lovás *et al.*, 2010) [(2)] (Harrison, 1997) [(3)] [(4)](Marland, Merchant and Rawson, 2001)
Pyrrhotite	> [(1)] 81	[(2)] 20 - 180	[(2)] 6 – 70		[(1)] (Rosenholtz and Smith, 1936) [(2)] (Goldbaum *et al.*, 2020)
Sperrylite					NA
Sphalerite	5.29[(1)]	9.66[(2)]	0.007	7.36[(2)]	(Rosenholtz and Smith, 1936) [(1)] (Church, Webb and Salsman, 1988) [(2)]
Spodumene		6.98	0.0007	1.04	(Church, Webb and Salsman, 1988)

*(20 – 200 °C)
**(20 – 450 °C)
***(20 – 300 °C)

From the studies, it is evident that the dielectric properties of minerals are strongly dependent on measurement temperatures and frequencies. This is also evident from the large differences in dielectric properties of a single mineral measured in slightly different frequency-

or temperature ranges. Thus, determining which ore type is unanimously best suited for microwave assisted weakening is difficult.

Values for ϵ_r ϵ_r' ϵ_r" for pyrite, arsenopyrite, chalcopyrite, galena and pyrrhotite are considerably higher than the other minerals presented in **Table 2.** All of the aforementioned minerals belong to the sulphide minerals group. Thus, the mineral modelled in the second numerical model should also come from a sulphide mineral deposit.

A sample from Pyhäsalmi mine was selected from the Aalto University collections, as the sample contains pyrite, chalcopyrite, pyrrhotite and sphalerite. All the minerals have relatively high relative permittivities. The mineral properties are discussed more in detail in **Section 5.3.3**.

5 Description of the numerical modelling

This section aims to provide all methods and information to prepare and set up a numerical model capable of modelling microwave heating of a rock sample. The modelling is conducted with a finite element model (FEM). In FEM, a model geometry is discretized into smaller mesh-elements for which the electromagnetic and heat transfer equations are solved. Discretizing the problem into smaller elements makes it possible to solve complicated equations for complex geometries consisting of multiple different materials. As discussed earlier, two separate models are created.

Both models consist of similar geometries and general numerical model settings which are presented in **Sections 5.1.1** and **5.1.2**. In both models, a rock sample is inserted in a rectangular microwave oven domain, filled with air. The microwave oven geometry is shared between the models. The major difference is that in the first model, the inserted rock sample is a cubical, symmetrical shape, whereas in the second model the sample is thinner and consist of irregular minerals.

In the first model, a simplified geometry of a rock sample is created. This setup is used determine how different radiation and material parameters influence the induced stresses in the sample. The geometry of the sample does not represent any real mineral and rock configuration but should still represent general influences of the various parameters. This setup is used, as it allows isolating the effect of various aspects of the microwave heating progress. For example, changing the ratio between microwave-absorbing minerals to non-microwave-absorbing minerals is complicated with a sample consisting of realistically shaped minerals, while it is very simple to do in a simulated geometry.

In the second model, the selected ore rock sample (see **Section 4)** is digitized and a microwave heating of the sample is modelled. This model is used to assess how stresses are induced in a realistic rock sample geometry. The results can be used to preliminary assess the viability of microwave-assisted rock comminution for a sulfidic ore.

5.1 Numerical model setup shared in both models

In this section, the shared numerical modelling aspects of both models are presented. Both models follow a similar workflow of modelling. The models share the governing equations, boundary conditions, numerical solvers, and the microwave geometries. The larger differences between the models consist of differently shaped rock geometries, different material parameters and different microwave radiation settings. These aspects are defined separately for both models in **Sections 5.2** and **5.3.**

5.1.1 Numerical modelling setup

Aim of the numerical model is to simulate the microwave heating of a rock sample. This approach applies for both models. Multiple physics modules are used to couple the applied electric field and the heating of the rock sample. The thermal response of the sample is also considered. In principle, first the electromagnetic field is calculated throughout the model

for a certain time step, this is followed by the calculation of the dielectric losses in the rock. The dielectric losses act as a heat source in the minerals and thus cause a temperature distribution within. The increased temperatures cause thermal expansion in the minerals leading to increased stresses in the model.

The individual tasks are performed with different physics modules of COMSOL. *Electromagnetic Waves, Frequency Domain* -module, is used to model a microwave input port and the resulting electromagnetic field on the studied sample. The *Heat Transfer in Solids* -module is used to model the heat response of the rock sample to the microwave radiation. Finally, the *Solid Mechanics* -module is used to determine the thermal effect on the mechanics of the rock. The mathematical model describing each module in detail is discussed later in this section. The flow chart of the modelling is presented in **Figure 3**.

In the numerical model geometry, the rock sample in both models is placed within an enclosed copper casing with a small opening functioning as the input of microwave radiation. This setup is used to simplify a small domestic microwave oven, where the sample is heated. This does not represent an industrial scale microwave oven, as the detailed geometry of such devices is outside of the scope of this study. As the main focus is on heating the sample, a simple geometry presented individually for both models, is considered adequate.

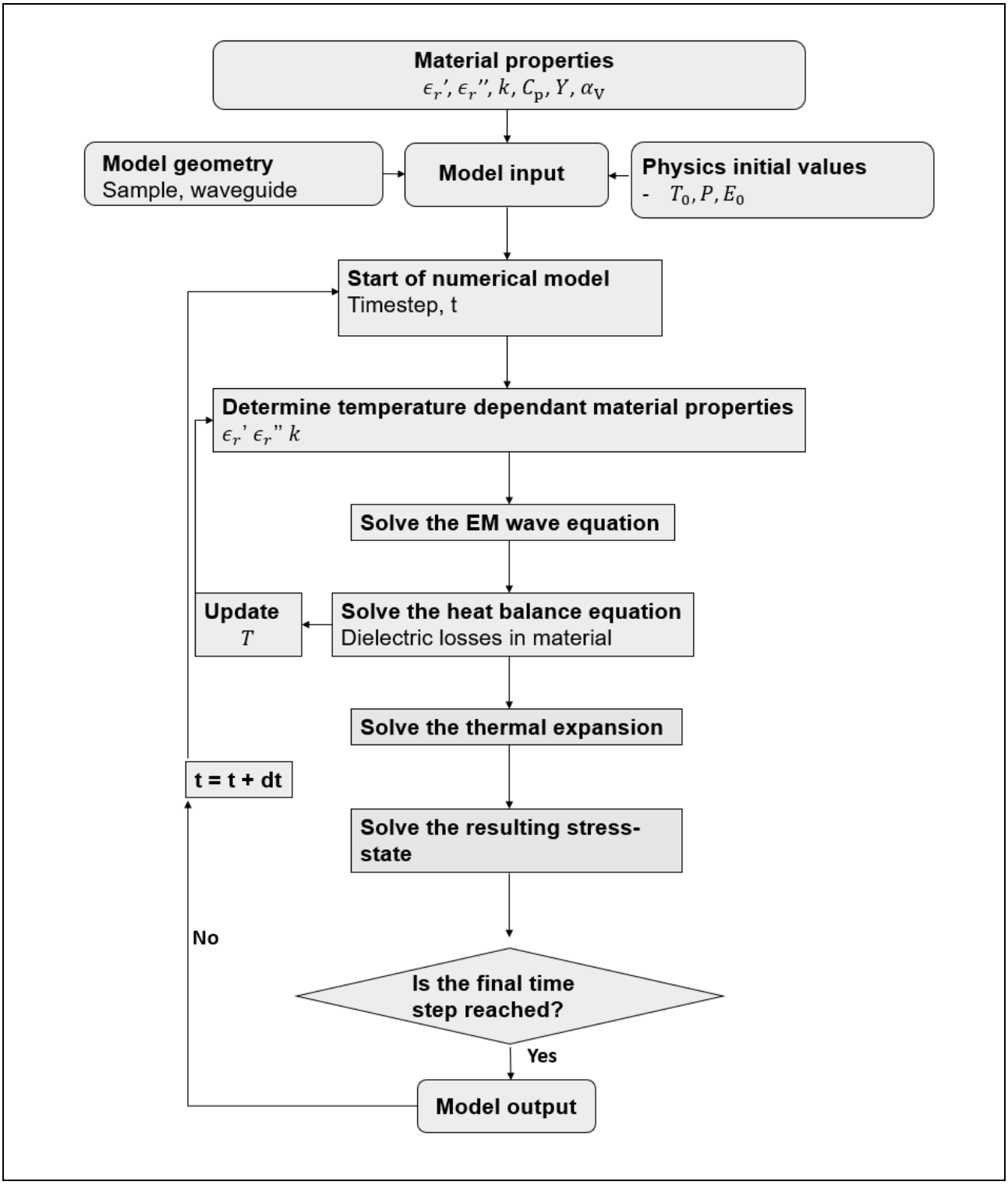

Figure 3: The flowchart of the numerical model.

5.1.2 Mathematical model

Theory of microwave heat transfer was discussed in detail in **Section 3.2**. In this section, governing equations of the numerical models are presented. These equations are pre-defined in each physics module of COMSOL but can be tailored for various applications. The equations in this section are formulated as they appear in COMSOL, but the theory presented in **Section 3** applies throughout.

The electromagnetic wave equation describes how the electric field interacts with the geometric model. It is introduced to the model within the *Electromagnetic Waves, Frequency Domain*-module. It is represented with

$$\nabla \times \mu_{\mathrm{r}}^{-1}(\nabla \times \boldsymbol{E}) - \omega^2 \varepsilon_0 \mu_0 \varepsilon_{\mathrm{r}} \boldsymbol{E} = 0, \tag{53}$$

where μ_0 is the permeability of a vacuum and μ_{r} the relative permeability of the material. The heat balance equation describes how heat is transferred throughout the model. The heat balance equation is introduced within the *Heat transfer in solids* -module. It is represented as **Equation (38)**

When coupling the electromagnetic wave equation and the heat balance equation, the Q_{add} can be represented as a sum of resistive and magnetic losses. In COMSOL, the resistive losses are represented as

$$Q_{\mathrm{rh}} = \frac{1}{2} Re(\boldsymbol{J} \cdot \boldsymbol{E}^*). \tag{54}$$

Equation(21) can be inserted within the brackets and thus the total heat balance equation gains the form as in **Equation (39)**.

Furthermore, the thermomechanical response of the rock is modelled. Thus, the *Solid mechanics*-module is introduced to the model. In this model, the material is assumed to be linear elastic and fully isotropic. The material is also considered to be fully continuous so that no fractures or discontinuities are present. Finally, the effect of gravity is omitted. The rock sample is very small, and the mechanical effect of gravity is considered to be negligible. The force balance equation can then be represented as:

$$\nabla \cdot \sigma = 0, \tag{55}$$

where

$$\sigma = C : \varepsilon_{\mathrm{el}} \tag{56}$$

In addition to the governing equations a set of boundary and initial conditions are applied to the model. The initial electric field throughout the model is assumed to be 0. The electric field is introduced as a rectangular port boundary condition on the waveguide intake on the top part of the model. The port input power can be varied and the used input power is presented separately for each numerical model in **Sections 5.2 and 5.3**. The port mode is set to be transverse electric, where the electric field of the microwave is perpendicular to the

direction of the wave, while the magnetic field is towards the wave direction. The mode number is set to 10. The port boundary condition is represented with

$$S = \frac{\int_{\partial\Omega}(\boldsymbol{E} - \boldsymbol{E_1}) \cdot \boldsymbol{E_1}}{\int_{\partial\Omega} \boldsymbol{E} \cdot \boldsymbol{E_1}}, \tag{57}$$

where S is the scattering parameter or S-parameter of the port and $\boldsymbol{E_1}$ the corresponding electric field pattern (COMSOL, 2018b).

An impedance boundary condition is applied on the copper casing. This boundary condition ensures that microwave radiation does not penetrate deeply to the casing. The boundary condition lessens the computational intensity of the modelling, as it simplifies the radiation penetration so that the casing can be modelled as a two-dimensional boundary-area. The boundary condition is calculated with

$$\sqrt{\frac{\mu_0\mu_\mathrm{r}}{\varepsilon_0\varepsilon_\mathrm{r} - j\sigma/\omega}}\boldsymbol{n} \times \boldsymbol{H} + \boldsymbol{E} - (\boldsymbol{n} \cdot \boldsymbol{E})\boldsymbol{n} = \boldsymbol{0}, \tag{58}$$

Initial temperature throughout the model is set at room temperature at 20°C. The boundaries of the rock sample are set to be thermally insulated, as the heat exchanged between the rock sample and the air domain is assumed to be negligible in the short irradiation duration. Thus, the boundary condition can be presented as:

$$-\boldsymbol{n} \cdot \boldsymbol{q} = 0. \tag{59}$$

Thus, the thermal flux in the direction of the bottom surface normal is set to 0.

A fixed boundary condition is set for the rock sample bottom to limit its movement in downwards direction. The sample is allowed to thermally expand in all three other directions. The fixed bottom boundary condition is set by setting displacements of the bottom surface to 0 as

$$\boldsymbol{u} = 0, \tag{60}$$

where $\boldsymbol{u}$ is the displacement.

5.2 Simulated rock sample numerical model settings

In this section, all necessary steps to create the simulated rock sample numerical model are presented.

5.2.1 Numerical modelling parameters

Aim of the first model is to assess how different material and radiation parameter affect the induced temperature changes and stresses in a rock sample. The aim is to isolate the effect of parameters on the induced stresses and determine which varied parameters have the greatest influence on microwave assisted comminution. For this reason, simplified

geometries and material parameters are used. The rock sample geometry consists of a cubical host mineral that contains mineral intrusions. The host mineral side length is 0.01 m if not stated otherwise. The geometry of the intrusions is varied between spheres and the five the platonic solids. These include the tetrahedron, cube, octahedron, dodecahedron, and the icosahedron. The sample is enclosed within a simplified microwave geometry. The microwave geometry dimensions are presented in **Table 3**. The model geometry is presented in **Figure 4**.

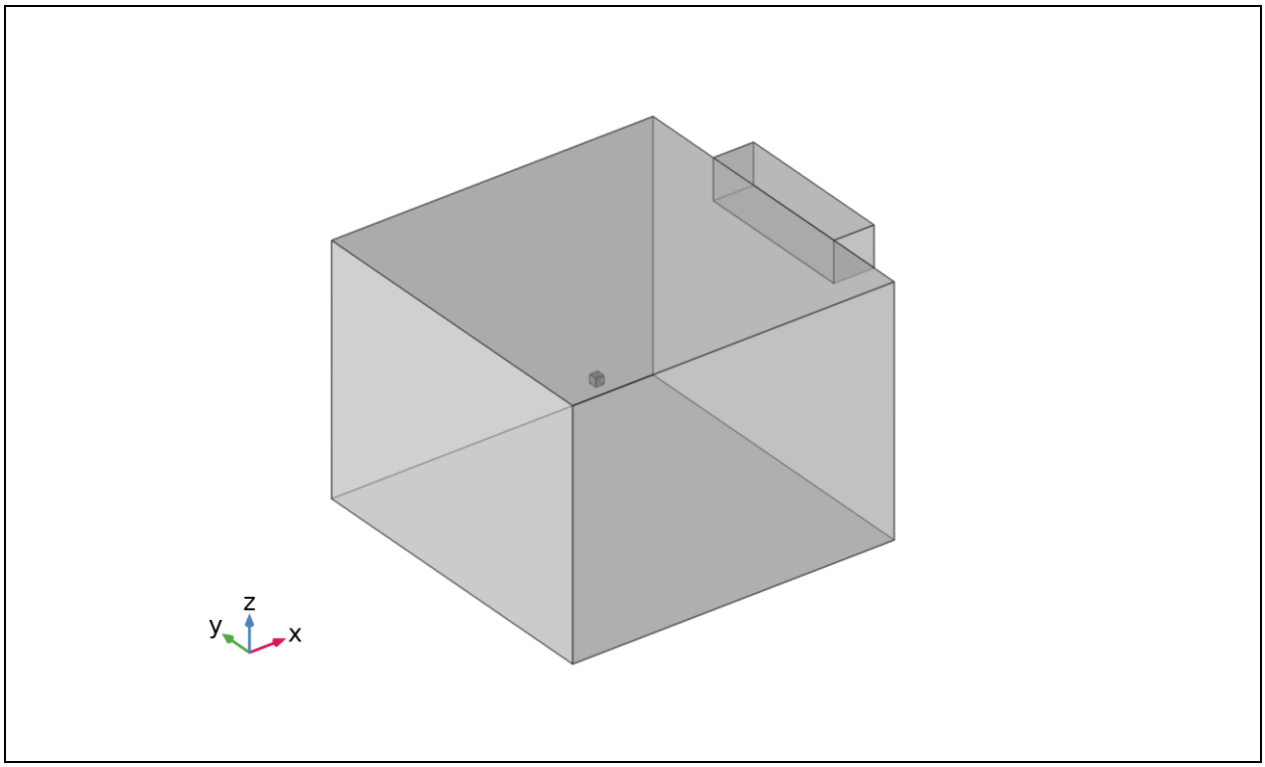

Figure 4: Model geometry of the simulated rock sample. The large rectangle represents the microwave area, the smaller rectangle the waveguide and the smallest cube the rock sample

Table 3: Model geometry of the microwave oven in mm

Component	x-dimension	y-dimension	z-dimension
Rectangular waveguide	50	200	50
Copper casing	400	400	300
Air domain	400	400	300

In order to maintain a sensible number of variable combinations, only one variable is changed at a time. Thus, initial values for all parameters are required. For the microwave frequency, the commonly used 2.45 GHz is used together with a power of 1 kW. A host mineral with a low relative permittivity is used to simulate a mineral absorbing heat transferred by microwaves weakly. For the internal minerals, a mineral with a high relative permittivity is used. The ratio between the internal and external mineral is chosen to be 0.1 with a total of 8 symmetrically placed internal minerals. In other words, the total volume of all 8 internal minerals account for 10 % of the volume of the host mineral. Finally, cubical shape is set for the internal minerals. A summary of the model parameters of the initial step are presented in **Table 4.**

Table 4: Initial model parameters of the base case.

Parameter	Value
Frequency [GHz]	2.45
Power [kW]	1
Host mineral	non-absorbing
Internal mineral	absorbing
Ratio between internal and host mineral	0.1
Number of internal minerals	8
Shape of the internal minerals	cubical

Material parameters were assigned for each geometrical domain in the finalized model geometry. These parameters include all necessary material properties required for the full numerical model including electrical, thermal, and mechanical properties of the rock.

Electric properties are required for all materials for which the EM-wave equation, **Equation (53)**, is solved. In addition to the minerals within the rock sample, the EM-wave equation is solved for the air and copper domains. Furthermore, values for relative permeability for the aforementioned materials are required.

Material properties for the copper casing and the air domain are imported directly from COMSOL material libraries. The values are presented in **Table 5**.

Table 5: Material properties of the copper casing and the air domain

Material	ϵ_r	μ_r	$\sigma\ [S/m]$
Air	1	1	0
Copper	1	1	$6 \cdot 10^7$

Material properties for the high-permittivity mineral are based on pyrite, whereas the values for the low permittivity mineral are based on quartz. However, definitive values are not used and thus approximate values for both minerals are used. The approximate values for pyrite are based on values presented in **Table 7** and **Table 8**. Next, the material properties of quartz used in the first numerical model are discussed.

Marland, Merchant and Rawson (2001) present dielectric permittivity values for minerals associated with coals. In their study, they determined dielectric permittivities for quartz in various frequencies. The real part of dielectric permittivity for quartz mineral in 2.216 GHz is 1.85, while the imaginary part is 0.0493. The values were determined in 60°C. The value was determined for quartz with a density of 2650 kg/m^3. In this study approximate values of 2 for ϵ_r' and 0.5 for ϵ_r'' are used.

According to Rochette, Jackson and Aubourg (1992) quartz acts as a diamagnetic mineral, meaning that the relative permeability of it is less than 1. They present a value of $-14.5 \cdot 10^{-6}$ for the magnetic susceptibility of quartz. However, as the value deviates only very little from 0, the effect on the numerical model is deemed insignificant. The permeabilities can be calculated from the more common magnetic susceptibilities with the relation

$$\mu_r = \chi + 1, \tag{61}$$

where χ is the magnetic susceptibility of the mineral. Thus, a value of 1 for the relative permeability of quartz is used.

According to Robertson (1988) the thermal conductivity of quartz decreases between 300 K and 300 k from approximately 10 $\frac{\mathrm{W}}{\mathrm{m}*\mathrm{K}}$ to 3 $\frac{\mathrm{W}}{\mathrm{m}*\mathrm{K}}$. For the first model a value of 5 $\frac{\mathrm{W}}{\mathrm{m}*\mathrm{K}}$ is used. They also present a value of 4.98 $10^{-5}/^{o}C$ for the coefficient of volumetric expansion for quartz with a density of 2648 kg/m3. Thus, a value of 5 $[10^{-5}/^{o}C]$ is used for the coefficient of quartz in the first model. Finally, the specific heat capacity of quartz at 20°C is 740 $[J/kgK]$.

Furthermore, elastic properties for both minerals are required in order to assess the induced stresses in the rock sample. In **Section 3.5** it was discussed how Young's modulus and Poisson's ratio can be used to determine the stress-strain relationship of a material. However, multiple ways, or sets of parameters, called elastic modulus, to determine the relations exist. These moduli can be easily converted to each other with simple calculations. In the case of COMSOL, the elastic properties can be added in multiple configurations and the software automatically calculates the desired values. The relationship between Young's modulus, Poisson's ratio and the shear modulus G can be calculated with

$$G = \frac{E}{2(1+\boldsymbol{\nu})}, \tag{62}$$

while the relationship between Young's modulus, Poisson's ratio and the bulk modulus K can be calculated with

$$K = \frac{E}{3(1-2\boldsymbol{\nu})}. \tag{63}$$

Whitaker *et al.* (2010) determined the elastic properties of Pyrite mineral. They present a pressure dependant K and G for the mineral in 0 – 9.5 GPa pressure range. K of pyrite varies between 151 GPa and 193 GPa within the range, whereas G varies between 118 GPa and 139 GPa. As the first numerical model utilizes simplified mineral properties, an average value of 172 GPa for K and 128 GPa for G is used. Y and $\boldsymbol{\nu}$ are calculated from the averages using **Equation (62)** and **Equation (63)**.

Wang *et al.* (2015) determined the temperature dependent elastic properties of quartz in the pressure range between 100 kPa and 10 GPa. The values for K increased from 38 GPa to 90 GPa, while the values for G increased from 44 GPa to 49 GPa. Values for Y and $\boldsymbol{\nu}$ are calculated again from the averages of K and G using **Equation (62)** and **Equation (63)**. All material properties used in the first model are presented in **Table 6**.

Table 6: Material parameters of the first numerical model

Parameter	Pyrite	Quartz
$\epsilon_r{}'$	8	2
$\epsilon_r{}''$	1	0.05
μ_r	-	1
$\mu_r{}'$	0.9	-
$\mu_r{}''$	0.2	-
k [W/(m · K)]	20	5
c_p [J/(kg · K)]	500	740
α_V [$10^{-5}/^oC$]	3.4	5
ρ [kg/m^3]	5000	2700
$\boldsymbol{Y}$ [GPa]	308	113
$\boldsymbol{v}$	0.2	0.2

As the aim of the first model is to evaluate the effect of isolated changes in input parameters and model geometry, a coarser mesh is used in the modelling to decrease the computational intensity of the model and thus speed up the simulation. The mesh consists of freely formed tetrahedral elements. They are chosen, as the model geometry varies in some steps of the model. The density of the mesh is controlled via giving the mesh either a pre-defined density through COMSOL or with a minimum and maximum element size.

As the stresses and temperatures are solely assessed in the rock sample area, a much denser mesh is used there. The minimum element size is $5 \cdot 10^{-6}$ m and the maximum element size $9 \cdot 10^{-4}$ m in the rock sample, if not stated otherwise in a step. The surrounding air domain is meshed with a predefined element size of *fine* in COMSOL. The elements have a minimum size of $4.5 \cdot 10^{-3}$ m and a maximum size of 0.036 m. The complete mesh consists of 62893 elements. The minimum quality is 0.211 and the average quality 0.66. The element quality ranges from 0 to 1 with 0 being the worst element quality and 1 the best. The mesh on top of the internal minerals is presented in **Figure 5**.

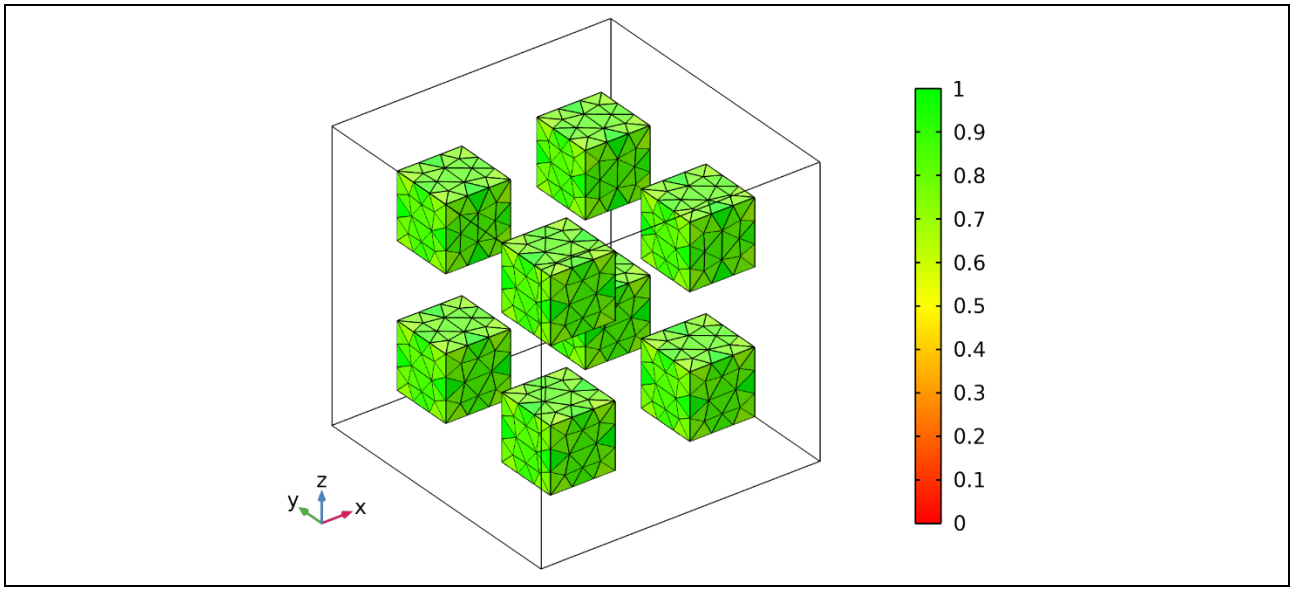

Figure 5: An overview of the element size and quality on the internal minerals. 1 represents perfect element quality while 0 worst element quality

Finally, the solver settings are presented. As the numerical model is of a time-dependent nature, a time-dependent solver is used. The solver method is Backward Differentiation Formula with a relative tolerance of 0.01 and a tolerance factor of 0.1. The step size is determined as a range from 0 to 120 s with a 1 s step. parallel sparse direct solver is used as the linear system solver. The same settings are used for both **Section 5.2** and **Section 5.3**.

5.2.2 Steps of the first numerical model

Steps of the first numerical model consist of varying the parameters listed in **Table 4** in the following way:

1) determining whether larger stresses are induced by placing the sample within an EM-wave maximum or minimum
2) altering input power of the microwave radiation
3) altering minerals in the rock sample
4) altering the rate of the internal and external mineral in the rock sample
5) altering the mineral grain size
6) altering the shape of the internal minerals
7) using a 30 cm x 30 cm x 30 cm sample
to assess the effect on induced stresses

An overview of all steps is also presented in **Figure 6.**

Step 1: Situating the rock sample in an EM-field local min and max

Run	Sample located within EM maximum
1	True
2	False

Step 2: Changing input power of microwave radiation

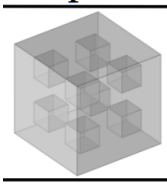

Run	Input power
1	0.1 kW
2	1 kW
3	5 kW
4	10 kW

Step 3: Varying the mineral composition of the rock sample

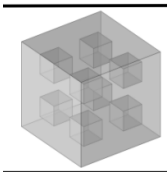

Run	Host mineral	Internal mineral
1	Quartz	Pyrite
2	Pyrite	Quartz
3	Pyrite	Pyrite
4	Quartz	Quartz

Step 4: Varying the ratio between the internal and host mineral

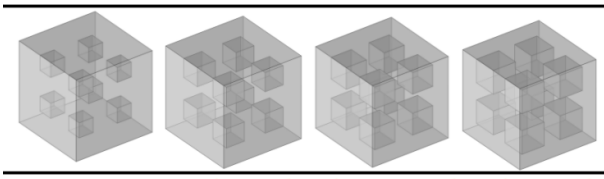

Run	Ratio between internal and host mineral
1	0.05
2	0.10
3	0.15
4	0.20

Step 5: Varying the internal mineral size

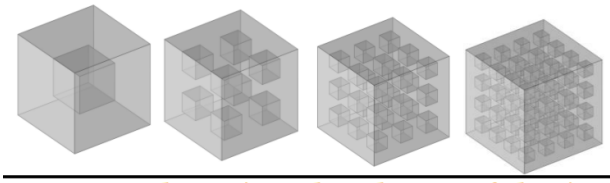

Run	Number of internal minerals
1	1^3
2	2^3
3	3^3
4	4^3

Step 6: Changing the shape of the internal minerals

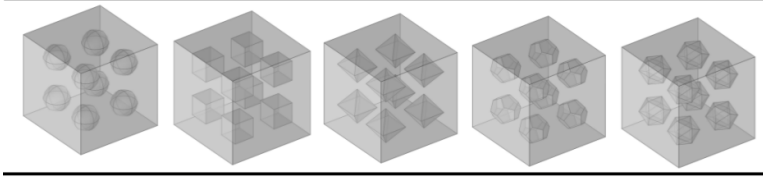

Run	Shape of internal minerals
1	Sphere
2	Cube
3	Dodecahedron
4	Icosahedron

Step 7: Using a larger rock sample

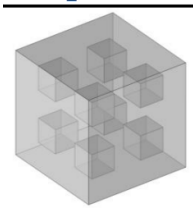

Run	Length of host mineral edge
1	0.1 m

Figure 6: Configurations of each step of the numerical modelling of the simulated sample. The various mineral geometries are presented on the left side. In the base case, the rock sample side length is 0.01 m, the host mineral is quartz and internal mineral pyrite. The fraction between pyrite and quartz is 0.1 and the internal minerals cubical. The input power is 1 kW. The changed parameters of each step are presented on the right-hand-side.

Step 1: Situating the rock sample in an EM-field local minimum and maximum
The EM-wave pattern inside of the microwave oven is determined by the shape of the wave guide and the frequency of the microwave radiation. As the geometry is constant throughout the model, only the frequency has an effect on the wave pattern. Thus, in the first step it is necessary to determine whether placing the sample within a minimum or a maximum of the EM-wave induces larger stresses in the sample. The result is used to place the sample in the most optimal place for all varied frequencies in the following steps of the model.

When the sample is displaced -0.02 m in the x-direction and +0.02 m in the z-direction from the centre of the microwave domain, it lies within a local EM wave maximum. Alternatively, displacing the sample by X and Z from the centre sets the sample within a local EM-wave minimum. Displacement, where the rock sample is within a local EM-wave maximum and in the XZ plane is visualized in **Figure 7.**

As the results in **Section 6.1** indicate, higher stresses are obtained, when the rock sample is situated within an EM-wave local maximum. Thus, in all following steps the rock sample is set at -0.02 m, +0.02 m (x- and y-directions) displacement. However, in the next step, where the effect of different microwave frequencies is assessed, the sample displacements are set separately for each different frequency.

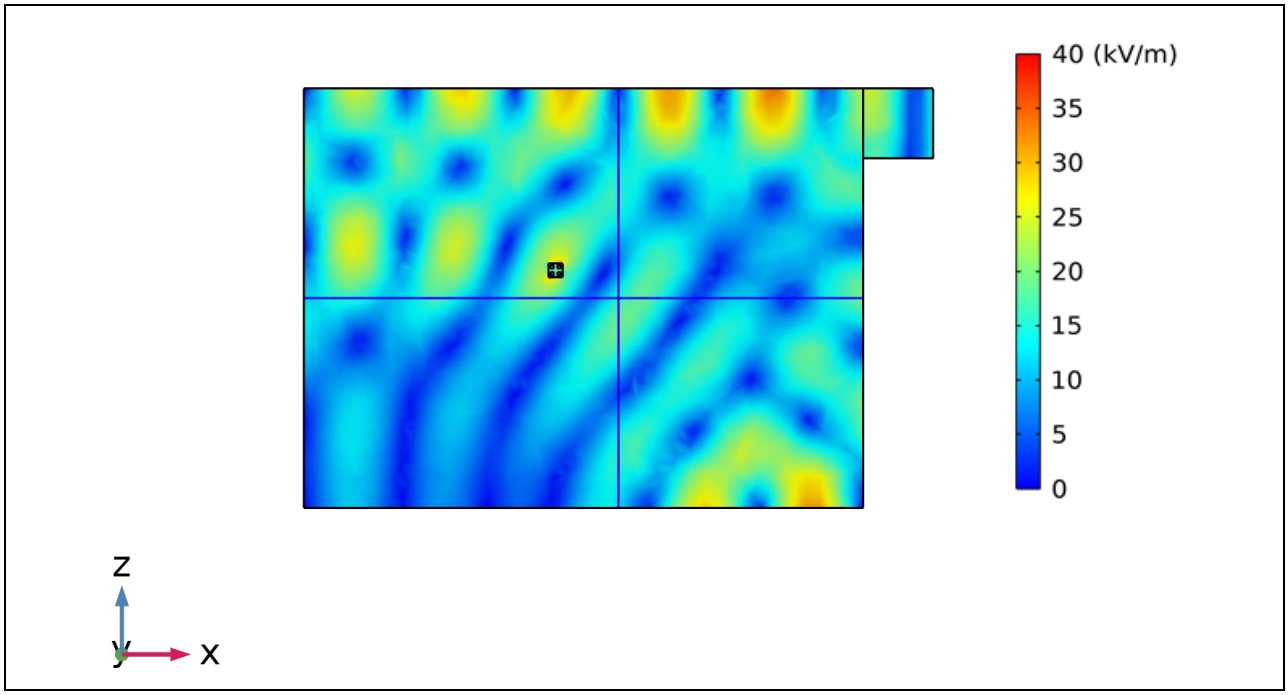

Figure 7: The EM-field, where the rock sample is situated within a local maximum.

STEP 2: Changing input power of microwave radiation

Effect of different input microwave powers on the induced stresses are assessed in the third step. The aim is to study whether irradiating the sample with low power radiation for a long duration or with high power radiation for a short period induces larger stresses. 100 W is chosen as the low microwave input power. The power is increased to 1 kW, 5 kW, 10 kW powers. 10 kW is set as a conservative maximum power, as many industrial cavity microwave

ovens operate at that power range (i.e. (Richardson Electronics, no date), (Fricke und Mallah Microwave Technology GmbH, 2020)).

In this step, the mesh element size was lowered slightly. As the higher power of the microwave radiation induce far larger temperatures and stresses on the sample, the element quality was deemed inadequate. Thus, in this step the minimum element size is $4.5 \cdot 10^{-6}$ m and the maximum size $8.5 \cdot 10^{-4}$ m. This resulted in a mesh consisting of 70688 elements with a minimum quality of 0.2053 and an average quality of 0.6587.

STEP 3: Varying the mineral composition of the rock sample

Varying the mineral composition of the rock sample is assessed in this step. In this step, the internal and host minerals are changed in the following way: 1) The host mineral is quartz, and the internal mineral is pyrite, 2) The host mineral is pyrite while the internal mineral is quartz, 3) Both minerals are pyrite and 4) Both minerals are quartz. The first run is identical to the initial case. The aim is to assess, whether rocks consisting of various minerals induce more or less stresses than homogenous rocks. The effect of having high permittivity minerals enclosed within low permittivity minerals and vice versa is also studied.

STEP 4: Varying the ratio between the internal and external mineral

In the Step 4, the ratio between the internal mineral and the host mineral is varied. The chosen ratios are 0.05, 0.1, 0.15 and 0.2 volume of internal mineral per volume of the external mineral. In practice, this either decreases or increases the size of the internal minerals. The volume of a single internal mineral changes thus from X1, X2, X3 to X4.

As the rock sample geometry is varied throughout this step, the mesh size changes accordingly. The minimum and maximum element size is held at the same thresholds as in step 1. When the ratio is set to 0.05, the total element count is 63558. With a ratio of 0,15 the element count is 62197 and with the ratio of 0.2 the mesh consists of 64118 elements.

STEP 5: Varying the internal mineral size

Step 5 is very similar to the fourth step, but instead of changing the mineral size by varying the relation between internal mineral and the host mineral, the size of an individual internal mineral is changed. This is achieved so that the total fraction keeps constant between the runs. This method simulates various grain sizes so that the internal minerals ratio to the external mineral is kept constant. In the initial step 2^3 individual internal minerals are used. In step 6, this number is varied between 1^3, 2^3, $3^3$and 4^3. The aim of the step is to understand, whether higher stresses are induced on coarsely or finely grained minerals.

In this step the geometry of the sample is once again varied when the number of internal minerals is changed. The element counts for 1^3, 3^3 and 3^3 are 62842, 65214 and 65523 respectively.

STEP 6: Changing the shape of the internal minerals

In this step the shapes of the internal minerals are changed mainly to understand how altering the geometry angles affect the induced stresses. For Step 6, four different platonic solids, namely cubical, octahedral, dodecahedral, and icosahedral solids are used. Additionally, a spherical shape is also used. Platonic solids are used, as all angles in the shape are regular. The volumes or all shapes in Step 6 are defined so that the ratio between internal minerals and external minerals stays identical to the initial step.

When spherical internal minerals are used, the mesh element count is 65209. For the octahedral minerals, the count is 63175, for dodecahedral it is 64295 and finally for the icosahedral the element count is 62278. The minimum and maximum element sizes are again same as in step 1.

STEP 7: Using a larger rock sample

In the eight step, the rock sample size is changed from 0.01 m x 0.01 m x 0.01 m to 0.1 m x 0.1 m x 0.1 m. The ratio between the internal and external mineral is also held at 0.1. This results in larger sample and mineral sizes altogether. The aim of this step is to study, whether higher stresses are induced with smaller or larger shapes. Otherwise, the geometry is identical to STEP 1.

As the rock sample size is increased significantly in this step, the element count of the mesh has to be adjusted in order to keep the computational time reasonable. Thus, the minimum element size is increased to $1 \cdot 10^{-4}$ m and the maximum to 0.015 m. This results in a mesh consisting of 25628 domain elements.

5.3 Digitizing and numerically modelling microwave heat transfer on a Pyhäsalmi mine ore sample

In this section it is evaluated, how irradiating a rock sample with a realistic geometry and more in-depth material properties affects its stress state. For this model, a sample of Pyhäjärvi mine from Finland is digitized. The digitized sample is in the place of the symmetrical rock sample of **Section 5.2**. The rock sample is again enclosed in a microwave domain, where it is irradiated with microwave radiation. The thermomechanical response of the rock sample is also modelled. The steps of digitizing the rock sample are discussed in the next section. This is followed by presenting the material parameters of the rock sample.

5.3.1 Rock sample digitization

The chosen Pyhäsalmi rock sample was selected from Aalto University collections. Images of the sample were taken through a polarizing microscope with a phone camera. A 2.5 times magnification objective was used on the microscope. The images were then digitized in order to use the sample data in the numerical modelling process.

Aim of the digitization was to turn the sample image into a vector geometry. The vector geometry is used later to define the model geometry for the numerical model. The workflow in the image digitization was as follows: 1) the image was edited to bring forth edges between different minerals 2) the edges were detected with an edge detection algorithm 3) the detected edges were fine tuned to close regions and reduce noise 4) the edges were turned from raster images to vector images. The individual steps are discussed next in detail.

An image of a rock sample chosen in **Section 4** was first edited with a graphics editor to increase contrast between light and dark areas. Additionally, the number of colours was decreased to lessen the amount of noise in the image. This helped to simplify one mineral consisting of different hues of one colour to one universal colour. With these steps, the image should ideally have one colour representing each mineral present in the sample. Finally, the image was cropped to resemble a rectangular area. The initial image and the edited version of the rock sample images are presented in **Figure 8**.

In the next step, the image was opened in MATLAB where it was converted into grayscale. The inbuilt edge detection tools of MATLAB require grayscale images for simple edge detection. Next, the edge detection method *Canny* was used. *Canny* is beneficial as the aim was to generate areas enclosing each individual mineral which the algorithm is well suited for.

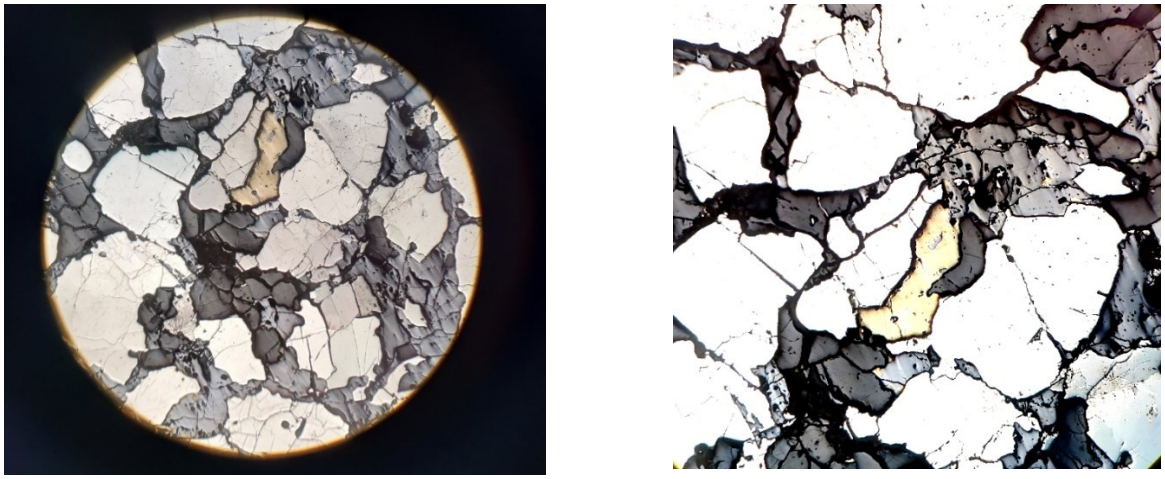

Figure 8: On the left, the initial image of the rock sample. On the right, colour corrected and cropped image of the sample.

After the edges of minerals were detected in MATLAB, the image was exported and fine-tuned in a graphics editor to enclose any edges that were left open in the algorithm. Additionally, any leftover noise and small mineral fragment areas were removed with a graphics editor. In this state, the image consisted of two colours, a black background and white mineral edges. The image in this state is presented in **Figure 9**.

Figure 9: The hand adjusted and detected edges prior to converting them to vectors. The detected edges of the rock sample mineral boundaries are pictured with white colour.

As the image at this state consisted of only two colours, the edges could be detected easily within the graphics editor and converted into vector graphics. The vector graphics were exported as a dfx-file, compatible with the COMSOL geometry building tool. A final touch to the dfx-vectors was performed within the COMSOL geometry module. In this step it is ensured that all vectors form closed minerals and no tiny mineral fragments are present. The final digitized mineral boundary samples are presented in **Figure 10**.

Figure 10: The final rock sample surface geometry created from the Pyhäsalmi rock sample created from vectorized mineral boundaries.

5.3.2 Model geometry and meshing

Identically to **Section 5.2**, a simplified microwave geometry consisting of two rectangular blocks representing the microwave interior and the waveguide are used. The details of the microwave geometry are presented in **Table 3**. Additionally, a glass-block is placed within the microwave geometry. The glass block is used as a way to place the thin rock sample on a support so that a roller boundary condition can be used on the bottom of the rock sample. The roller boundary condition allows movement in x- and y-directions but prohibits it in the z-direction. This simulates the rock sample being laid on top of an immovable object.
The glass block is excluded from heat transfer simulations and thus only the mechanical load from the thermally expanding rock sample affects the block. The block also influences the EM-field in the microwave oven.

The digitized geometry created in **Section 5.3.1** is imported to the model geometry builder and the vectors indicating mineral boundaries are used to separate different 2D domains in the sample area. The dimensions of the rock sample are based on the image width of the microscope. In the image, the sample is approximately 0.01 m wide. Thus, the x- and y-dimensions of the rock sample are set as 0.01 m. In the z-direction, a thickness of 5 mm is assumed based on the sizes of the individual minerals. The finalized model geometry is presented in **Figure 11**.

In order to maximize the temperatures and stresses within the rock sample, the sample is once again displaced so that it is approximately within a local EM-maximum. Thus, the sample is displaced in X in x-direction, and Z in z-direction from the centre of the microwave oven. The rock sample within the EM-field in the XZ-plane is presented in **Figure 11**.

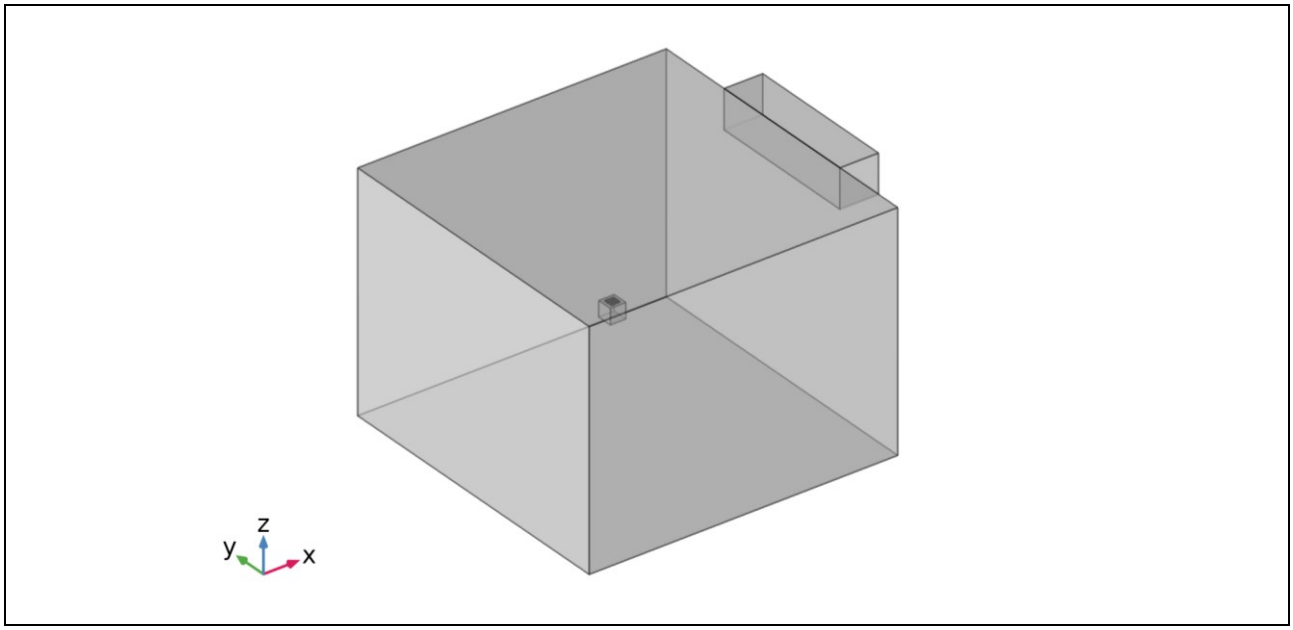

Figure 11: The full model geometry. The large rectangle represents the microwave oven while the smaller rectangle represents the waveguide. The glass cube is situated in the centre on top of which the thin rock sample is laying. The x- and y-side length of the microwave is 0.4 m while the z-side is 0.3 m long.

The rock sample surface is meshed with a free triangular mesh. The formed triangular network is swept throughout the rock sample and divided into three layers. This decreases the amount of mesh element within the rock sample. A free tetrahedral mesh is used throughout rest of the model.

As discussed in **Section 5.2.1**, the element size of the mesh plays a great role in both increasing the accuracy of the calculations but also increasing the complexity of the solver. For this reason, a balance between computational accuracy and complexity is sought for in this Section. Thus, the minimum element size is set to 10^{-4} m in the triangular mesh. With these settings the final mesh consists of 263749 elements with a minimum quality of 0.056 and an average quality of 0.62. The mesh of the rock sample surface is presented in **Figure 12**.

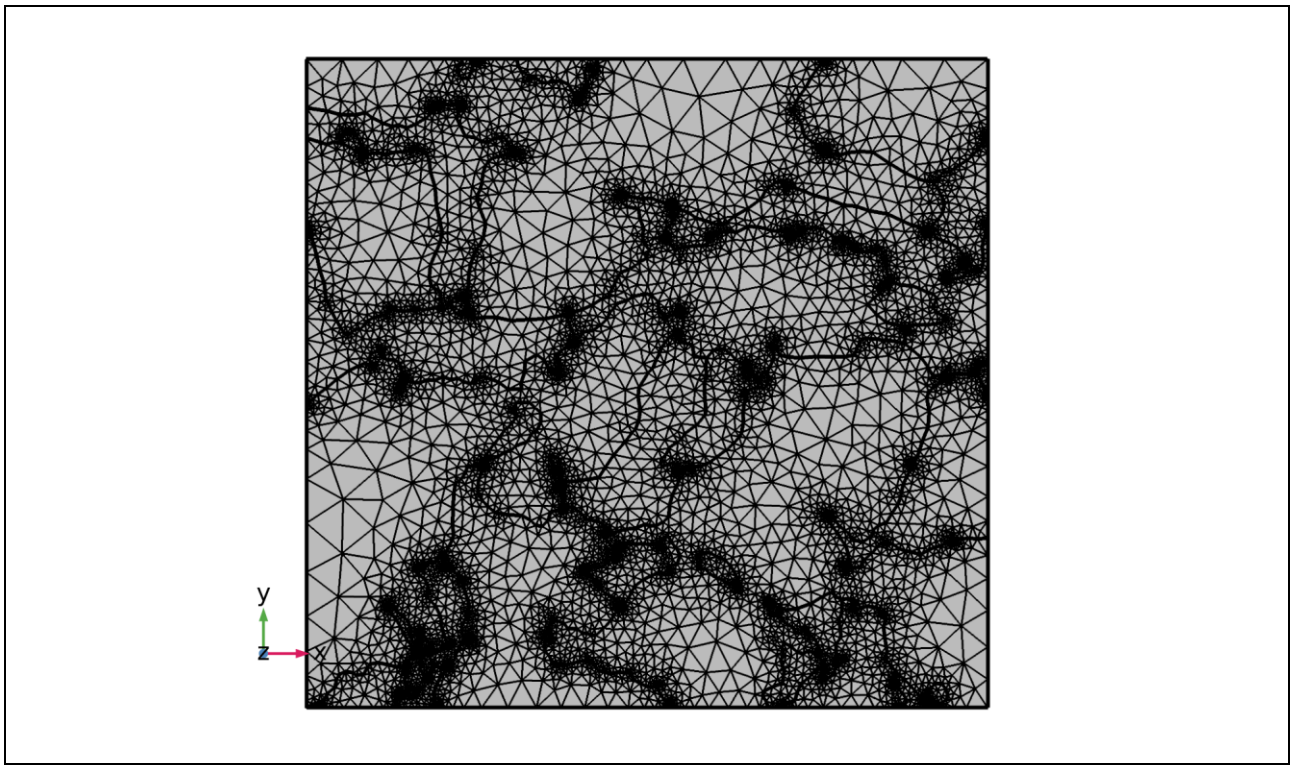

Figure 12: The finalized free triangular mesh on the top surface of the rock sample. The side length is 0.01 m.

5.3.3 Material parameters

Material properties for the air and copper domains are presented earlier in **Table 5**. Same values are used here in this Section. In **Section 5.2**, approximate values for pyrite were used. However, in this Section, more accurate values are used. Thus, material parameters specific for pyrite and additionally all other Pyhäsalmi mine rock sample minerals are discussed and presented next.

Dielectric properties of all minerals in this Section are based on the values in **Section 4**. As various values exist for most of the minerals, a selection on a single value was done. As the both the real and imaginary dielectric constants of pyrrhotite vary significantly and the values are drastically higher than on most other minerals, conservative values of 20 for ϵ_r' and

0.6 for ϵ_r" were selected. The selected values are presented in **Table 7**. Next the permeabilities of the minerals are discussed.

Peng *et al.* (2014) determined temperature dependant imaginary and real permeability of pyrite. In 100 – 400 K range both the real and imaginary part of the permeability are varying very little and are approximately 0.9 and 0.2 respectively for 2.45 GHz frequency radiation. Furthermore, Zhandov, (2018) presents a value of 1 for pyrite and chalcopyrite, and a value of 2.5 for pyrrhotite.

Kingman, Rowson and Sahyoun (2003) present magnetic susceptibility values for chalcopyrite in 0 – 800 °C range. The susceptibility of the mineral rises linearly in 0 to 350 °C range from 0.12 to 0.2. From 350 °C to 500 °C, the susceptibility rises rapidly from 0.2 to 0.5 in which it stays until 650 °C. The relative permeability of chalcopyrite is calculated from these values with **Equation (64)** and presented in **Table 7**.

Rochette, Jackson and Aubourg (1992) present a magnetic susceptibility value for pyrrhotite as $50 - 300 * 10^{-3}$. The relative permeability is calculated from the value using **Equation (61)** and presented in **Table 7**. Dahlin and Rule, (1993) present a magnetic susceptibility of $3.81 \cdot 10^{-9}$ for sphalerite. The calculated relative permeability is presented in **Table 7**.

Table 7: electromagnetic properties of minerals and other materials used in the study

Material	ϵ_r'	ϵ_r"	μ_r	μ_r'	μ_r''
Chalcopyrite	4.75	0.26	1.12 – 1.5		
Pyrite	7.5	1.1	1	0.9	0.2
Pyrrhotite	20.0	6.0	1.175		
Sphalerite	9.66	0.007	1		

In addition to the electromagnetic properties, thermal properties of the minerals are required for the numerical modelling. These parameters include the thermal conductivity and the heat capacity at a constant pressure. Wyzga *et al.* (2017) determined a temperature dependant thermal conductivity for three different samples of Mexican natural chalcopyrite. They present an empirical fit for the thermal conductivity as

$$-1.94 + 2865\, \boldsymbol{T}^{-1}. \tag{64}$$

The formula is applicable in the thermal range required in this study. Their results are in line with experimental results of Lefèvre *et al.* (2016), who reported similar values for the thermal conductivity of chalcopyrite. For this study a value of 7.68 $\frac{W}{m \cdot K}$, calculated at 373.15 K is used.

Clauser and Huenges (1995) present values for thermal conductivities for rocks and minerals. They present thermal conductivity values for pyrite and pyrrhotite in 35 °C temperatures. Furthermore, Horai, (1971) presents a thermal conductivity of 12.71 $\frac{W}{m \cdot K}$ at 0°C for Sphalerite. The values are presented in **Table 8**.

Waples and Waples (2004) determined specific heat capacities for multiple minerals. The measurements were undertaken in various temperatures, but for chalcopyrite, pyrite,

pyrrhotite and sphalerite the specific heat capacity was determined at 20°C. The values for these minerals at 20°C are presented in **Table 8**.

Table 8: Thermal properties of minerals

Material	$c_p\ [J/(kgK)]$	$k[W/(m \cdot K)]$
Chalcopyrite	534	7.68
Pyrite	510	23.15
Pyrrhotite	594	3.53
Sphalerite	450	12.71

Finally, the mechanical properties of the material are once again only required for the rock sample minerals. These parameters include the Young's modulus, Poisson's ratio, density, and coefficient of thermal expansion.

Robertson, (1988) present values for volumetric thermal expansion coefficients of various minerals. Minerals applicable for this study are sphalerite and pyrite The values apply for a temperature range between 20°C and 400°C and are thus suitable for this study. They also present densities for the minerals. Volumetric coefficients of thermal expansion and the densities for minerals used in this study are presented in **Table 9**.

Very little research is conducted on thermal expansion parameters of chalcopyrite mineral. However, Khaledalidusti, Mishra and Barnoush (2019) calculated thermal expansion behaviour of chalcopyrite. Their results are presented in **Figure 13**.

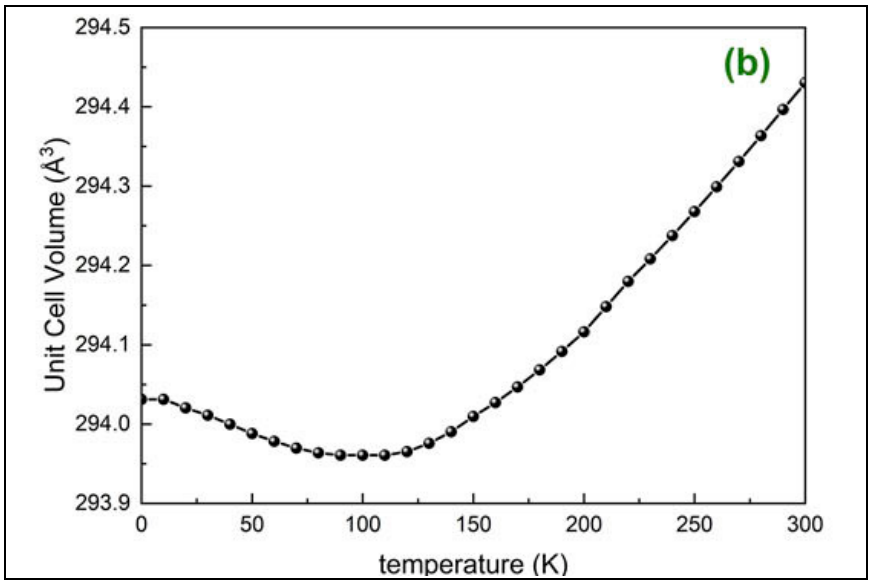

Figure 13: Thermal expansion of Chalcopyrite by (Khaledalidusti, Mishra and Barnoush, 2019).

As seen from **Figure 13**, chalcopyrite has a peculiar negative coefficient of thermal expansion in the 0 – 100 K range. However, from 100 – 300 k, the coefficient is positive and thus can be easily calculated with:

$$\alpha_V = \frac{1}{V}\left(\frac{dV}{dT}\right). \tag{65}$$

Thus, in the 150 – 300 k range, the volumetric coefficient of thermal expansion of chalcopyrite is 0.98 $[10^{-5}/^{o}C]$.
Tenailleau et al. (2005) determined coefficients of thermal expansion of pyrrhotite samples in various temperatures. The average value for pyrrhotite was 12.6 $[10^{-5}/K]$ which is presented in **Table 9**.

Table 9. Volumetric coefficient of thermal expansion and the density of the rock sample minerals.

Material	$\alpha_V[10^{-5}/K]$	$\rho[kg/m^3]$
Chalcopyrite	0.98	4190
Pyrite	3.40	5016
Pyrrhotite	12.6	4610
Sphalerite	2.37	4089

Similar values of Y and $\boldsymbol{v}$ for pyrite as discussed in **Section 5.2.1** are used for the modelling of the digitized sample and are again presented in **Table 10**. Values for the other minerals have been studied very little. Therefore, values presented here should do not necessary represent the minerals accurately in same temperatures and pressures. However, the focus of this numerical model is to crudely analyse, how the stress-state develops when the sample is heated, the values are deemed sufficient.

Khaledalidusti, Mishra and Barnoush (2019) determined the bulk and shear modulus of chalcopyrite in 300 K experimentally. Young's modulus and Poisson's ratio were calculated from values they present with **Equation (62)** and **Equation(63)** and are presented in **Table 10.**

Goldman, Rossman and Dollase (1997) cited in Ahrens (1995) present elastic properties for Sphalerite at room temperature. Young's modulus and Poisson's ratio calculated based on their values using **Equation (62)** and **Equation (63)** are presented in **Table 10.**

Kübler (1985) determined the Young's modulus of single-crystal pyrrhotite samples in various temperatures. They observed that Y decreases when temperature is increased. At 473.15 K, Y has a value of 67 GPa. Finally, Ji *et al.* (2018) determined a value of 0.2 for pyrrhotite. Values for pyrrhotite are presented in **Table 10**.

Table 10: Young's modulus and Poisson's ratio of the rock sample minerals.

Material	Y [GPa]	$\boldsymbol{v}$
Chalcopyrite	202	0.2
Pyrite	308	0.2
Pyrrhotite	67	0.2
Sphalerite	83	0.3

6 Results

In this section, results both for both the simulated and the digitized model are presented.

6.1 Results of the numerical model with the simulated rock sample

As the main interest in the first model is on differences between thermally induced stresses, a unified location for determining the stresses was set. As the internal minerals have a larger relative permittivity, the internal minerals absorb more heat transferred by microwave radiation. This causes larger temperatures within the internal minerals. This, combined with the difference between the volumetric coefficients of thermal expansion cause the largest stresses to be located on the boundary between the internal minerals and the host mineral. This is also corresponding with the results of previous studies discussed in **Section 2**. For this reason, the stresses are evaluated and compared on the bottom edge of one of the internal minerals on the upper side of the symmetry axis of the rock sample. The selected edge is visualized in **Figure 14**.

An observation edge was used to plot the data, as observing solely the maximum stress within one internal mineral gives too much influence on very high stresses in elements consisting of sharp corners. With a line, a more general stress state can be compared, as an average value can be calculated. As the aim is not on studying any absolute values, but focus on general trends in the result, this approach is deemed sufficient.

Stresses higher than those appearing on the selected border are possible within other internal sample edges, but as the main focus of the assessment is stress differences between input parameters, the selected border suffices. Furthermore, stresses on the border are plotted at the final timestep (120 s). Next, the results of each individual step of the first model are presented.

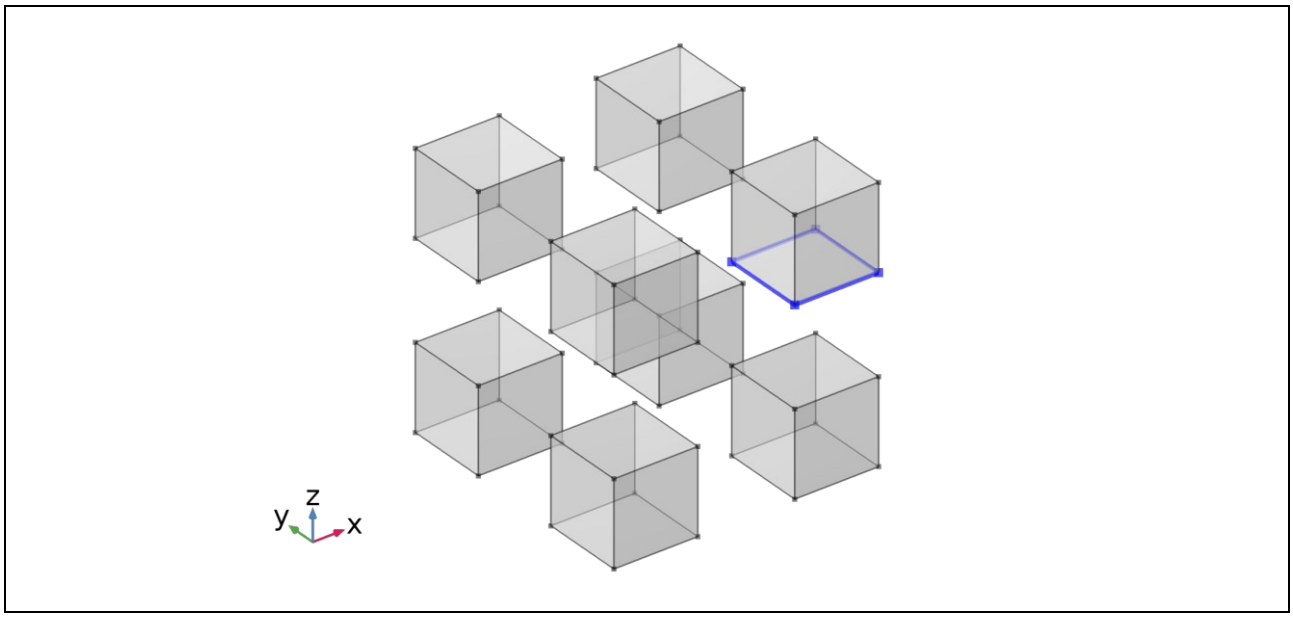

Figure 14: The border, visualized with blue colour on which the stress and temperature data is evaluated in **Table 11**, **Table 12**, **Table 13**, **Table 14**, and **Table 15**.

STEP 1: Situating the rock sample in an EM-field local minimum and maximum

In the first step it was assessed whether situating the rock sample within an EM-wave maximum or minimum yields in larger induced stresses. The rock sample within a local EM-maximum is presented in **Figure 7**. The minimum maximum and average stresses and temperatures on the observation edge when the sample is places within a local EM wave maximum are presented in **Table 11**. The stresses and temperatures in a local minimum are presented in **Table 12**.

Table 11: The minimum, maximum and average von-Mises stress and temperature on one of the top internal mineral edges, when the rock sample is within a local EM-wave maximum.

Parameter	Min	Max	Average
Stress	247	446	322
Temperature	384	384	384

Table 12: The minimum, maximum and average von-Mises stress and temperature on one of the top internal mineral edges, when the rock sample is within a local EM-wave minimum.

Parameter	Min	Max	Average
Stress	156	273	200
Temperature	350	350	350

The von-Mises stresses of Step 1 on the bottom side of the top minerals are visualized in **Figure 15**.

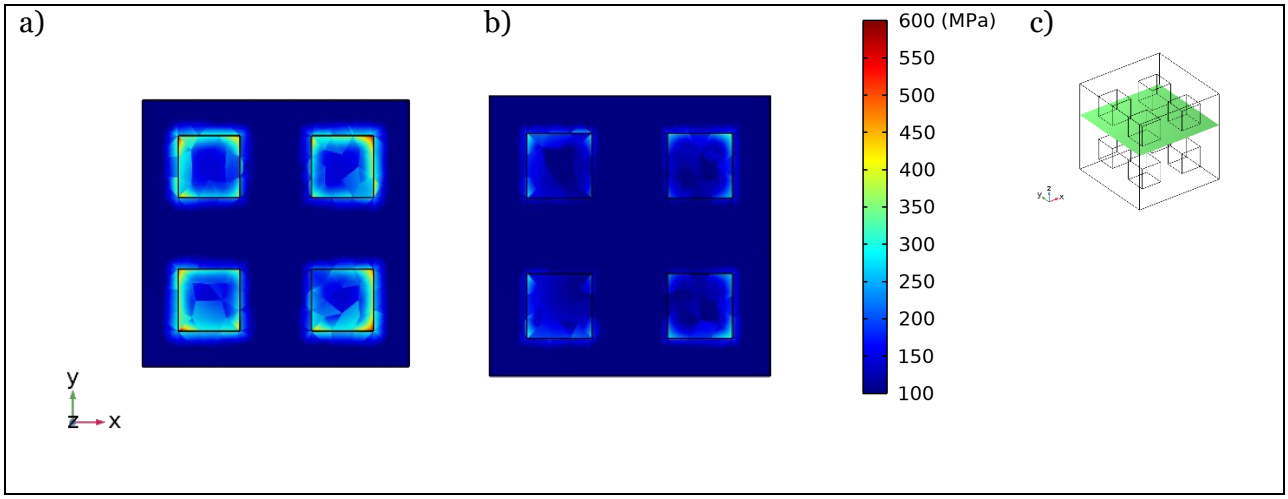

Figure 15: The maximum von-Mises stresses at a slice on the bottom of the top minerals in MPa. a) When the sample is located at an EM-wave maximum, b) When the sample is located at an EM-wave minimum, c) the cut-slice

STEP 2: Changing input power of microwave radiation

In the second step, the input power of the microwave port is varied between 0.1 kW to 10 kW. The stresses and temperatures are evaluated on the same observation edge as in Step 1. The minimum, maximum and average temperatures and von-Mises stresses for all input powers are presented in **Table 13**.

Table 13: Von-Mises stresses and temperatures on the observation edge for various microwave input powers

Input power [kW]	Parameter	Min	Max	Average
0.1	Stress	24.1	44.2	32.1
0.1	Temperature	302	302	302
1	Stress	241	442	321
1	Temperature	384	384	384
5	Stress	1200	2210	1600
5	Temperature	747	748	748
10	Stress	2410	4420	3210
10	Temperature	1202	1203	1202

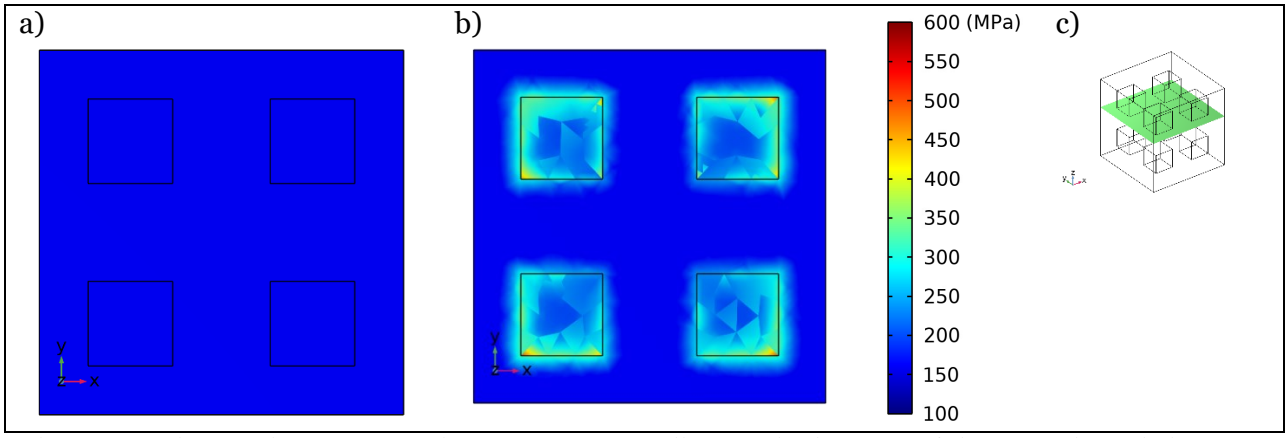

Figure 16: The maximum von-Mises stresses at a slice on the bottom of the top minerals in MPa. a) With an input power of 0.1 kW, b) with an input power of 1 kW, c) the cut-slice

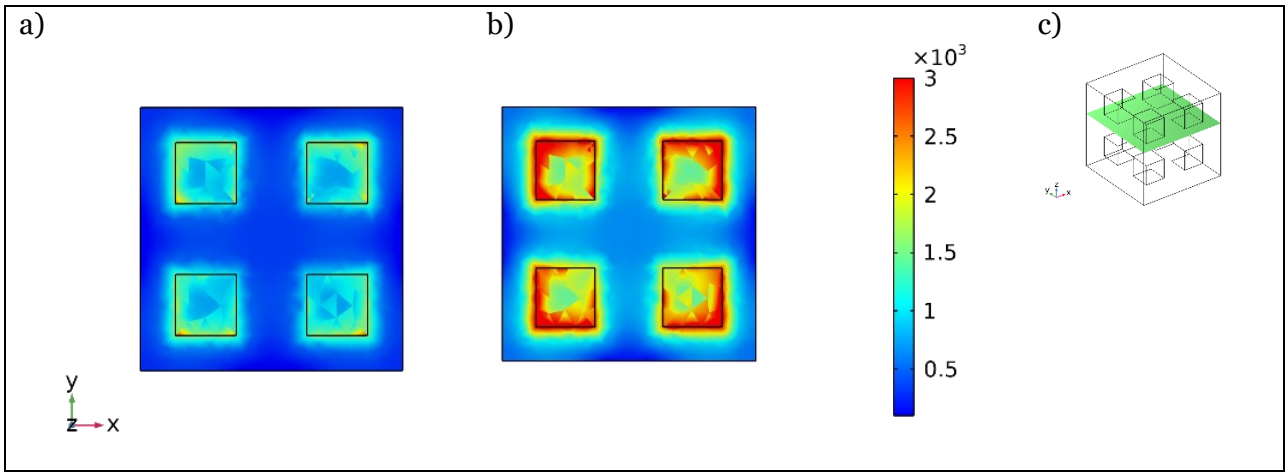

Figure 17: The maximum von-Mises stresses at a slice on the bottom of the top minerals in MPa. a) With the input power of 5 kW. b) with the input power of 10 kW, c) the cut-slice. Note the scale on the stresses.

As discussed in **Section 7**, comparing results with very high temperatures is difficult. Thus, it is better to compare, when certain temperature or stress thresholds are met with each different input power. For this reason, the stresses at the corner, where maximum stresses on an internal mineral are induced, are plotted for all time steps and internal powers in **Figure 18**. From the figure it can be seen that an induced stress of 100 MPa was reached at an irradiation time of 31 s when using the same input power, 1 KW, as in step 1. When the power is increased to 5 kW, the threshold was met at 6 s, while with the 10 kW input power the threshold was exceeded at 3 s. For all three input powers, the stress state was met around 45°C. With the lowest input power of 0.1 kW, the threshold of 100 MPa was not met during the 120 s irradiation time.

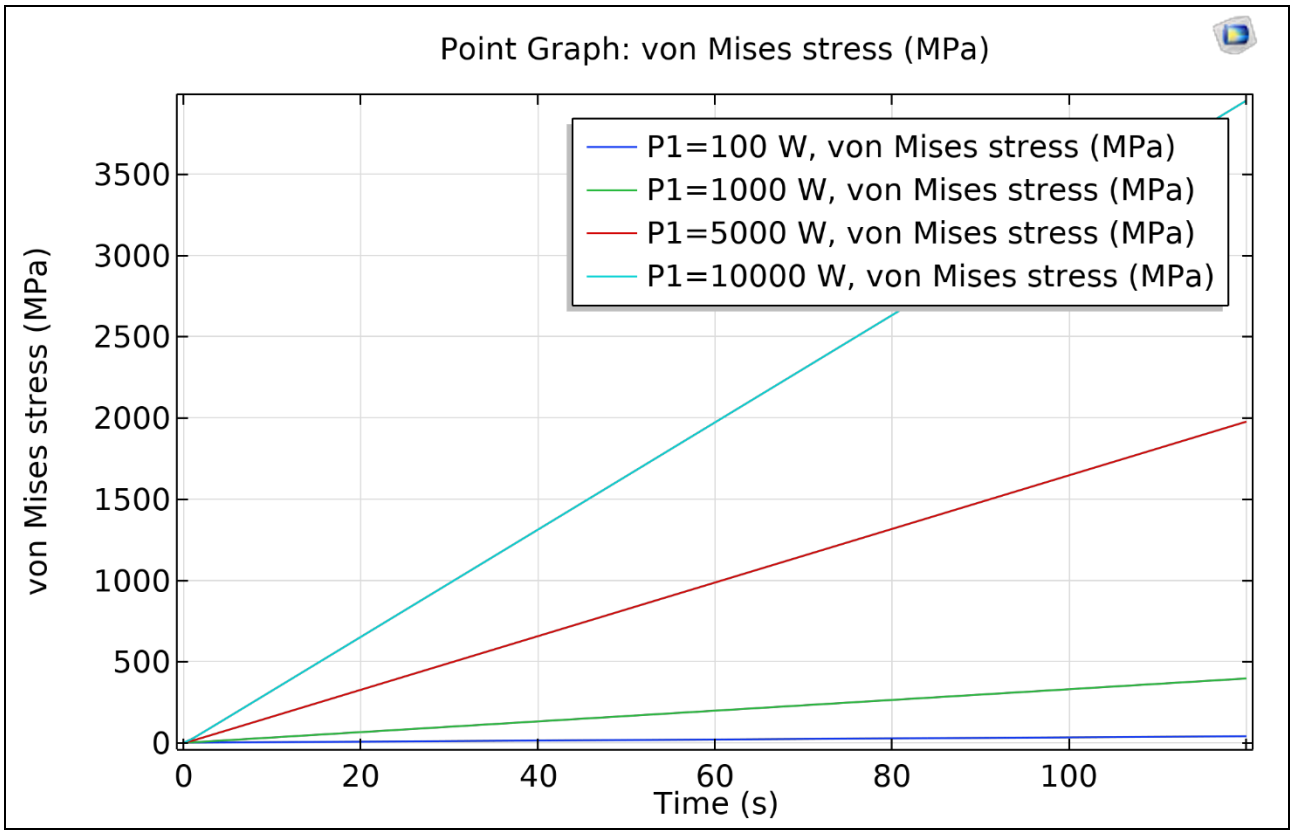

Figure 18. Von Mises stress of all input powers or 0 – 120 s

It is clearly visible from **Figure 18.** that increasing the input power of the port induces larger stresses on the sample. The very high stresses induced when using 5 kW and 10 kW input powers are explained by the very high temperature of the samples at 120 s irradiation times. In a real application the rock sample would have melted by that point, making the values not comparable at 120 s irradiation times. The slopes of the lines indicate that increasing the input power also induces larger stresses faster, than using a lower input power.

Increasing the input power also increases the magnitude of the thermal gradient in the sample. As the sample is irradiated with a constant, steady microwave radiation, the dielectric losses act as continuous heat sources. Thus, the thermal gradient within the sample stabilizes around a constant value. The thermal gradients in a corner on the observation edge for the four different microwave input powers are presented in **Figure 19**. Having higher input power results in higher thermal gradients.

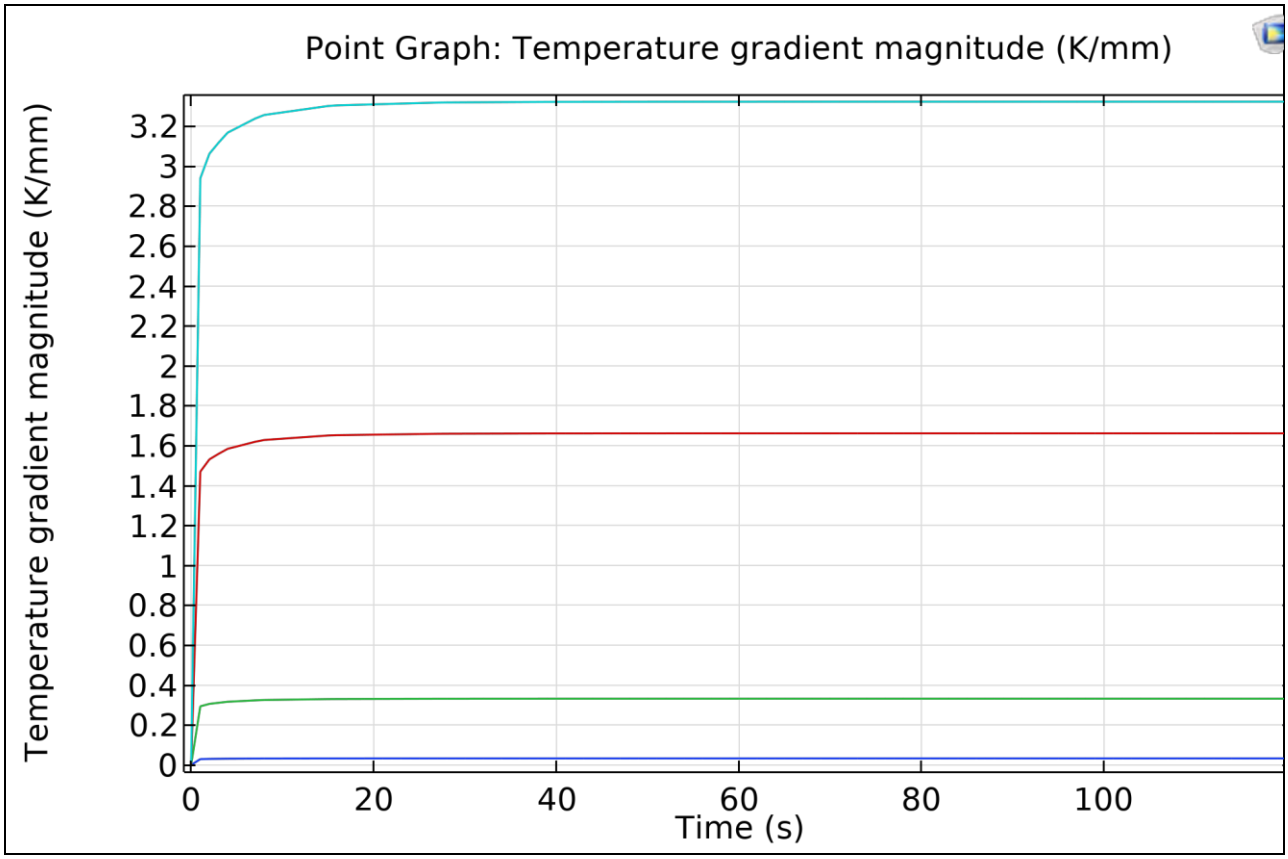

Figure 19: Magnitudes of thermal gradients of a corner of the internal mineral with 0.1 kW, 1 kW, 5 kW and 10 kW input powers.

STEP 3: Varying the mineral composition of the rock sample

In Step 3, the material properties of the external and internal mineral were varied. As the geometry of all different configurations in Step 3 are identical to the initial case, the same observation edge is used. The irradiation time and input power in this step are identical to Step 1 being 120 s and 1 kW. The minimum, maximum and average temperatures and von-Mises stresses for all material configurations are presented in **Table 14**.

Table 14: Von-Mises stresses and temperatures on the observation edge for various mineral configurations of the rock sample.

Host mineral/Internal mineral	Parameter	Min	Max	Average
Quartz/Pyrite	Stress [MPa]	247	446	322
Quartz/Pyrite	Temperature [K]	384	384	383
Pyrite/Quartz	Stress [MPa]	489	772	630
Pyrite/Quartz	Temperature [K]	550	550	550
Pyrite/Pyrite	Stress [MPa]	209	272	238
Pyrite/Pyrite	Temperature [K]	550	551	551
Quartz/Quartz	Stress [MPa]	26.7	34.8	30.4
Quartz/Quartz	Temperature [K]	355	355	355

The von-Mises stresses in all mineral configurations, on a slice adjacent to the bottom of the top minerals are presented in **Figure 20**.

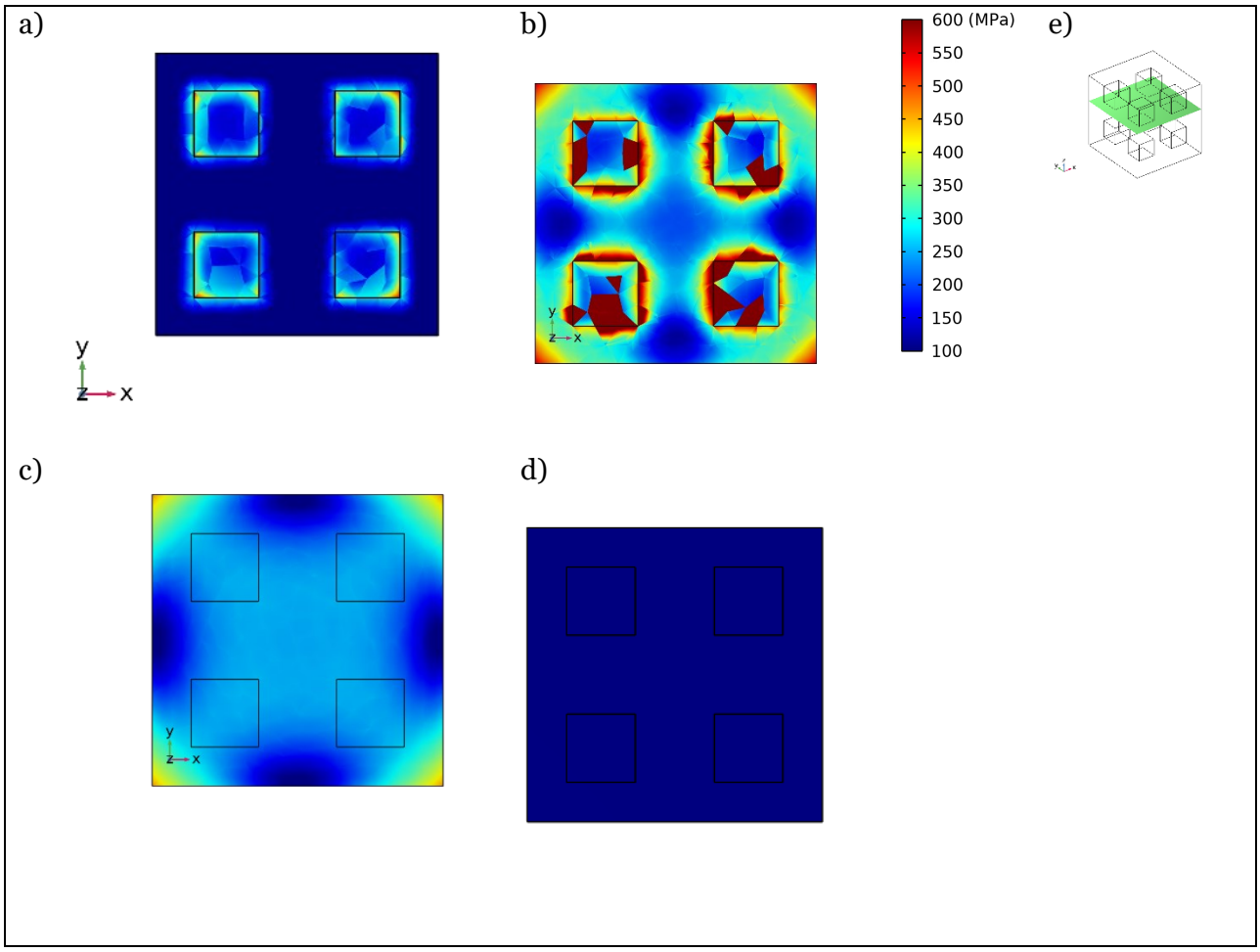

Figure 20: The maximum von-Mises stresses at a slice on the bottom of the top minerals in MPa. a) When the host mineral is quartz and the internal mineral pyrite, b) When the host mineral is pyrite and the internal mineral quartz, c) When both minerals are pyrite, d) When both minerals are quartz, e) the cut-slice

STEP 4: Varying the ratio between the internal and external mineral

In Step 4, the ratio of internal minerals to the host mineral is varied between 0.05, 0.1, 0.15 and 0.2. The stresses and temperatures are evaluated on the same observation edge as in Step 1. The minimum, maximum and average temperatures and von-Mises stresses for all ratios are presented in **Table 15**. As the length of the observation edge is altered in this step, the amount of data locations is changed between the different ratios. Thus, the average for 0.05 is calculated from 73 values, while the values for 0.1 and 0.15 are calculated from 109 values. The average for 0.2 is calculated from 145 values.

Table 15: Minimum, maximum and average von-Mises stresses and temperatures on the observation edge, when the ratio of internal mineral and external mineral is varied.

Ratio of internal mineral to the external mineral	Parameter	Min	Max	Aver-age
0.05	Stress [MPa]	198	323	254
0.05	Temperature [K]	370	370	370
0.1	Stress [MPa]	247	446	322
0.1	Temperature [K]	384	384	384
0.15	Stress [MPa]	273	489	356
0.15	Temperature [K]	398	398	398
0.2	Stress [MPa]	297	665	389
0.2	Temperature [K]	410	410	410

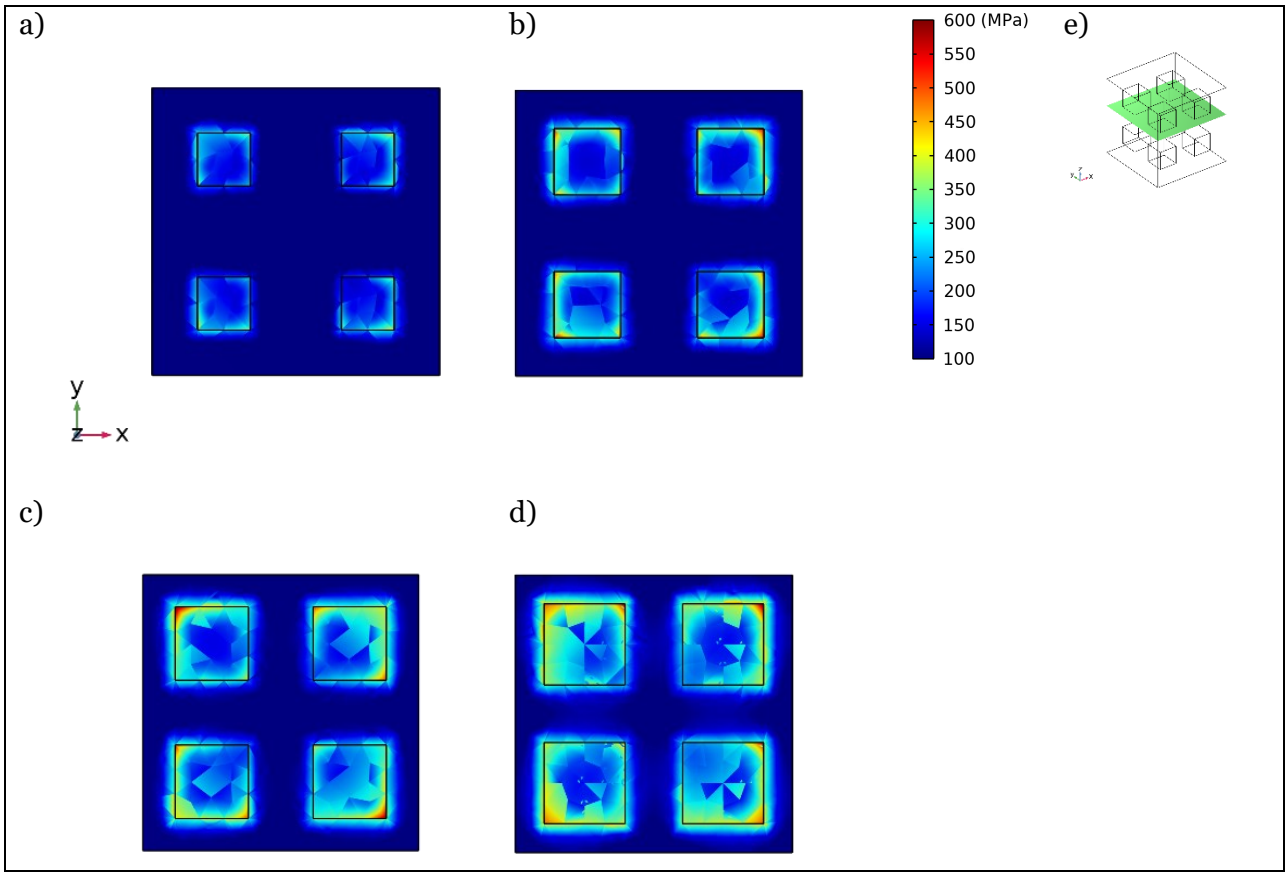

Figure 21: The von-Mises stresses at a slice on the bottom of the top minerals in MPa. a) the ratio between internal mineral to external mineral is 0.05, b) the ratio between internal mineral to external mineral is 0.10, c) the ratio between internal mineral to external mineral is 0.15, d) the ratio between internal mineral to external mineral is 0.2, e) the cut-slice

STEP 5: Varying the internal mineral size

As the number of internal minerals is varied in the fifth step, a unified observation edge is not possible. Thus, in order to study the effects of varying the grain size on the temperatures and stresses, each step is considered separately. The results when the amount of minerals is set as 2^3 are again identical to the initial model setup. The observation edges used for 1^3, 3^3

and 4^3 internal minerals are presented in **Figure 22**. The minimum, maximum and average von-Mises stresses and temperatures on the observation edges are presented in **Table 16** and the stress distribution on cutting lines within the rock sample are presented in **Figure 23**.

Table 16: Minimum, maximum and average von-Mises stresses and temperatures on the observation edges when the number of internal minerals is varied.

Number of internal minerals	Parameter	Min	Max	Average
1^3	Stress [MPa]	290	424	331
1^3	Temperature [K]	384	385	385
2^3	Stress [MPa]	247	446	322
2^3	Temperature [K]	384	384	384
3^3	Stress [MPa]	230	416	313
3^3	Temperature [K]	385	385	385
4^3	Stress [MPa]	193	439	276
4^3	Temperature [K]	386	386	386

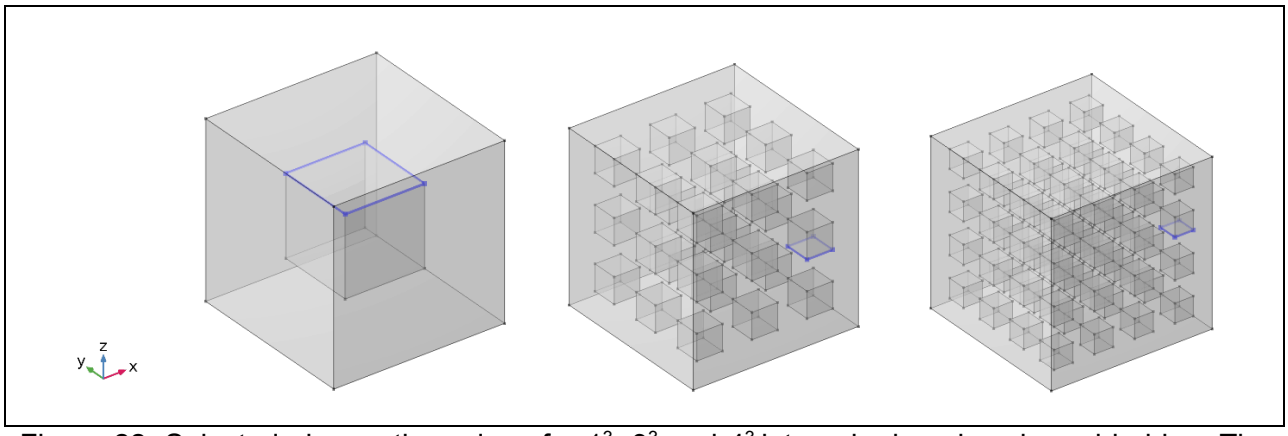

Figure 22: Selected observation edges for 1^3, 3^3 and 4^3 internal minerals coloured in blue. The data in Table 16 is evaluated on these observation edges.

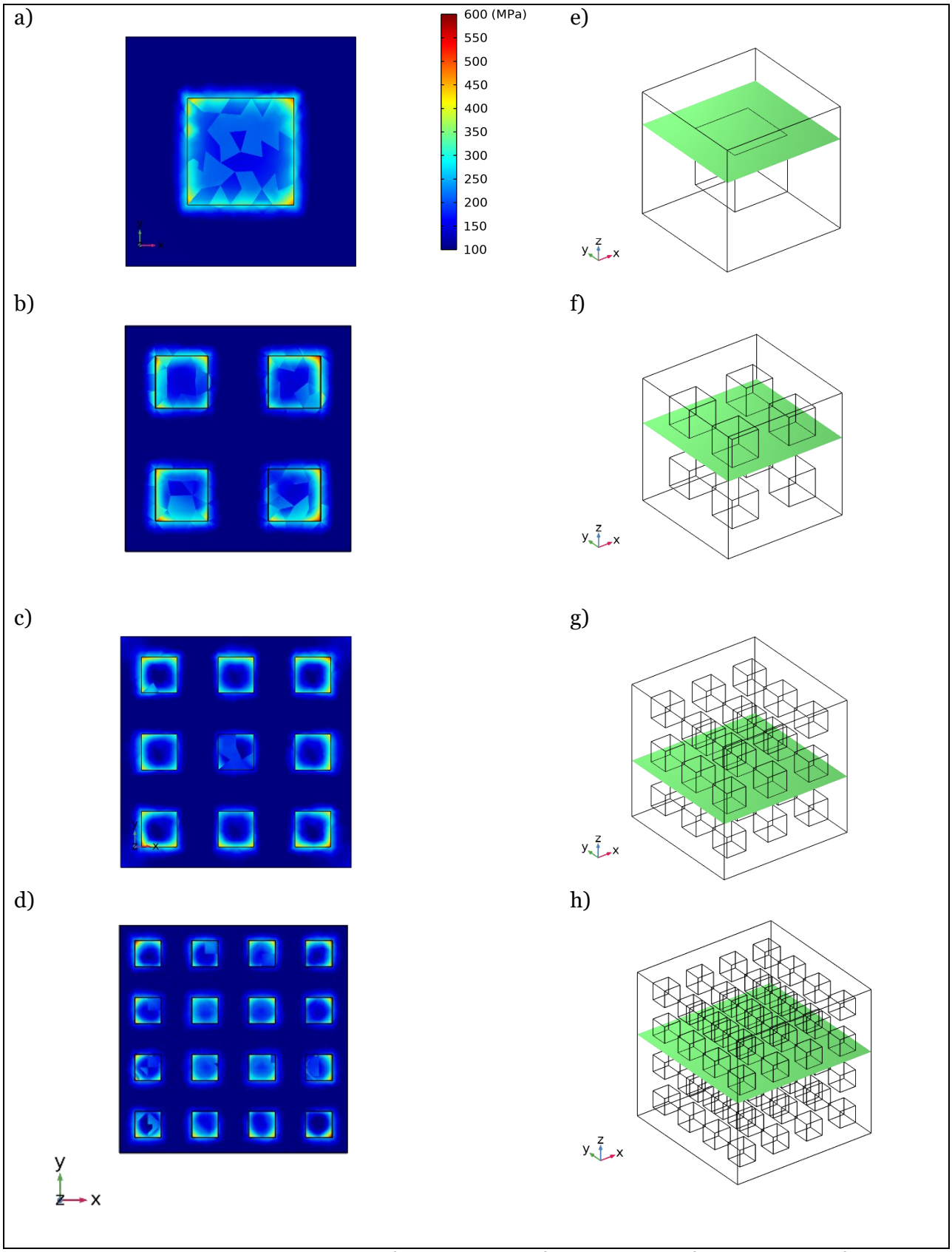

Figure 23: Von-Mises stresses on a) 1^3 minerals, b) 2^3 minerals, c) 3^3 minerals, d) 4^3 minerals with their respective cutting lines (d – h).

STEP 6: Changing the shape of the internal minerals

As the shape of the internal minerals is varied in this step, defining a unified observation edge is not possible. Thus, once again, the line is defined for each shape separately. For all shapes, the line is selected at the same mineral, as in the initial Step 1.

For the spherical mineral, the observation edge is defined at the horizontal circumference. For the octahedron, the observation edge is set on the widest horizontal edge, where the bases of both pyramids meet. The observation edges for both the dodecahedron and the icosahedron are presented in **Figure 24.** The minimum, maximum and average von-Mises stresses for the different mineral shapes are presented in **Table 17**. The stress distributions on slices of the rock sample are presented in **Figure 25**.

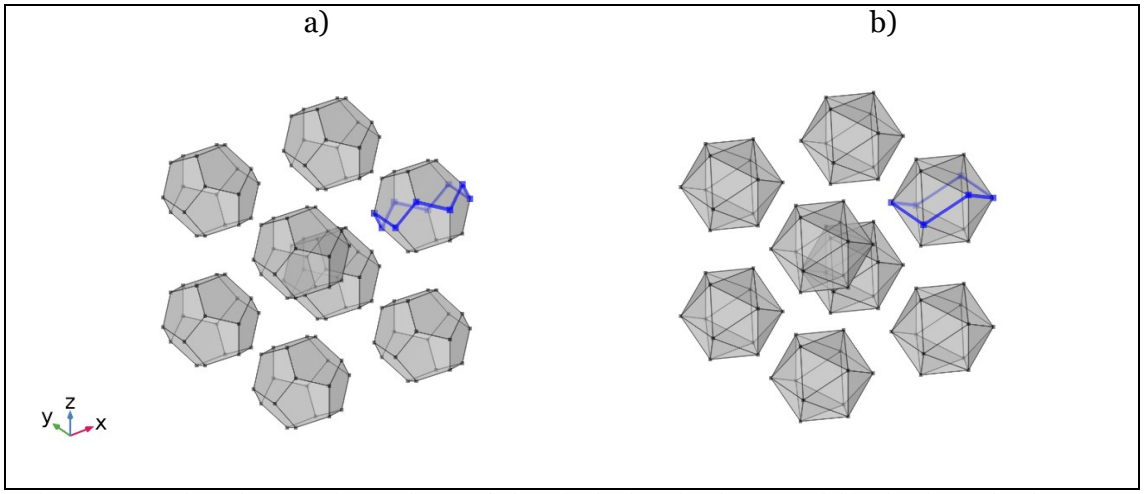

Figure 24: The observation edges of the a) dodecahedron and b) the icosahedron on which the data in Table 17 is evaluated.

Table 17: Minimum, maximum and average von-Mises stresses and temperatures for different shaped internal minerals.

Shape	Parameter	Min	Max	Average
Sphere	Stress [MPa]	152	193	169
Sphere	Temperature [K]	380	380	380
Cube	Stress [MPa]	247	446	322
Cube	Temperature [K]	384	384	384
Octahedron	Stress [MPa]	217	488	298
Octahedron	Temperature [K]	384	384	384
Dodecahedron	Stress [MPa]	185	295	223
Dodecahedron	Temperature [K]	382	382	382
Icosahedron	Stress [MPa]	163	303	212
Icosahedron	Temperature [K]	381	382	381

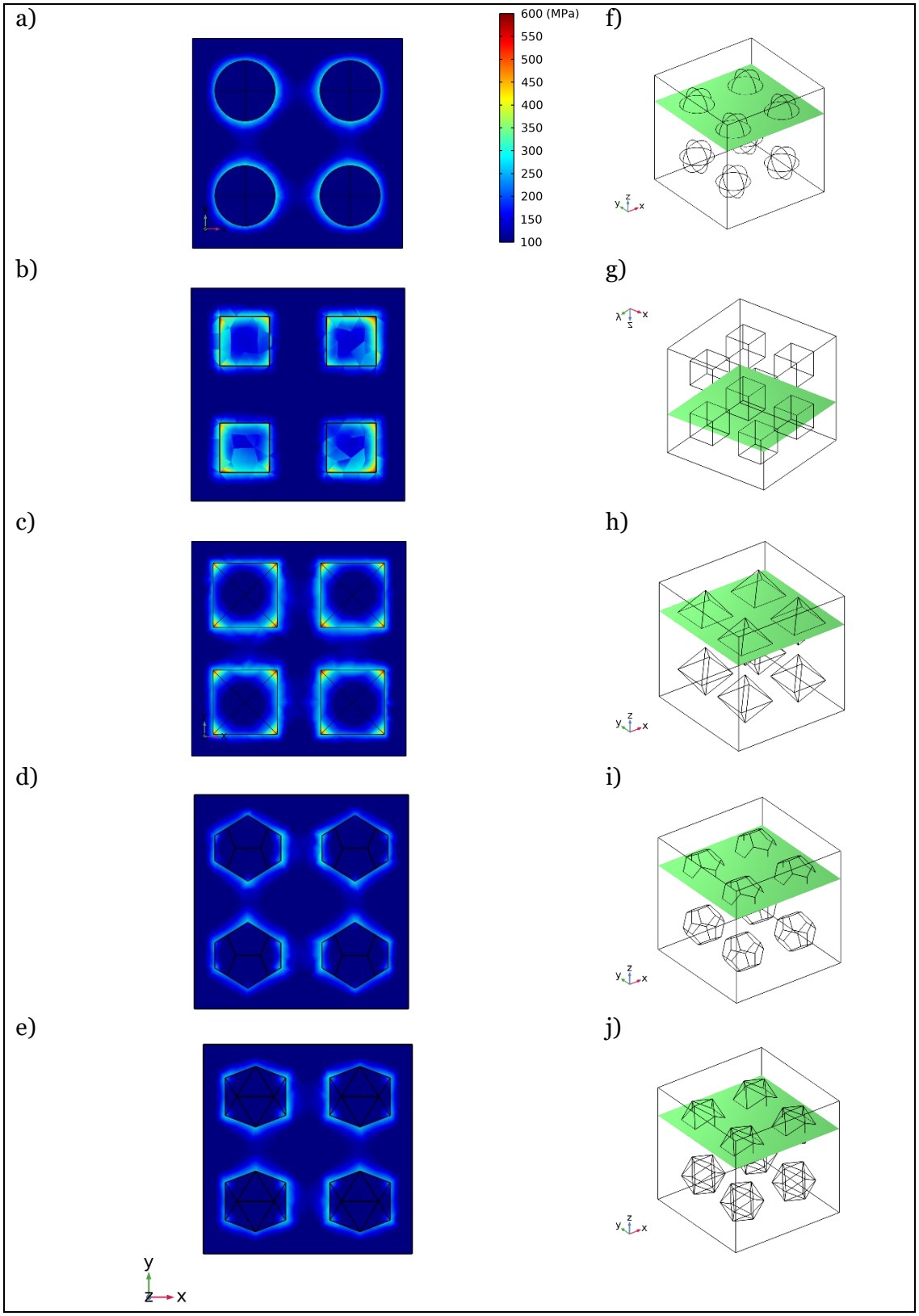

Figure 25: Von-Mises stresses on a) spherical, b) cubical, c) octahedral, d) dodecahedral and e) icosahedral internal minerals with their respective cut planes (f – j)

STEP 7: Using a larger rock sample

In the Step 7, the rock sample side length was increased tenfold. This results in a far larger rock sample and thus, the whole sample does not fit within a high-intensity part of the EM-wave. The sample is also large enough to alter the EM-field significantly. The resulting EM-field is visualized in **Figure 26**. This results in a more varied heating within the sample.

The observation edge in Step 7 was altered so that it is located within the local EM-field maximum, visible in the bottom left mineral in **Figure 26**. The observation edge is visualized in **Figure 27**. The minimum, maximum and average von-Mises stresses for the larger rock sample are presented in **Table 18**. A distribution of von-Mises stresses on a cut plane adjacent to the top side of the bottom internal minerals is visualized in **Figure 28**.

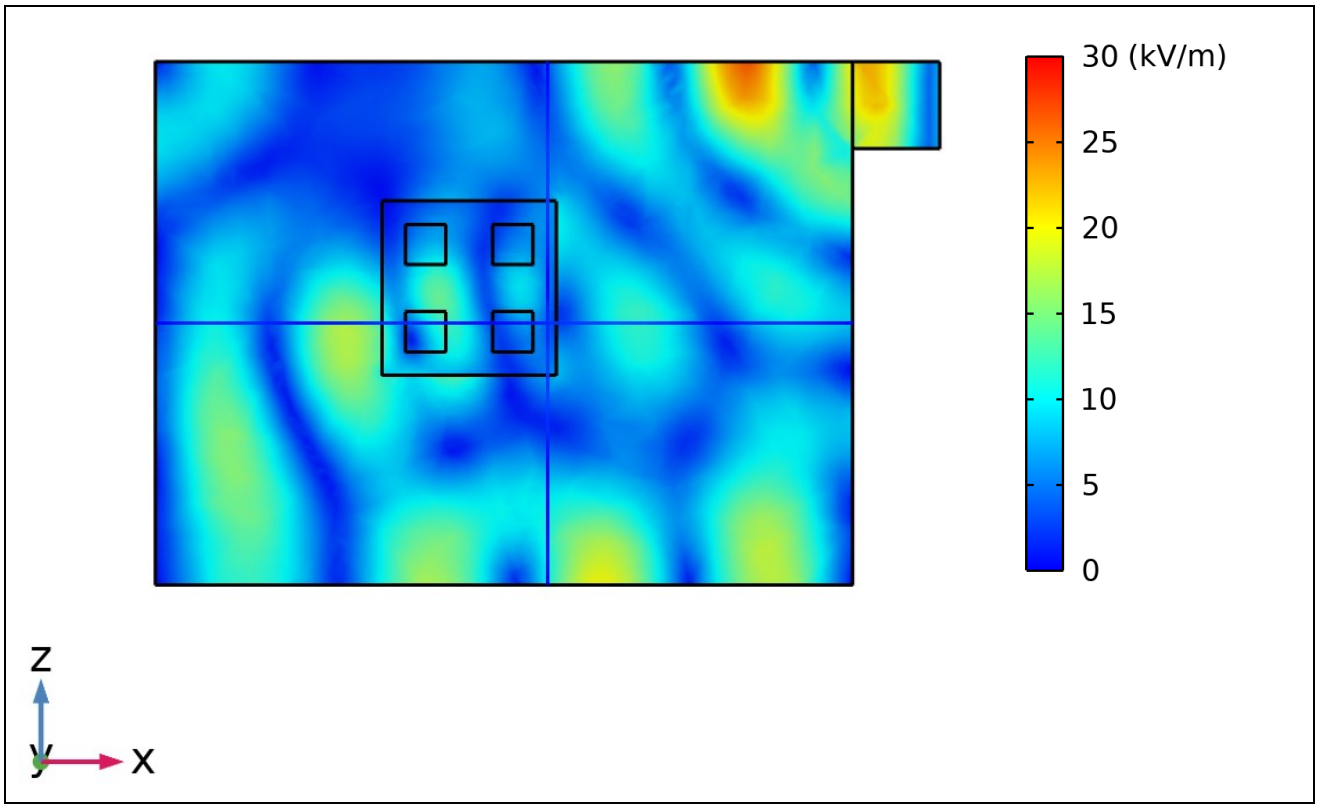

Figure 26: The larger rock sample with 0.1 cm edge widths within the EM-field

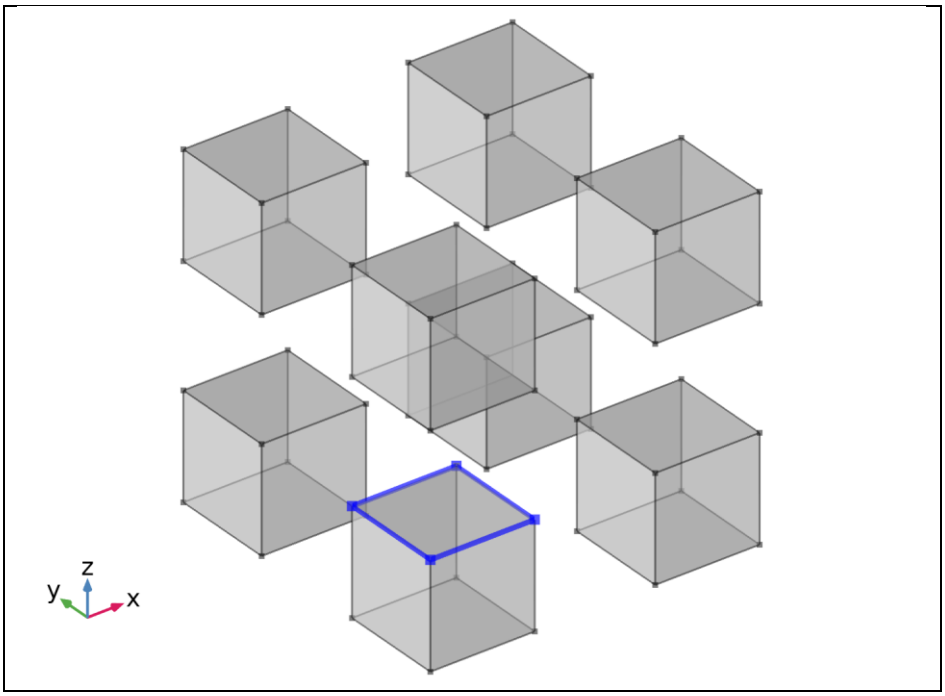

Figure 27: The observation edge used for the larger rock sample

Table 18: The minimum, maximum and average von-Mises stresses and temperatures on the observation edge, when the rock sample side length is increased tenfold

Parameter	Min	Max	Average
Stress [MPa]	79.2	199	121
Temperature [K]	350	375	365

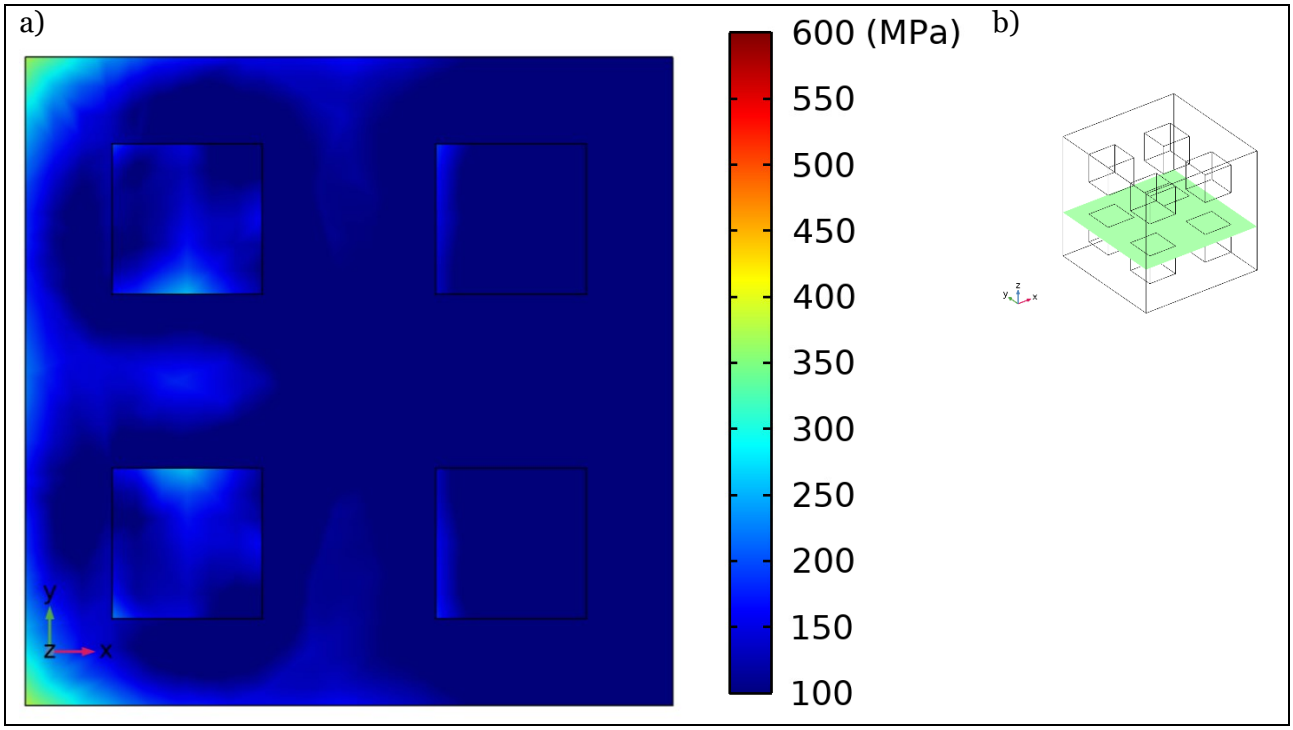

Figure 28 a) the stress distribution of the larger rock sample b) the cut plane on which the stresses are visualized

6.2 Results of the numerical model with the digitized rock sample

With the displacement of the rock sample discussed in 5.3.2, the sample is situated well within a local EM-field maximum as seen in **Figure 29**.

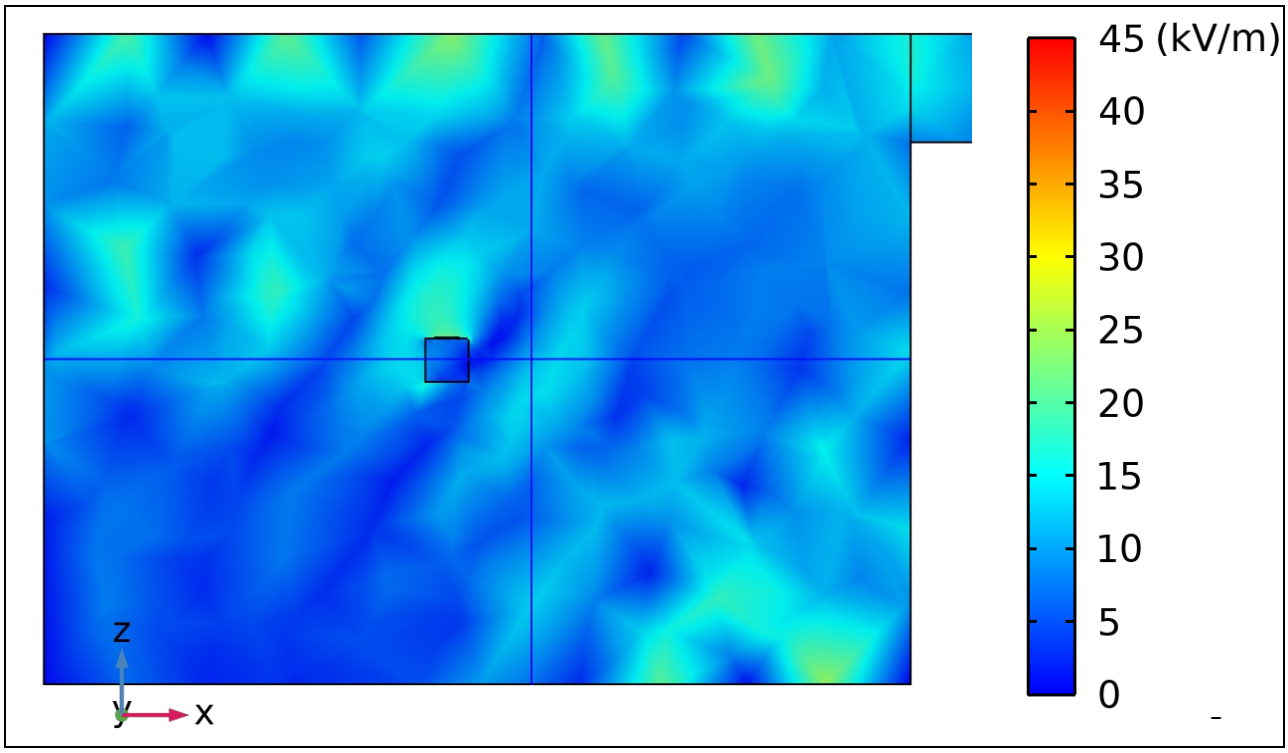

Figure 29: The digitized rock sample within the EM-field.

Due to the small size of the rock sample with a thickness only of 5 mm, the temperature and stress evaluation is conducted at 15 s time interval. Additionally, a new observation edge has to be established. The chalcopyrite mineral is situated centrally in the rock sample, and it has a diverse stress distribution on its borders. Thus, the mineral borders of chalcopyrite are selected as the observation edge. The selected border is presented in **Figure 30**.

As the sample is situated in an EM-field maximum, the heat distribution mainly results from different dielectric properties of the minerals. From the rock sample minerals, pyrrhotite has the highest imaginary part of the dielectric constant and thus it heats up the most. The temperature differences between the highest and lowest temperatures are however small. The temperature distribution on the top surface of the rock sample is presented in **Figure 31**. The minimum, average and maximum temperatures on the observation edge are presented in **Table 19.**

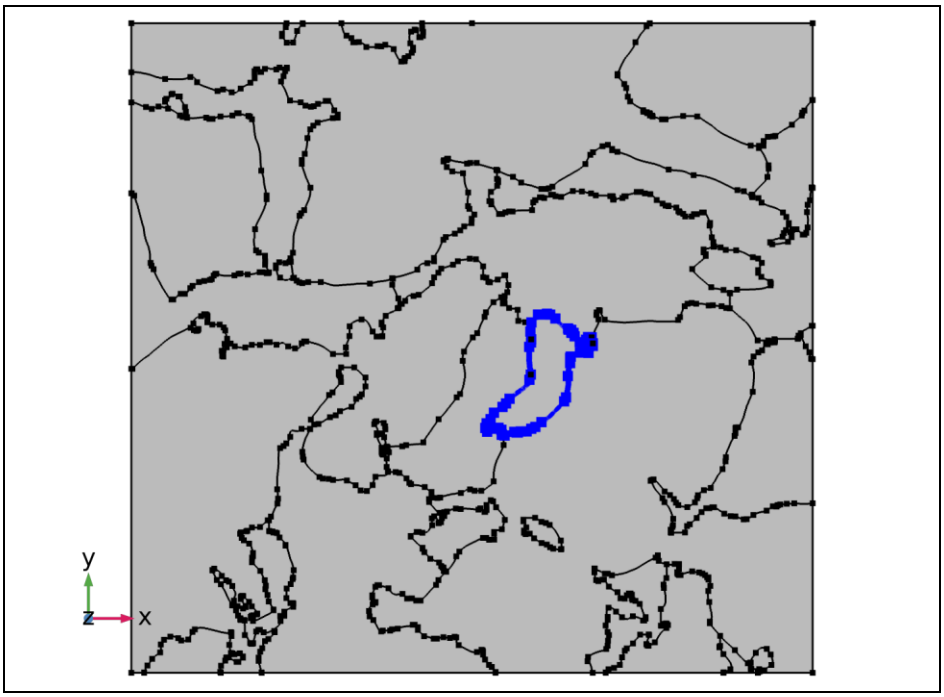

Figure 30: The observation edge of the digitized rock sample. The selected line is on the chalcopyrite mineral border.

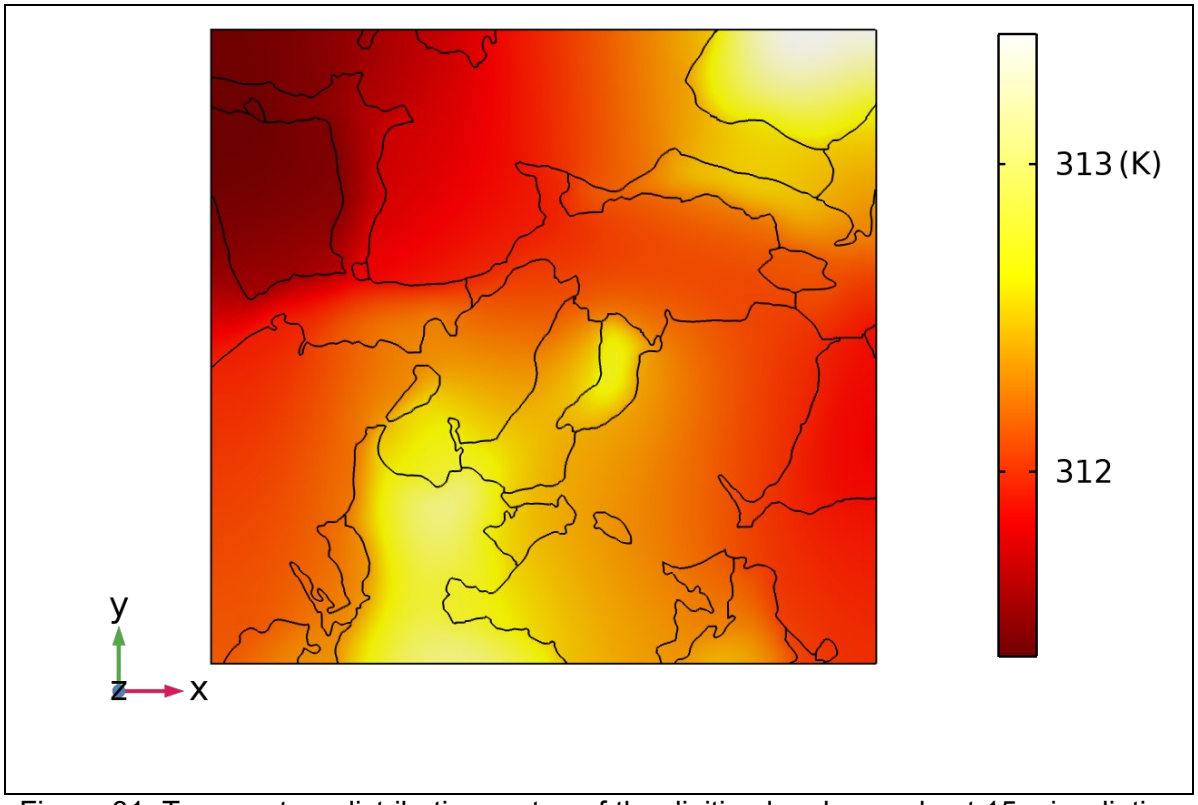

Figure 31: Temperature distribution on top of the digitized rock sample at 15 s irradiation time.

Thermal expansion of the minerals is seen in **Figure 32**. Pyrrhotite has the highest coefficient of thermal expansion which can be observed as a larger strain than on the other minerals.

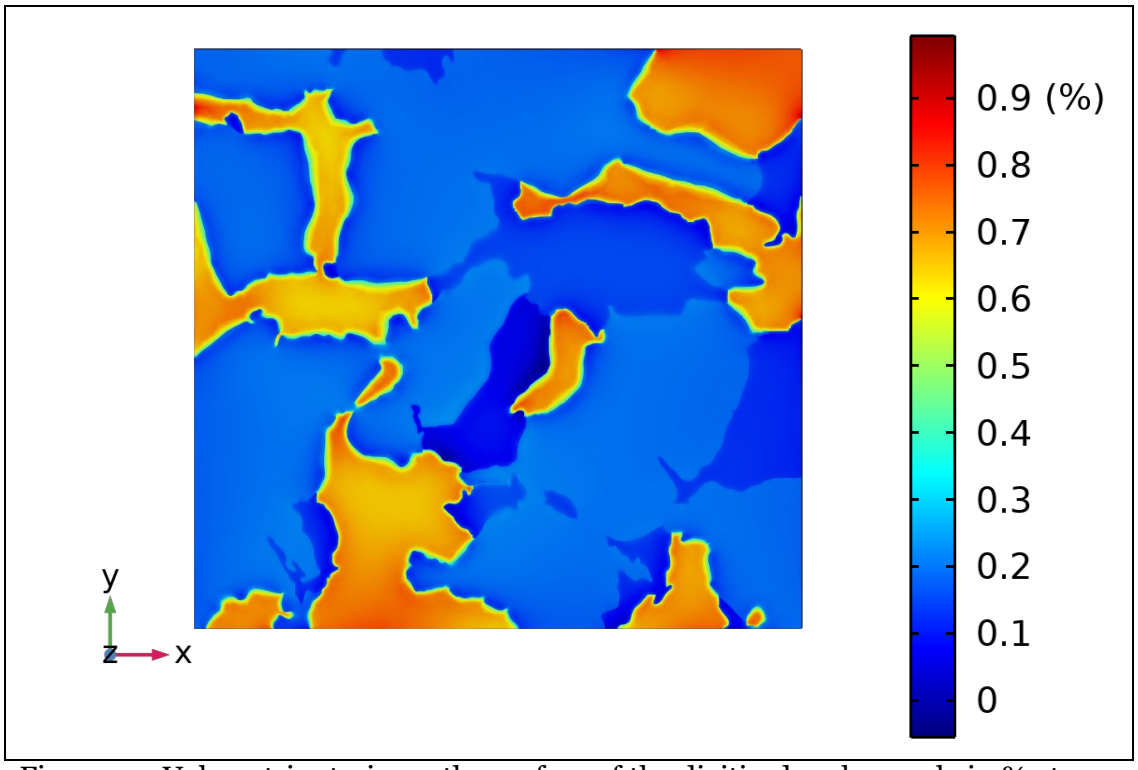

Figure 32: Volumetric strain on the surface of the digitized rock sample in % at 15 s irradiation time.

Finally, the resulting von-Mises stresses are presented in **Figure 33**.

Table 19: The minimum, maximum and average von-Mises stresses and temperatures on the observation edge.

Parameter	**Min**	**Max**	**Average**
von-Mises stress [MPa]	139	553	271
Temperature [K]	312	313	312

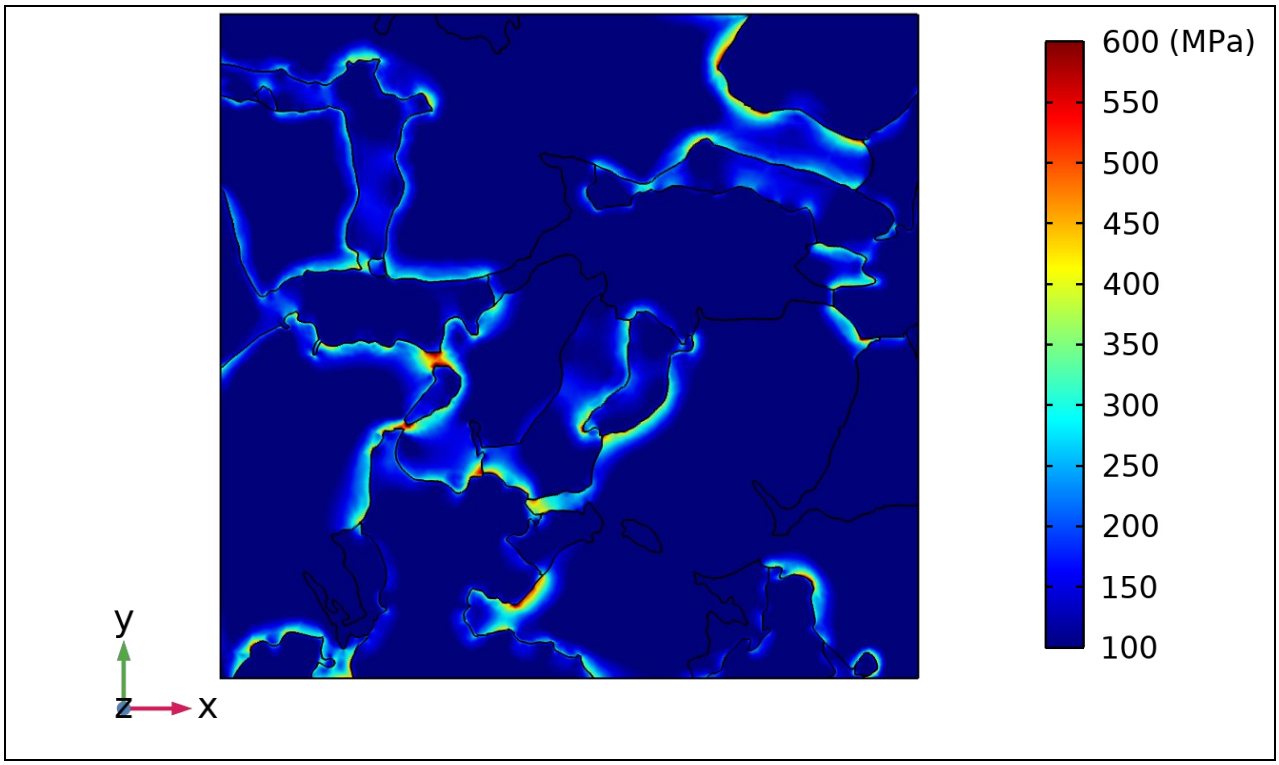

Figure 33: Von-Mises stress distribution on top of the digitized rock sample in MPa at 15 s irradiation time.

7 Discussion of the results

In this section the results for both the simulated and the numerical sample are discussed. The discussion is divided so that the effect of one parameter, either on the radiation or on the material properties, is discussed separately. The results are also compared to the theory presented in **Section 3** and articles published in scientific journals. The effects of the parameters on rock comminution processes are also discussed.

7.1 Effect of the EM-wave pattern

Li *et al.*, (2017) performed numerical analysis on microwave heating of coal. They found out that variations in the EM-field altered the regions where the coal sample was heated up. Similarly in this study, the location of the rock sample influences the temperature and thus the induced stresses of the rock sample. Higher temperatures were reached when the rock sample was situated within an intensive EM wave region. Simultaneously, the average von Mises stresses were over 100 MPa higher. This is due to heat losses in dielectric materials being dependent on the electric field as seen in **Equation (22)**.

This implies that in order to achieve higher stresses, the rocks in rock comminution processes should be placed within intensive EM wave regions. However, in the numerical model it was assumed that the rock sample is stationary and thus it stays stationary in the constant EM-field. In conventional microwave ovens, uniform heating is achieved by rotating the heated object so that it travels through the EM-field.

In rock comminution process this could be solved with a belt fed application, where the rock is travelling on a conveyor through the oven. Thus, the individual rocks would go through both EM minimums and Maximums, allowing for a more uniform heating. Such a system would probably be open-ended and thus research on an open-ended microwave oven could be interesting. In an open-ended setup, the EM-waves would not stop and reflect at the microwave boundaries and thus the efficiency could be lower.

When the cubical sample side length was increased from 0.01 m to 0.1 m in Step 7, the complete sample was not any longer situated within a high-intensity EM-wave area. This resulted in some areas of the sample to heat up considerably more than other areas. This can be clearly seen on the temperature and stress data on the observation edge in **Table 18.** On the line, the temperature between the minimum and maximum temperature varies significantly more (14^{o}C) than in the initial case (0.1^{o}C). In larger sample sizes, the penetration depth of the microwaves should also be considered. As the sample absorbs microwave energy, its intensity decreases throughout the sample. Thus, on larger samples, areas deep within receive less dielectric heat losses and thus heat up less.

In a real-life rock comminution application, this would suggest using the microwave treatment in the later parts of the process, when the rock size is already decreased significantly. Microwave treatment should thus be used either before the grinding, or even between coarse and fine grinding of the rock.

7.2 Effect of the microwave input power and the thermal properties of the rock

In Step 2 the effect of changing the input power of the microwave radiation was studied. Increasing the input power resulted in higher temperatures when comparing identical irradiation times. From **Figure 18**, it can be seen that doubling the input power of the microwave doubles the induced stresses in the sample. However previous studies discussed in **Section 2** such as Ali and Bradshaw (2010) and Pressacco and Saksala (2019), determined that short, high intensity microwave radiation induced stresses at a faster rate, than long, low intensity microwave radiation. In both studies, the effect of microcracks on the rock were included within the model as well as thermally dependent material parameters. As such aspects were not considered in this study, it could explain why no difference in the rate of induced stresses between short, high-intensity, and long, low intensity microwave radiation was found in Step 2.

In this study all material properties were assumed constant in all temperatures. Additionally, the input power in this study stays constant and no heat is transferred from the sample to the environment. Thus, the heat gradient within the rock reaches an equilibrium in a very short time as seen in **Figure 19**. In order to model the heating of the rock sample in more detail in future studies, thermally dependent material parameters should be used. It should be noted however that no comprehensive studies for multiple ore mineral material properties have been conducted. Therefore, thermally dependent material parameters would need to be determined during such a more in-depth numerical model.

As temperature dependent material parameters were not used, comparing stresses induced by very high temperatures is not realistic. With 120 s irradiation times using 5 kW input powers, the temperatures of the sample reached over 700 ^{o}C. With 10 kW input powers, the temperatures were even greater. With such high temperatures, the material properties of the rock and minerals would have altered so drastically that comparing the stress states at 120 s irradiation times is not reasonable. Therefore, irradiation times, on which an induced stress of 100 MPa is reached, were compared in **Section 6.1.**

It is evident that increasing the input power induces stresses faster than when using lower powers. However, if the rate stays constant, Irradiating the rock with double power for half the time should consume as much energy as irradiating the rock with half power for double the time. Thus, it would seem that there is no difference on energy consumption between the two. However, if the thermally dependent material parameters and other aspects discussed above are considered, the energy consumption of short, high-intensity irradiation could be smaller.

In a real application, increasing the irradiation times could increase the rate of heat lost to the surrounding environment. This would favour having short irradiation times with high power. Another aspect to consider is that having long irradiation times decreases the throughput of the microwave treated rock in a comminution process. This is an especially crucial aspect in mines, where large quantities of rocks would be treated. Having a larger throughput could also be achieved with larger surface areas on which the rock can be treated.

For this, large microwave ovens are furthermore required. Finally, the efficiency of the microwave generating devices should also be considered. In case A, all microwave input powers operate with a perfect efficiency, but in a real application, different input powers have different efficiencies. Thus, a balance between a sufficient throughput and operating the microwave-generating device at an optimal efficiency should be sought after.

7.3 Effect of mineral composition and the ratio of low-permittivity material to high-permittivity material

The induced stresses of the different configurations of Step 3 vary significantly. In Step 3, the internal and host minerals were varied between low permittivity quartz and high permittivity pyrite. Switching the internal mineral from pyrite to quartz and vice-versa on the host mineral significantly increased the amount of high-permittivity material in the sample as. Thus, the sample reached over 160 K higher temperatures than in the initial case. The average von-Mises stresses nearly two-folded. Similarly in Step 4, the temperatures of the sample grew higher, as the amount of high-permittivity mineral was increased. The highest stresses in Step 4 were located on mineral boundaries.

This is consistent with previous studies on the field. As discussed in **Section 2**, studies by Kingman, Corfield and Rowson (1998), Ali and Bradshaw (2010), Toifl *et al.* (2016), and Li *et al.* (2019) observed increased stresses on mineral boundaries of heterogenous rocks. This could be due to the different coefficients of thermal expansion between the various minerals.

When the entire sample consisted of pyrite, the temperatures also increased approximately by 160 K. However, the induced stresses decreased significantly when compared to the base case, as the material was fully homogeneous, and no mineral boundaries were present.

Hartlieb *et al.* (2012) stated that a homogenous rock sample heated up equally and significantly. Which is also consistent with the results of this mentioned in the previous paragraph. As there are no mineral boundaries, the stresses do not concentrate in the rock sample and thus the induced stresses stay on lower thresholds.

For rock comminution purposes, it would seem that heterogenous rocks consisting of minerals with high dielectric permittivities should be preferred. However, the various minerals should have different material parameters and clear mineral boundaries, in order to concentrate the stresses. Only when certain thresholds of stresses are reached, damage in the rock can occur, as discussed in **Section 3.5.2**. For example, Pyhäsalmi mine ore consists of inter alia pyrite, chalcopyrite and pyrrhotite, all minerals with high dielectric permittivities. Thus, the ore would heat up significantly when under the influence of microwave radiation and stresses could induce on the mineral boundaries.

In step 5 the individual mineral size is varied, while keeping the fraction of internal mineral to the external constant. The temperature throughout all different grain sizes keeps fairly constant, but the stresses decrease as the mineral size is decreased. Rocks consisting of minerals with smaller grain sizes are closer to a homogenous mass, than those consisting of coarse particles. This could explain, why such behaviour was observed. It should be noted

however that a unified observation boundary could not be established, as the geometry of the sample was altered. The different locations of the observation edge might cause slight deviation in the compared results. Due to the stresses decreasing the more finely grained the minerals are, coarsely grained minerals could benefit more from microwave assisted breakage.

When the shapes of the internal minerals are varied in Step 6, the ratios of internal and external minerals stay constant. However, the angles of the internal mineral corners are either varied or completely removed as seen in **Figure 25.** The temperatures between the various shapes stay similar to each other, but the internal stress states vary greatly. As expected, when the angles of the shapes are decreased, induced stresses increase. This is due to the stresses concentrating on the narrower mineral edges. If heating real rocks is considered, rocks with internal minerals with crystal structures with narrow angles could result in higher, concentrated stresses. Having these high stress concentrations could result in the rock's strength to be exceeded on the areas, where stress is concentrated. These damaged areas can act as places for larger fractures in the rock to induce.

7.4 Numerical model of the digitized sample

The Pyhäsalmi ore sample in **Section 5.3** composes of various minerals that all have relatively high imaginary parts of dielectric permittivity. This leads in large thermal losses in the whole rock sample. As the sample is small, the temperature rises also rapidly.

The stresses on the digitized sample are located on the mineral boundaries as is expected based on previous research discussed in **Section 2** and the results of **Section 6.1**. However, the higher stresses are not present on all mineral boundaries and are instead highest on pyrrhotite-pyrite boundaries.

The differences in stresses between various minerals can be explained with the various material properties of the minerals, namely the coefficient of thermal expansion and Young's modulus. Pyrrhotite has significantly larger coefficient of thermal expansion than the other minerals. Thus, the strain on the pyrrhotite domains is larger than other minerals. Chalcopyrite in the other hand has the lowest coefficient of thermal expansion and thus the strain on chalcopyrite domains are lowest. Both are evident from **Figure 32**.

Pyrite has the second highest coefficient of thermal expansion and thus, the strain on pyrrhotite-pyrite boundaries are very high. This combined with the high Young's modulus of pyrite being over 300 GPa induce largest stresses in the boundaries of pyrite domains. This can be easily explained with **Equation (40)**, where the stresses are dependent both on the strain and the Young's modulus. The higher the strain or Young's modulus, the higher the stresses.

Very low stresses are observed on the pyrite-sphalerite borders. Pyrite has a lower coefficient of thermal expansion than pyrrhotite, while sphalerite has a low Young's modulus of only slightly over 80 GPa. Thus, the stresses on those borders are also lower. In comparison,

stresses between sphalerite and pyrrhotite are larger, but still significantly lower than on pyrrhotite-pyrite borders due to the low Young's modulus of sphalerite.

Although chalcopyrite has the lowest coefficient of thermal expansion and thus the lowest strains, it's high Young's modulus of over 200 GPa also cause large stresses to induce on borders with pyrrhotite.

The results should however not be taken as explicit, as many material parameters of pyrrhotite are significantly larger than on the other minerals. The higher imaginary part of the dielectric constant does not directly affect the stress states on the mineral boundaries, as the temperature differences throughout the rock sample are very small as is evident from **Figure 31**. Higher ϵ_r" affects the overall temperature of the sample and causes overall higher stresses when compared to a more conservative value.

The larger effect is on the significantly, over five times larger, α of pyrrhotite which accounts for the most significant stresses in the rock sample as discussed above. More conservat

Whether microwave pre-treatment can result in a decreased energy consumption of the total rock comminution progress depends, whether the pre-treatment decreases the energy consumption more than it demands energy. In order to further assess this, a experimental study with the above mentioned material properties considered could be beneficial.

8 Conclusions

In this study, two numerical models were created to answer the three research questions laid out in the introduction. The conclusions in this section are based on the questions. The numerical models proved to be a good way to give preliminary results on how different rocks and minerals behave under microwave radiation.

In order to answer the first research question, "*What ores and minerals are suitable for microwave treatment?",* material parameters of various ore minerals found in Finnish mines were compared. Higher dielectric permittivities of the minerals increased the heat losses in the minerals. Thus, minerals with high permittivities are more suitable for microwave pre-treatment, than minerals with low permittivities. Many sulfidic minerals have high values of dilectric permittivities and thus, a sulfidic ore sample from Pyhäsalmi mine was digitized and used in a numerical model to assess induced stresses.

The numerical model on the digitized rock sample showed that the stresses within the sample increased significantly and rapidly under 1 kW microwave radiation. This indicates that microwave pre-treatment can be used to heat up and potentially damage sulfidic minerals.

A numerical model where a simulated rock sample was put under microwave radiation was created to answer the second research question: "*How do different microwave and rock properties affect the induced temperatures and stresses of a simulated rock sample?*". With the model varying different material and microwave radiation parameters could be done easily and the effect of each parameter studied separately.

The results showed that increasing the electromagnetic field pattern affects the heating up of the rock significantly. Placing the sample within a local EM-field maximum yielded higher temperatures and stresses than having it outside the maximum. Furthermore, samples larger than the EM-field maximum heated up uniformly and the microwave did not penetrate the sample as efficiently as when irradiating the smaller samples. Increasing the input power of the microwave radiation also heated up and induced stresses on the sample faster. Doubling input power halved the time to reach same stress thresholds.

Material parameters of the simulated sample also played a large role on the induced stresses. Increasing the amount of high-permittivity material caused the sample to heat up faster. However, boundaries between minerals with different mechanical properties was deemed important to concentrate the stresses. Without mineral boundaries, the induced stresses reached far lower thresholds, even, when the amount of high-permittivity material was increased. Finally, the heterogeneity of the mineral structure also influenced the induced stresses. Larger grain size and narrower mineral angles that caused the rock sample to be more heterogenous increased the stress thresholds.

The final research question, *"How does microwave heating affect the stress-state of a realistic mineral geometry?"* was answered with the numerical model, where the digitized Pyhäsalmi ore sample was irradiated with microwave radiation. The results showed that very large stresses were induced with a short irradiation time on the sample. This was partly due

to the very small size of the sample. Furthermore, it was evident that larger stresses occurred on mineral boundaries between minerals with high elastic moduli and coefficient of thermal expansion. In this model, such boundaries existed between pyrrhotite and pyrite. On these boundaries, the stresses reached over six-fold higher values than on areas in middle of the minerals.

References

Ahrens, T.J. (1995) *Mineral physics and crystallography : a handbook of physical constants*. USA: American Geophysical Union (II).

Alapieti, T.T. and Kärki, A.J. (2005) *Field Trip Guidebook: Early Paleoproterozoic (2.5-2.4) Tornio - Näränkävaara Layered Intrusion Belt and Related Chrome and Platinum-Group Element Mineralization, Northern Finland*. Finland: Vammalan Kirjapaino Oy. Available at: https://tupa.gtk.fi (Accessed: 21 April 2021).

Ali, A.Y. and Bradshaw, S.M. (2010) 'Bonded-particle modelling of microwave-induced damage in ore particles', *Minerals Engineering*, 23, pp. 780–790.

Bécherrawy, T. (2012) *Electromagnetism : Maxwell Equations, Qave Propagation and Emission*. 1st edn. ISTE Ltd and John Wiley & Sons, Inc.

Bektas, R. and Vathavooran, A. (2019) *Laiva, Finland*. NI 43-101 Resource Update. Coffey Geotechnics LTS, A Tetra Tech Company. Available at: http://tupa.gtk.fi/ (Accessed: 21 April 2021).

Brady, B.H.G. and Brown, E.T. (2004) *Rock Mechanics For underground mining*. 3rd. edn. The Netherlands: Springer.

Chou, P.C. and Pagano, N.J. (1967) *Elasticity - Tensor, Dyadic, and Engineering Approaches*. New York: Dover Publications, Inc.

Chung, K. and Myoung-Gyu, L. (2018) *Basics of Continuum Plasticity*. Singapore: Springer Nature Singapore Pte Ltd.

Church, R.H., Webb, W.E. and Salsman, J.B. (1988) *Dielectric Properties of Low-Loss Minerals*. Report of Investigations 9194. United States Department of the Interior. Available at: https://stacks.cdc.gov/view/cdc/10413/cdc_10413_DS1.pdf (Accessed: 4 December 2021).

Clauser, C. and Huenges, E. (1995) 'Rock Physics & Phase Relations: A Handbook of Physical Constants, Volume 3', in *Rock Physics & Phase Relations: A Handbook of Physical Constants, Volume 3*. USA: American Geophysical Union (AGU Reference Shelf, 3).

COMSOL (2018a) 'Heat Transfer Module : User's Guide'. COMSOL. Available at: https://doc.comsol.com/5.4/doc/com.comsol.help.heat/HeatTransferModuleUsersGuide.pdf.

COMSOL (2018b) 'RF Module: User's Guide'. COMSOL. Available at: https://doc.comsol.com/5.4/doc/com.comsol.help.rf/RFModuleUsersGuide.pdf (Accessed: 26 July 2021).

Dahlin, D.C. and Rule, A.R. (1993) *Magnetic Susceptibility of Minerals in High Magnetic Fields*. Report of Investigations 9449. USA: United States Department of the Interior.

Doucet, D., Girard, D., Grondin, L. and Matte, P. (2010) *Technical Report on the December 31, 2009, Mineral Resource and Mineral Reserve Estimate and the Suuri Extension Project, Kittila Mine, Finland*. Kittila Mine Technical Report. Agnico-Eagle Mines Limited. Available at: https://s21.q4cdn.com/374334112/files/doc_downloads/operations/kittila/March4-KittilaMine-Technical-Report-2010_v001_d1j74l.pdf (Accessed: 21 April 2021).

Dragon Mining Limited (2014) *Annual Report 2014*. ABN 19 009 450 051. Dragon Mining Limited.

Dragon Mining Limited (2020) 'Voluntary Announcement Drilling Continues to Define Extensions of the Jokisivu Gold Deposits'. Available at: http://tupa.gtk.fi/ (Accessed: 21 April 2021).

Dunne, R.C., Kawatara, S.K. and Young, C.A. (2019) *SME Mineral Processing & Extractive Metallurgy Handbook - Knovel*. United States: Society for Mining, Metallurgy, and Exploration (SME).

Fricke und Mallah Microwave Technology GmbH (2020) 'Product Catalog'. Fricke und Mallah Microwave Technology GmbH. Available at: https://www.microwaveheating.net/images/Dokumente/2019-0070-Katalog-2020.pdf.

Geological Survey of Finland (2021a) *Kylylahti*. Mineral Deposit Report. Geological Survey of Finland. Available at: http://tupa.gtk.fi/ (Accessed: 21 April 2021).

Geological Survey of Finland (2021b) *Pampalo*. Mineral Deposit Report. Geological Survey of Finland. Available at: http://tupa.gtk.fi/.

Geological Survey of Finland (2021c) *Pyhäsaslmi*. Mineral Deposit Report. Geological Survey of Finland. Available at: http://tupa.gtk.fi/ (Accessed: 21 April 2021).

Goldbaum, M.W. Elliott, R., Maham, Y. and Bobicki, E.R. (2020) 'Investigating the microwave heating behaviour of pyrrhotite tailings', *Mineral Engineering*, 146. doi:https://doi.org/10.1016/j.mineng.2019.106152.

Gray, D., Cameron, T. and Briggs, A. (2016) *Kevitsa Nickel Copper Mine, Lapland, Finland*. NI 43-101 Technical Report. First Quantum Minerals Ltd. Available at: http://tupa.gtk.fi/karttasovellus/mdae/references/12_Kevitsa/12_Kevitsa_Ni43-101_TechnicalReport_20160330.pdf (Accessed: 21 April 2021).

Grigoriev, A.D. (2018) *Microwave Electronics*. Springer International Publishing AG (Springer Series in Advanced Microelectronics).

Haffez, G.S.A. (2012) 'Correlation between bond work index and mechanical properties of some Saudi ores', *Journal of Engineering Sciences, Assiut University*, 40(1), pp. 271–280.

Hahn, D.W. and Özisik, M.N. (2012) *Heat Conduction*. 3rd. edn. New Jersey: John Wiley & Sons, Inc.

Haque, K.E. (1999) 'Microwave energy for mineral treatment processes—a brief review', *International Journal of Mineral Processing*, 57(1), pp. 1–24. doi:https://doi.org/10.1016/S0301-7516(99)00009-5.

Harrison, P.C. (1997) *A fundamental study of the heating effect of 2.45 GHz microwave radiation on minerals*. Doctoral thesis. The University of Birmingham.

Hartlieb, P., Leindl, M., Kuchar, F., Antretter, T. and Moser P. (2012) 'Damage of basalt induced by microwave irradiation', *Minerals Engineering*, 31, pp. 82–89.

Horai, K. (1971) 'Thermal Conductivity of Rock-Forming Minerals', *Journal of Geophysical Research*, 76(5), pp. 1278–1308. doi:https://doi.org/10.1029/JB076i005p01278.

Ji, S. Li, L., Motra, H.B., Wuttke, F., Sun, S., Michibayashi, K. and Salisbury, M.H. (2018) 'Poisson's Ratio and Auxetic Properties of Natural Rocks', *Journal of Geophysical Research: Solid Earth*, 123(2), pp. 1161–1185. doi:https://doi.org/10.1002/2017JB014606.

Karwa, R. (2017) *Heat and Mass Transfer*. Singapore: Springer Scinece + Business Media Singapore.

Khaledalidusti, R., Mishra, A.K. and Barnoush, A. (2019) 'Temperature-dependent properties of magnetic CuFeS2 from first-principles calculations: Structure, mechanics, and thermodynamics', *AIP Advances*, 9(6). doi:10.1063/1.5084308.

Kingman, S., Rowson, N.A. and Sahyoun, C. (2003) 'The Effect of Heat Treatment on Chalcopyrite', *Magnetic and Electrical Separation*, 12(1). doi:DOI:10.1080/1478647031000101296.

Kingman, S.W., Corfield, G.M. and Rowson, N.A. (1998) 'Effects of Microwave Radiation Upon the Mineraloogy and Magnetci Processing of a Massive Norwegian Ilmenite Ore', *Magnetic and Electrical Separation*, Vol. 9, pp. 131–148.

Korman, T., Bedekovic, G., Kujundzic, T. and Kuhinek, D. (2015) 'Impact of Physical and Mechanical Properties of Rocks on Energy Consumption of Jaw Crusher', *Physiochemical Problems of Mineral Processing*, 51(2), pp. 461–475.

Kübler, L. (1985) 'Deformation Mechanisms in Experimentally Deformed Single Crystals of Pyrrhotite, Fe1-xS', *Phys Chem Minerals*, 12, pp. 353–362.

Lefèvre, R., Berthebaud, D., Mychinko, M.Y., Lebedev, O.I., Mori, T., Gascoin, F. and Maignan, A. (2016) 'Thermoelectric properties of the chalcopyrite Cu1-xMxFeS2-y series (M = Mn, Co, Ni)', *RSC Advances*, 6, pp. 55117–55124. doi:DOI: 10.1039/c6ra10046e.

Li, B., Li, H., Chen, Z., Hong, Y. and Wang, Z. (2017) 'Sensitivity analysis on the microwave heating of coal: A coupled electromagnetic and heat transfer model', *Applied thermal engineering*, 126, pp. 949–962. doi:https://doi.org/10.1016/j.applthermaleng.2017.08.012.

Li, J. Kaunda, R.B., Hartlieb, P. and Nelson, P. (2019) 'Fully-coupled simulations of thermally-induced cracking in pegmatite due to microwave irradiation', *Journal of Rock Mechanics and Geotechnical Engineering*, 11(2), pp. 242–250. doi:10.1016/j.jrmge.2018.12.007.

Lovás, M., Kovácová, M., Dimitrakis, G., Cuvanová, S. and Znamenácková, I. (2010) 'Modelling of microwave heating of andesite and minerals', *International Journal of Heat and Mass Transfer*, 53, pp. 3387–3393.

Lupi, S. (2017) *Fundamentals of Electroheat : Electrical Technologies for Process Heating*. 1st. edn. Switzerland: Springer International Publishing AG.

Marland, S., Merchant, A. and Rawson, N. (2001) 'Dielectric properties of coal', *Fuel*, 80(13), pp. 1839–1849. doi:https://doi.org/10.1016/S0016-2361(01)00050-3.

Peng, Z. Hwang, J., Kim, B., Kim, J. and Wang, X. (2014) 'Characterization of Minerals, Metals, and Materials 2014', in *Characterization of Minerals, Metals, and Materials 2014*. USA: Wiley.

Pressacco, M. and Saksala, T. (2018) 'Numerical modelling of fracture processes in thermal shock weakened rock', in. *European Rock Mechanics Symposium (EUROCK2018)*, St. petersburg, Russia.

Pressacco, M. and Saksala, T. (2019) 'Numerical modelling of heat shock-assisted rock fracture', *International Journal for Numerical and Analytical Methods in Geomechanics*, 48(1), pp. 40–68. doi:10.1002/nag.3004.

Reino, J. and Pekkarinen, L. (1989) 'Sotkamon Talvivaaran monimetalliesiintyman geologiset tutkimukset 1.1. - 30.4.1989'. Finland. Available at: https://tupa.gtk.fi/ (Accessed: 21 April 2021).

Richardson Electronics (no date) 'Industrial Microwave Product Guide'. Richardson Electronics. Available at: https://avtec.su/files/tubes/industrial_microwave_products.pdf (Accessed: 14 June 2021).

Robertson, E.C. (1988) *Thermal Properties of Rock*. Open-File Report 88–441. United States Department of the Interior Geological Survey.

Rochette, P., Jackson, M. and Aubourg, C. (1992) 'Rock magnetism and the interpretation of anisotropy of magnetic susceptibility', *Reviews of Geophysics*, 30(3), pp. 209–226. doi:https://doi.org/10.1029/92RG00733.

Rosenholtz, J.L. and Smith, D.T. (1936) 'The dielectric constant of mineral powders', *American Mineralogist*, 21(2), pp. 115–120.

Salsman, J.B. (1992) 'Measurement of Dielectric Properties in the Frequency Range of 300 MHz to 3 GHz as a Function of Temperature and Density', *Ceramic Transactions : Microwaves: theory and Application in Materials Processing*, 21, pp. 203–214.

Schubert, G. (2015) *Treatise on Geophysics*. 2nd. edn. Elsevier.

Shinohara, N. (2014) *Wireless Power Transfer via Radiowaves*. 1st. edn. London: ISTE Ltd.

Sidebotham, G. (2015) *Heat Transfer Modeling : An Inductive Approach*. 1st. edn. Springer International Publishing Switzerland.

Sotkamo Silver (2021) 'Hopeakaivos - Geologia'. Available at: https://www.silver.fi/fi/hopeakaivos/geologia.

Sweco Industry Oy (2016) *Keliber Lithium Project*. Pre-feasibility Study F13272. Helsinki. Available at: https://www.keliber.fi/ (Accessed: 21 April 2021).

Tenailleau, C., Etschmann, B., Wang, H., Pring, A., Grguric, B.A. and Studer, A. (2005) 'Thermal expansion of troilite and pyrrhotite determined by in situ cooling (873 to 373 K) neutron powder diffraction measurements', *Mineralogical Magazine*, 69(2), pp. 205–216. doi:DOI: 10.1180/0026461056920247.

Toifl, M., Meisels, R., Hartlieb, P., Kuchar, F. and Antretter, T. (2016) '3D numerical study on microwave induced stresses in inhomogeneous hard rocks', *Minerals Engineering*, 90, pp. 29–42.

Vasara, H. (2019) *Toimialaraportit : Kaivosteollisuus*. Kaivosalan toimialaraportti 2019:57. Helsinki: Työ- ja elinkeinoministeriö. Available at: https://julkaisut.valtioneuvosto.fi/ (Accessed: 21 April 2021).

Wang, J., Mao, Z., Jiang, F. and Duffy, T. (2015) 'Elasticity of single-crystal quartz to 10 GPa', *Phys Chem Minerals*, 42, pp. 203–212. doi:DOI 10.1007/s00269-014-0711-z.

Waples, D.W. and Waples, J.S. (2004) 'A Review and Evaluation of Specific Heat Capacities of Rocks, Minerals, and Subsurface Fluids. Part 1: Minerals and Nonporous Rocks', *Natural Resources Research*, 13(2), pp. 97–122.

Whitaker, M.L. Liu, W., Wang, L. and Li, B. (2010) 'Acoustic Velocities and Elastic Properties of Pyrite (FeS2) to 9.6 GPa', *Journal of Earth Science*, 21(5), pp. 792–800. doi:DOI: 10.1007/s12583-010-0115-z.

Whittles, D.N., Kingman, S.W. and Reddish, D.J. (2003) 'Application of numerical modelling for prediction of the influence of power density on microwave-assisted breakage', *International Journal of Mineral Processing*, 68(1–4), pp. 71–91.

Wills, B.A. (2006) *Will's Mineral Processing Technology : An Introduction to the Practical Aspects of Ore Treatment and Mineral Recovery*. 7th. edn. United Kingdom: Elsevier.

Wyzga, P., Bobnar, M., Hennig, C., Leithe-Jasper, A., Mori, T. and Gumeniuk, R. (2017) 'Thermoelectric Properties of Natural Chalcopyrite from Zacatecas, Mexico', *Journal of Inorganic and General Chemistry*, 643, pp. 858–863. doi:DOI: 10.1002/zaac.201700074.

Zhandov, Michael.S. (2018) 'Chapter 10 - Electromagnetic Properties of Rocks and Minerals', in *Foundations of Geophysical Electromagnetic Theory and Methods (Second edition)*. 2nd. edtn. United States: Elsevier, pp. 353–400.

Zheng, Y.L., Zhao, X.B., Zhao, Q.H., Li, J.C. and Zhang, Q.B. (2020) 'Dielectric properties of hard rock minerals and implications for microwave-assisted rock fracturing', *Geomech. Geophys. Geo-energ. Geo-resour*, 62(2), pp. 21–22. doi:https://doi.org/10.1007/s40948-020-00147-z.